MOPITT

Measurement of Pollution in the Troposphere

ALGORITHM THEORETICAL BASIS DOCUMENT

Retrieval of Carbon Monoxide Profiles and Column Amounts of Carbon Monoxide and Methane from MOPITT Observed Radiances

(Level 1 to Level 2)

Version 3

DRAFT

NCAR MOPITT Team

August, 1996

TABLE OF CONTENTS

Algorithm Theoretical Basis Document (ATBD)

Retrieval of Carbon Monoxide (CO) Profiles and Column Amounts of CO and Methane (CH_4) from MOPITT Observed Radiances

(Level 1 to Level 2)

1.0 Introduction

The intent of this document is to describe the algorithm involved in converting the Level 1 MOPITT radiances into the Level 2 products of retrieved CO profiles and column amounts of CO and CH_4. An overview of the MOPITT retrieval objectives is given along with a brief instrument description.

The MOPITT Level 1 to Level 2 data reduction algorithms are detailed in three sections. First, the forward model is described for both the CO thermal channels and the CO and CH_4 solar channels. Second, the cloud detection and clearing algorithm is addressed, explaining how MOPITT will determine clear, cloud contaminated and cloud cleared scenes. Third, the retrieval algorithm is presented and evaluated for the CO and CH_4 channels.

The last section deals with practical considerations involved with the conversion of Level 1 radiance into a Level 2 product.

2.0 Overview and Background Information

2.1 Experimental Objective

The MOPITT experiment has been described by Drummond (*1992*). The objective of MOPITT CO measurements is to obtain profiles with a resolution of 22 km horizontally, 3 km vertically and with an accuracy of 10% throughout the troposphere. A CO total column amount measurement will also be made with a 10% accuracy. For CH_4, the objective is to measure the column in the troposphere to a precision of better than 1%, with a spatial resolution similar to that of the CO measurement. The column amounts of CO and CH_4 will only be available on the sunlit side of the orbit as standard level 2 MOPITT products.

The concentration of CO in the earth's atmosphere had been increasing mainly because of increased human activities (*Khalil and Rasmussen, 1984*). However recent surface mesurments by Novelli et al.(1994), show a leveling off of the CO concentration. The full range of the

effects of the increased concentration of CO is not fully understood at the present time, but it is believed that CO is photochemically active and plays a major part in the concentration of OH radicals in the troposphere. Increased CO may deplete tropospheric OH radicals, thereby reducing the yearly removal of many natural and anthropogenic trace species. In particular, this effect may add to the increase of CH_4, which in turn could further reduce OH concentration. Increased CO may also indirectly intensify global warming and perturb the stratospheric ozone layer by increasing the lifetime of trace gases such as CH_4, CH_3Cl, CH_3CCl_3, and CFCs. Global measurements of CO and CH_4 will undoubtedly shed light on the concentration of OH, which is one of the most important and difficult species to measure from space due to its very low concentration. Those measurements will enhance our knowledge of the chemistry of the troposphere, and particularly how it interacts with the surface/ocean/biomass systems, atmospheric transports, and the carbon cycle. Global CO and CH_4 measurements from MOPITT will also be used in parallel modeling efforts to advance our understanding of global tropospheric chemistry and its relationship to sources, sinks, and atmospheric transports, which can be determined from other data. Understanding their biogeochemical cycles and their intimate interrelation with each other and with climate will lead to better predictions of possible effects of anthropogenic activities.

2.2 Historical Perspective

The possibility of remotely measuring CO profiles in the troposphere from space-borne platform observations of thermal infrared emission/absorption was first suggested by Ludwig *et al.* in 1974. Success of the Measurement of Air Pollution from Satellites (MAPS) on the second Space Transport System engineering test flight (STS-2) of the shuttle in November 1981 proved the feasibility of inferring CO profile from measurements by a nadir-viewing instrument (*Reichle et al Reichle et al., 1986; Reichle et al., 1989; Reichle et al., 1990*). The instrument employed is a gas filter radiometer operating in the 4.7 μm region of the CO fundamental band with a passband from 2080 to 2220 cm^{-1}. At the surface the instantaneous field of view is approximately 20 by 20 km. Successive MAPS experiment provided more global tropospheric CO measurements and further demonstrated the importance and feasibility of CO measurements from space.

Even though MAPS experiments have provided important global CO measurements for global tropospheric chemistry study, limited coverage and only the average CO mixing ratio in the middle of the troposphere is not adequate, and multiple level CO measurements that would resolve the troposphere into several layers are needed. MOPITT is an instrument designed to meet this requirement and provide global CO measurements of the lower, middle, and upper troposphere and daytime total columns of CO and CH_4. The MOPITT retrieval algorithm is based on proven retrieval techniques, such as the maximum likelihood method (*Rogers, 1976*), and is designed to maximize scientific return of the MOPITT experiment with state-of-the-art retrieval techniques.

2.3 Instrument Characteristics

Drummond (*1992*) has outlined the MOPITT instrument concept. The approach and viewing geometry are shown in Fig. 2.3.1. MOPITT, on the AM1 platform, measures upwelling thermal emission from the atmosphere and surface in the long-wave channels, and reflected solar radiation in the short-wave channels that has passed through the atmosphere, reflected at the surface, and transmitted back up through the atmosphere. Total atmospheric transmittance derived from reflected sunlight measurements is a convenient way to determine the total column amount of a trace gas. This technique requires that the target gas has a spectral band in a region with large solar radiance, and the total optical depth along such a path is not too large. Methane has an overtone band near 2.2 μm with a measurable, but not large, total absorption for such a

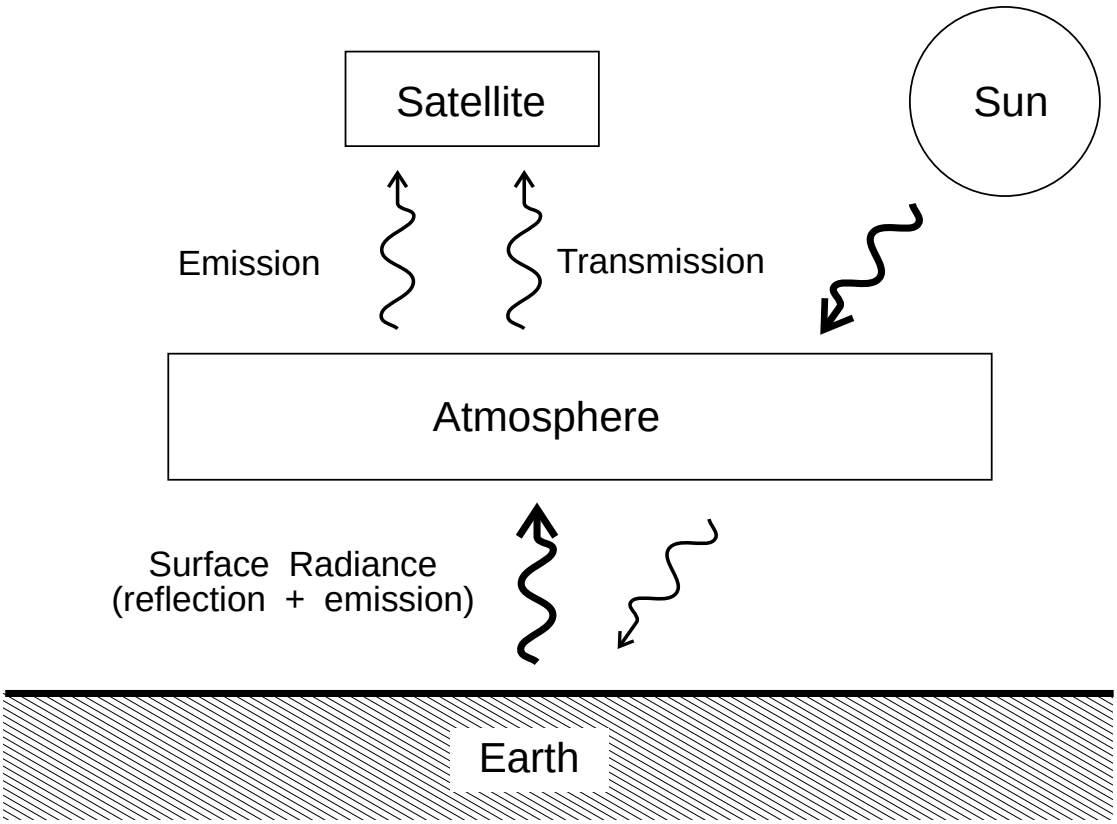

Figure 2.3.1 Schematic diagram of MOPITT measurement system.

path. Similarly, CO has its first overtone band at 2.3 μm which is also suitable. For vertical profiling, the requirement is that significant and measurable portions of the signal must originate in different atmospheric layers, which means that there must be a few values of different but appreciable opacity in the atmosphere, and that there must also be a source of radiation in the atmosphere. Thermal emission is a radiation source, and the CO fundamental band at 4.7 μm has enough opacity to determine atmospheric amounts, as demonstrated by *Reichle et al.* (*1986, 1990*).

All three bands are in regions of the spectrum with other bands, and the lines of the gases of interest are mixed with those of interfering species. It would be possible, in principle, to measure the total emission or transmission of the species of interest, and correct for the contributions of the interfering species. However, the contributions of other species are often larger than those of the gases of interest, and their amounts are not always known with sufficient accuracy. The uncertainties of the corrections may significantly degrade, or even mask, changes due to the gas of interest.

MOPITT is designed to meet this challenge by enhancing the sensitivity of the instrument to the gas of interest. Since all gases in the atmosphere are emitting/absorbing simultaneously, it is essential that the effect of the gas of interest can be separated out from the general radiation field. Further, since the information about the vertical distribution of the gas is contained within the shape of an individual absorption/emission line, it is necessary to be able to resolve the line shape, which generally requires high spectral resolution. High spectral resolution leads to low

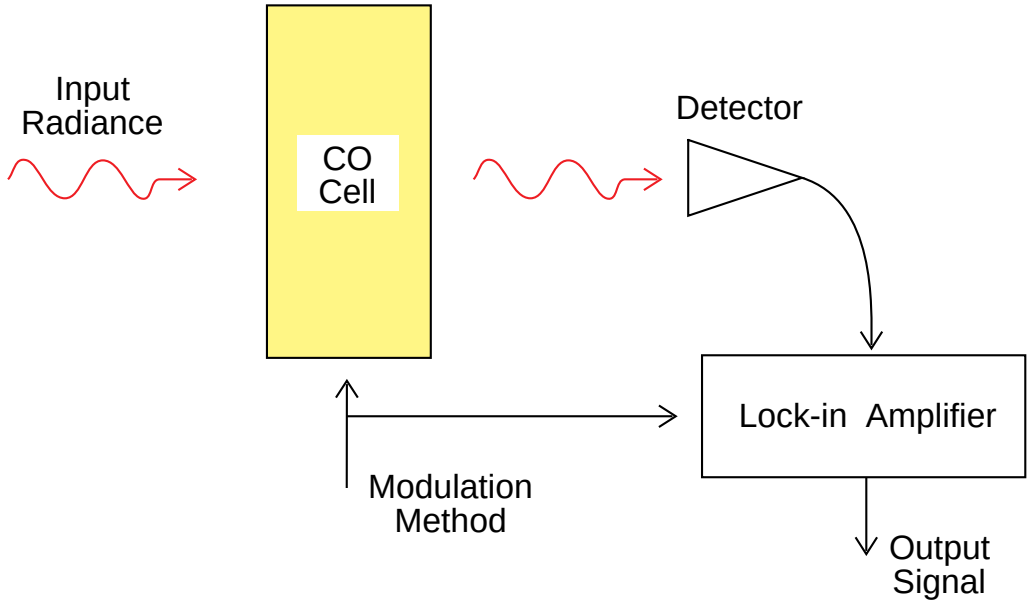

Figure 2.3.2 A basic correlation radiometry system.

signal to noise, which means low instrument sensitivity. Therefore, high sensitivity and high spectral resolution requirements for tropospheric trace species remote sensing are difficult to implement with conventional dispersing instruments.

Correlation Spectroscopy (CR), a non-dispersing spectroscopy technique, offers the opportunity for high spectral resolution as well as high signal to noise. The fundamental techniques of correlation spectroscopy are illustrated in Fig. 2.3.2. The cell contains a sample of the target gas. Assume monochromatic radiation enters from the left and is detected by the system on the right, the output as a function of spectral frequency is shown in Fig. 2.3.3(a) for two different amounts of gas in the absorption cell. By cycling the amount of gas in the absorption cell between the two states, the detector will be alternately looking through two different filters. The difference of the two signals will be identical to the output of a system in which the gas cell and its modulator are replaced by an optical filter of profile shown by the Equivalent Difference Transmission (EDT) curve in Fig. 2.3.3(b). The apparatus has the following unique characteristics:

(1) The equivalent filter profile, is zero between the spectral lines of the gas in the cell, eliminating signals from spectral regions subject to interference by other species as illustrated in Fig. 2.3.3(c).
(2) The filter profile has a maximum at each spectral line and thus the energy from each spectral line in a broadband emission is collected simultaneously. Therefore, the system is very sensitive to radiation with a spectrum identical or similar to that of the gas in the cell. Obviously the spectrum of the gas itself is best correlated with the filter profile.
(3) The apparatus does not require any high precision optical adjustments. In fact, the only thing that affects the alignment is Doppler shift caused by relative motion between gas in the cell and the emitting atmospheric gas.

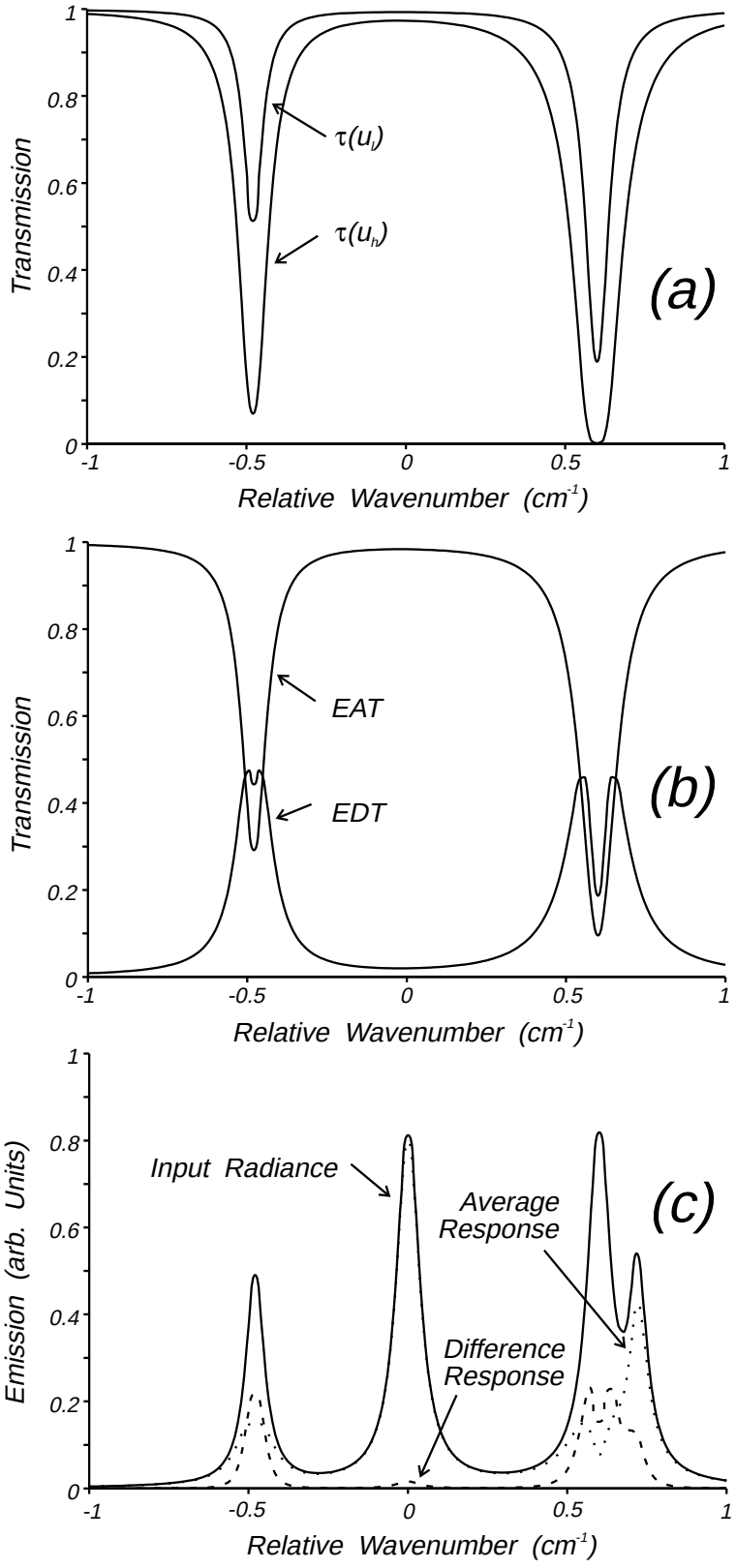

Figure 2.3.3 Operation of a correlation spectrometer in spectral space. EAT stands for Equivalent Average transmission, EDT stands for Equivalent Difference Transmission.

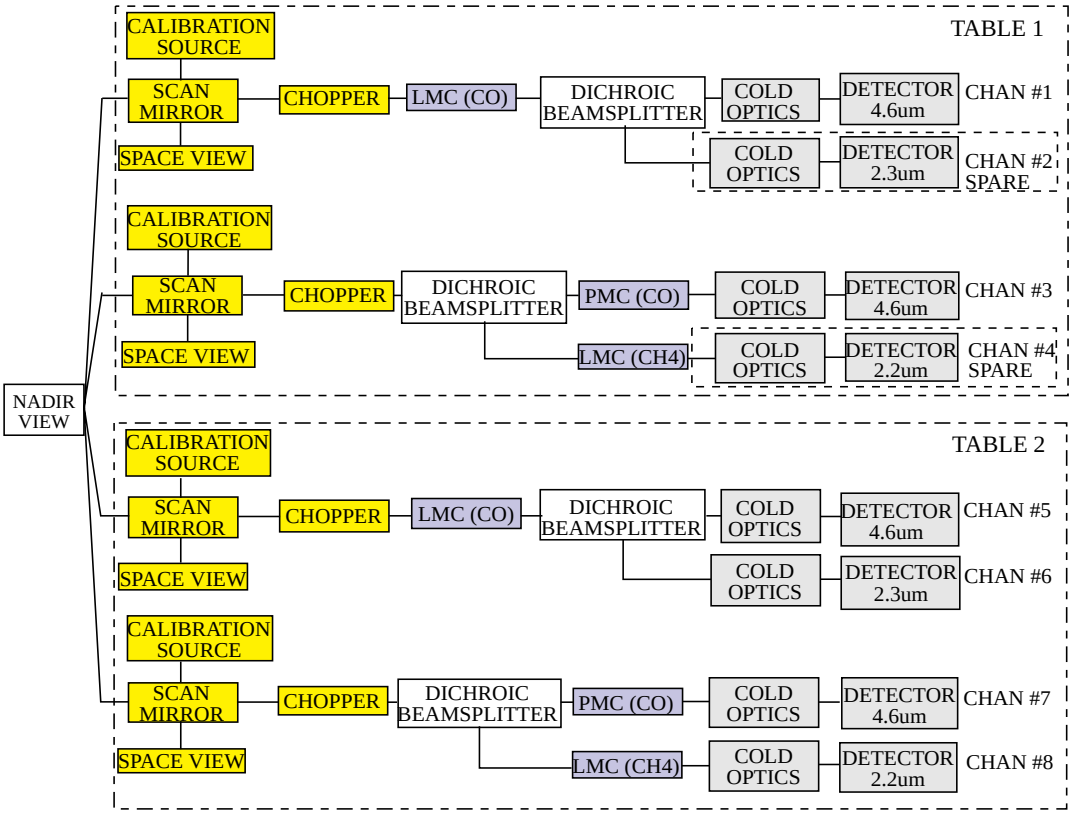

Figure 2.3.4 MOPITT optical channel diagram.

(4). The shape of the equivalent filter is sensitive to the amount of gas in the cell. If small amounts of gas are placed in the cell, the spectral lines will be narrow with incomplete absorption at the centers of the lines. The EDT will have peaks in line centers, where absorption coefficients are largest. If larger amounts of gas are placed in the cell, the lines will be broader and completely absorbed in the centers. In this case, the EDT will have peaks in the line wings, where absorption coefficients are smaller. By placing different amount of gas in the cell, different parts of the spectral line will be sampled, leading to altitude discrimination or vertical resolution. The largest part of the upwelling signal emitted by the atmosphere comes from the altitude region in which the optical depth is near unity. Thus, a cell that is sensitive to the line center will respond to signals originating higher in the atmosphere, while a cell with larger amounts of gas will respond to signals originating in the wings of the pressure broadened lines, at higher pressures (lower altitudes). The average of the signals obtained at the two states of the correlation cell can also be obtained. The resulting Equivalent Average Transmittance (EAT) is also shown in Fig. 2.3.3(b). It has the property that its transmittance is near unity away from the lines in the cell, but it reduces the signals at the centers of the lines. Thus, it is sensitive to other gases, and especially to the surface contribution to the upwelling radiation in the spectral regions of interest.

MOPITT makes use of two methods to modulate the gas transmittance. The first is by pressure modulation through the use of pressure modulated cells which have been described in detail by Taylor (*1983*). The second is by modulating the length of the gas cell in the optical path, through length modulated cells (*Drummond*, *1989*). A block diagram of the MOPITT optical arrangement is shown in Fig. 2.3.4. Two pressure modulated radiometers (PMR's) with different mean pressures and four length modulated radiometers (LMR's) are used. Separating the 2 μm and 4.7 μm channels with dichroic filters results in 8 separate spectral channels. Their design characteristics are summarized in Table 2.3.1; these values will be updated when measurements of the characteristics of the flight instrument are made during its characterization and calibration. Each channel produces an average (A) and a difference (D) signal.

Table 2.3.1 MOPITT nominal channel characteristics. Channels 1,3,5, and 7 are CO thermal channels. Channels 2 and 6 are CO solar channels. Channels 4 and 8 are CH_4 solar channels.

Channel Characteristics	1	2	3	4	5	6	7	8
Gas Species	CO	CO	CO	CH_4	CO	CO	CO	CH_4
Nominal Gas Pressure (kPa)	20	20	7.5	80	80	80	3.8	80
Mid-Wavenumber (cm^{-1})	2166	4285	2166	4430	2166	4285	2166	4430
Wavenumber Range (cm^{-1})	52	40	52	139	52	40	52	139
Mid-Wavelength (mm)	4.617	2.334	4.617	2.258	4.617	2.334	4.617	2.258
Wavelength Range (mm)	0.111	0.022	0.111	0.071	0.111	0.022	0.111	0.071
Modulator Type & Number	LMC1	LMC1	PMC1	LMC2	LMC3	LMC3	PMC2	LMC4
Nominal Modulator Freq (HZ)	11.78	11.78	51.85	11.78	11.54	11.54	42.85	11.54
Nominal Chopper Freq (Hz)	518.5	518.5	518.5	518.5	600	600	600	600
Scan Mirror/Chopper Number	#1	#1	#2	#2	#3	#3	#4	#4
Calibration Source Number	#1	#1	#2	#2	#3	#3	#4	#4
Optical Table	#1	#1	#1	#1	#2	#2	#2	#2

2.4 Experimental Study and Modeling of Pressure Modulator Cell (PMC) and Length Modulator Cell (LMC)

Pressure Modulator Radiometers (PMR) have been flown on numerous satellite missions including Nimbus 4 and 5 in 1970 and 1972, Pioneer Venus in 1978, and the Upper Atmosphere Research Satellite (UARS) in 1991. Extensive laboratory experimental studies to understand the operation of the pressure modulator cell (PMC) and the length modulator cells (LMC) have been conducted by many groups around the world. Models and calibration techniques of different complexity have been developed. May *et al.*, at JPL presented their investigation of the PMC with a tunable diode laser system in 1988 (*May et al., 1988*). For the first time, the mean and modulated transmission function of a pressure modulator cell have been measured during

operation using a tunable diode laser spectrometer. Good agreement was obtained between theoretical calculations and measurements. Roscoe and Wells reported on a very detailed investigation of the variation of pressure, temperature, and transmission within a pressure modulator in 1989 (*Roscoe and Wells, 1989*). Berman *et al.,* of the University of Toronto published the results of their investigation of a CO correlation cell in 1993 (*Berman et al., 1993*). Precise spectral line measurements of CO in an operating PMC was conducted using spectroscopic techniques. It demonstrated that dynamic spectroscopic measurements of both temperature and pressure in a PMC can be made. They also showed that gas amounts and pressure in a PMC cell can be accurately measured after filling and sealing, thus providing a noninvasive monitor of gas purity and amount during the ground testing phase of the satellite instrumentation. Those studies clearly demonstrated that the operation of the PMC and the cell transfer function, can be measured and modeled accurately. Similar measurements will be conducted with the MOPITT PMC.

There is no change of pressure in the sealed correlation cell during the operation of LMC, and the modulation is achieved by the change of the path length. The calibration and modeling of both PMC and LMC have been and will continue to be conducted at the University of Toronto. We are confident that an accurate transfer function of the correlation cells will be obtained for MOPITT. More detailed information on the calibration and modeling of PMC and LMC can be found in the references listed at the end of this document.

3.0 MOPITT Level 1 to Level 2 Data Reduction Algorithm Description

3.1.1 Physics of the Problem: Forward Model for Clear Sky Radiances

The measurement of CO and CH_4 in the troposphere requires an instrument that uses a nadir-viewing geometry. Compared to other atmospheric gases, the concentration of CO is relatively low, in the range 50-200 ppbv, and this concentration can vary significantly over small spatial and temporal scales. In the case of CH_4, a substantial change in the concentration near the surface may only result in a small change in the total column amount above the source region. The measurement system must therefore maximize total signal from these gases while using high effective spectral resolution to ensure sensitivity to changes in their concentration. This is best achieved using gas correlation spectroscopy.

The MOPITT instrument will make measurements in three spectral regions. A thermal channel at 4.7 μm will be used to obtain profile information about the tropospheric CO distribution. Short-wave solar reflectance channels will be used at 2.3 and 2.2 μm for total column measurements of CO and CH_4, respectively .

The forward model provides a numerical simulation of the radiative transfer of the problem and a physical description of the measurement process. The purpose of the forward model is twofold. The first is to study the measurement characteristics, and developing a forward model is an important step in the design of the instrument. The second is to form part of the data retrieval system. Derivation of the desired atmospheric parameters from the instrument signals is an inversion process. An accurate forward model is a necessary condition for the successful inversion. Clouds are not considered in the forward model discussed here. The MOPITT approach for discriminating clear sky from clouds and the algorithm for deriving clear sky radiances and cloud fraction under partially cloudy conditions are described in sections 3.2, 3.3 and 3.4, respectively.

3.1.2 The Radiative Transfer Equation

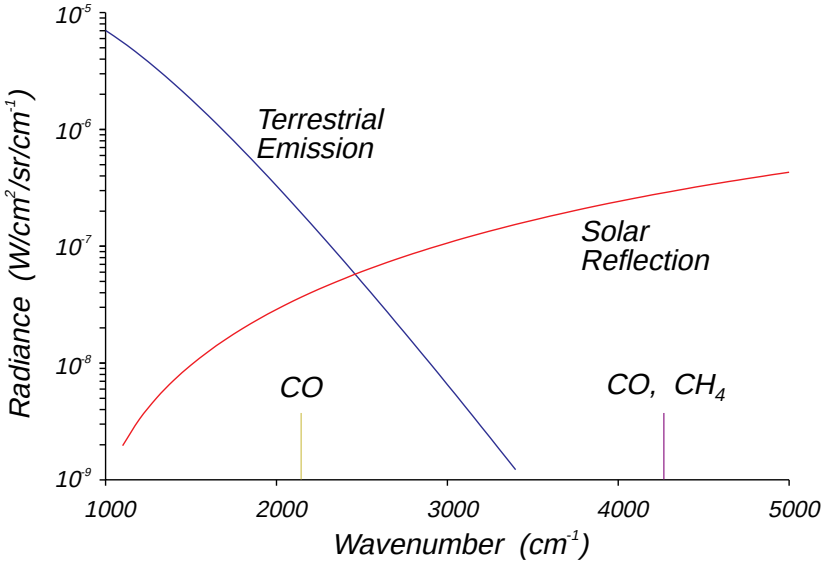

Figure 3.1.1 The comparative strengths of solar and terrestrial radiation in the range 1000-5000 cm^{-1}. A terrestrial thermal radiation temperature of 260 K has been assumed and a solar radiation temperature of 5780 K. The solar curve has been corrected for a Lambertian reflector with reflectivity varying from 1% at 1000 cm^{-1} to 25% at 5000 cm^{-1}. Also indicated are the spectral intervals of interest to MOPITT.

For the MOPITT spectral regions of interest, the monochromatic radiance $I^{CLEAR}(\nu,h)$ at the top of the atmosphere can be described by the radiative transfer equation,

$$I^{CLEAR}(\nu,h) = I(\nu,h_s)\tau(\nu,h_s) + \int_{h_s}^{h} B(\nu,T(z))\frac{d\tau(\nu,z)}{dz}dz \quad , \tag{3.1.1}$$

where $I(\nu,h_s)$ is the upwelling monochromatic radiance at the surface h_S [W/(m^2.sr.cm^{-1})]; $\tau(\nu, z)$ is the monochromatic atmospheric transmittance from z to h; $B(\nu,T(z))$ is the Planck function [W/(m^2.sr.cm^{-1})]; and h is the height of the instrument platform [m]. The first term on the right of Eq. (3.1.1) describes the radiation reaching the instrument from the Earth's surface, the second gives the contribution to the total radiance from atmospheric self emission between the surface and the instrument. The radiative transfer equation for a cloudy atmosphere is given in section 3.2.1.

The boundary radiance term is composed of two parts:

$$I(\nu,h_s) = \varepsilon B(\nu,T_s) + (1-\varepsilon)I_b(\nu,h_s), \tag{3.1.2}$$

where ε is the surface emissivity, T_S is the surface temperature, and I_b is the downward radiance perpendicuar to the earth surface. The latter includes both solar radiation and the thermal emission of the atmosphere.

The relative importance of the two terms of Eq. (3.1.1) depends essentially on the wavelength of the observation. This is illustrated in Figure 3.1.1. At longer wavelengths, where the solar spectrum is weak and the ground reflectivity is low the two terms are of equal magnitude. The boundary radiance term is then dominated by thermal radiation. However, at shorter wavelengths, the first term usually dominates because of the strength of the solar spectrum and the increasing surface reflectivity.

The boundary radiance term is determined partly by the transmittance $\tau(\nu,h_S)$, which in turn depends on the total column of the absorbing gas, whereas the differential in the second term of Eq. (3.1.1) is strongly affected by the height distribution. Measurements performed by monitoring solar radiation tend to measure the total column amount of gas (remember that the radiation traverses the atmosphere twice), whereas those performed by monitoring terrestrial radiation can obtain vertical profile information.

3.1.3 The CO Thermal Channels

The CO channel at 4.7 μm has a preliminary bandpass of 2140-2192 cm^{-1} and covers the *R*-branch of the CO(1) fundamental band. This band is at the short-wave end of the Earth/atmosphere thermal emission spectrum. The gas correlation technique, used in the PMRs and LMRs of MOPITT, serves to make the instrument particularly sensitive to that component of the total channel signal from the gas being measured and allows high effective signal-to-noise. However, there is a contaminating signal due to the presence of bands of other gases, particularly H_2O, CO_2, O_3, and N_2O in this spectral region (Figure 3.1.2). This contamination can be reduced by carefully choosing the channel passband.

MOPITT uses a nadir-viewing geometry, and the Earth's surface is always in the field of view of the instrument. Because relatively weak tropospheric bands that are not optically thick through

the vertical atmosphere are used, the surface will always provide the primary signal at the radiometer in the 4.7 μm thermal channel. It is therefore important to characterize accurately the surface temperature and emissivity. The radiation seen at 2140 cm^{-1} for a nadir view at the

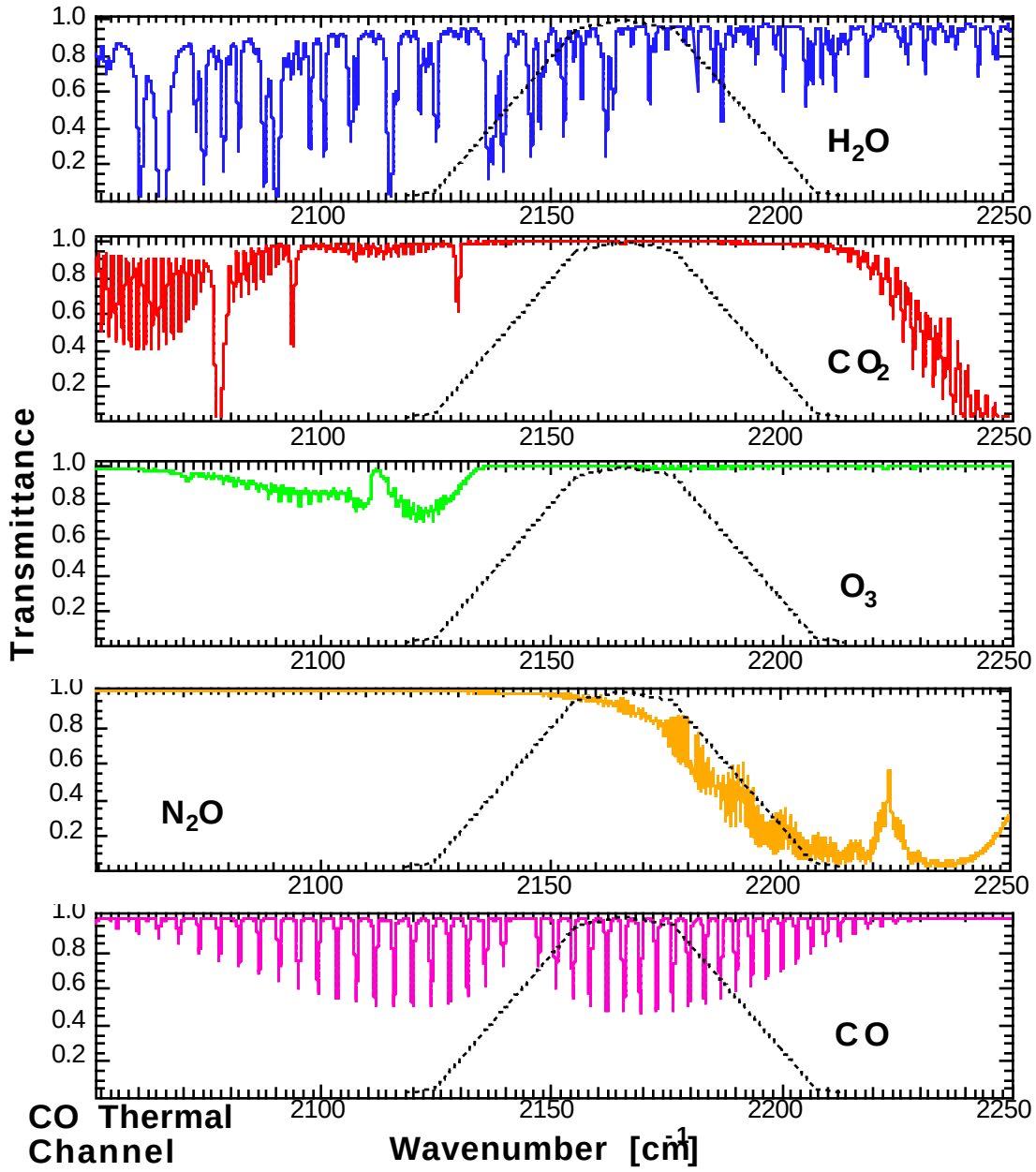

Figure 3.1.2 The atmospheric transmittance for a nadir view of the atmosphere in the 4.7 μm spectral interval. The transmittance of each of the important absorbing gases is shown individually. Spectra are calculated at a resolution of 0.5 cm^{-1}. The CO thermal channel passband is also indicated.

top of the atmosphere is shown in Figure 3.1.3. The gas signatures appear in absorption due to the fact that the emitting layers of the atmosphere are at a lower temperature than the surface.

The reflected downward radiance is, however, not negligible. For the daytime measurement, this reflected radiance is mainly the transmitted sunlight, while for the nighttime measurement, the downward radiance is the thermal emission of the lower atmosphere. As a result, both terms in Eq. (3.3.1) must be taken into account.

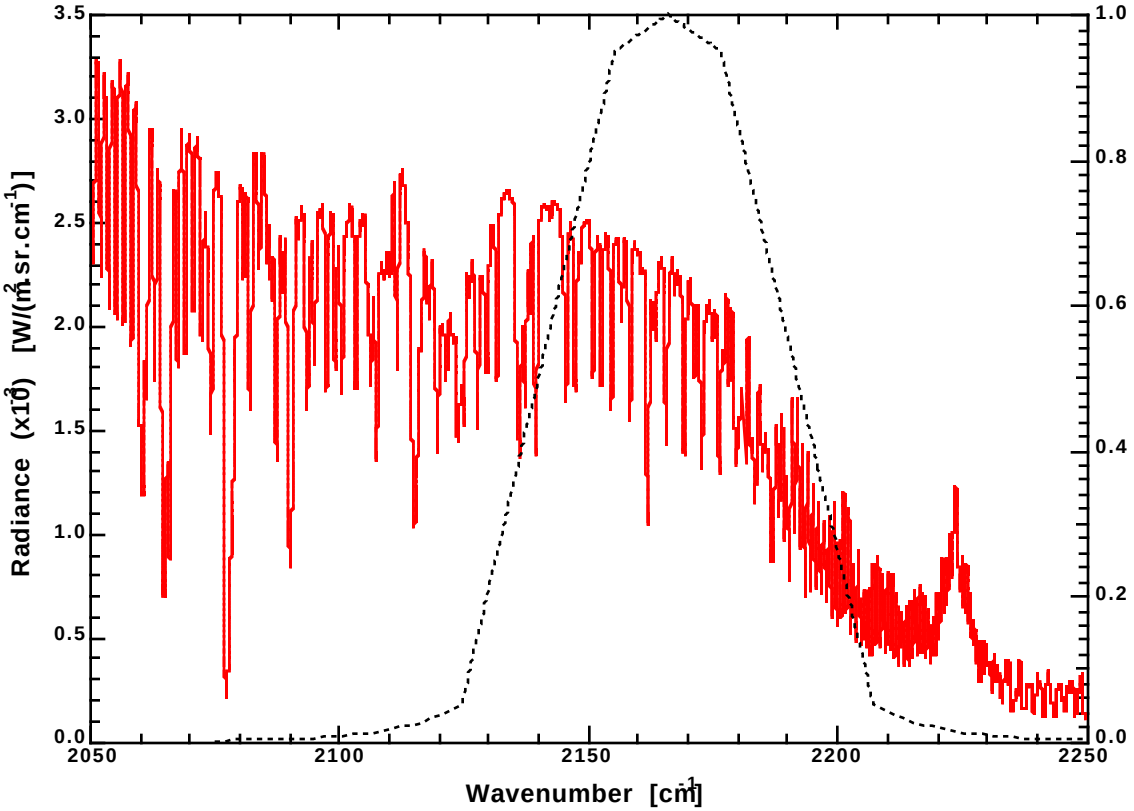

Figure 3.1.3 The total atmospheric radiance for a nadir view of the Earth surface in the 4.7 μm spectral region. The calculation assumes the U.S. Standard Atmosphere and a Lambertian surface with temperature and emissivity of 289 K and 0.98, respectively. The spectrum is calculated at a resolution of 0.5 cm^{-1}. The CO thermal channel passband is also indicated.

3.1.4 The CO and CH_4 Solar Channels

The CO short-wave channel utilizes reflected solar radiation for making the total column retrieval. It spans the *R*- branch of the first excited band at 2.3 μm and the provisional spectral bandpass is set at 4265-4305 cm^{-1}. This is a relatively weak band, and considerations of signal-to-noise and the effect of contaminating gas absorption from H_2O and CH_4 are important. The CH_4 short-wave channel has a wide bandpass, provisionally 4360-4500 cm^{-1}, and covers several spectral bands. This is a relatively clean channel in terms of contaminating atmospheric absorption from other gases, with only weak interfering lines of H_2O, CO_2, and N_2O present.

The atmospheric transmittance of the optically active gases in the spectral region of the CO and CH_4 solar channels is shown in Figure 3.1.4. Figure 3.1.5 shows the nadir-viewing atmospheric radiance with the reflected solar radiation modified by atmospheric absorption. In the 2.3 and 2.2 μm bands, the signals are dominated by the reflected solar radiation, i.e., the radiance is

dominated by the second term on the left of Eq. (3.1.2). Neglecting scattering, Eq. (3.1.1) simplifies to:

$$I^{CLEAR}(\nu,h) = I_O(\nu)\tau(\nu,h_s)r_s, \tag{3.1.3}$$

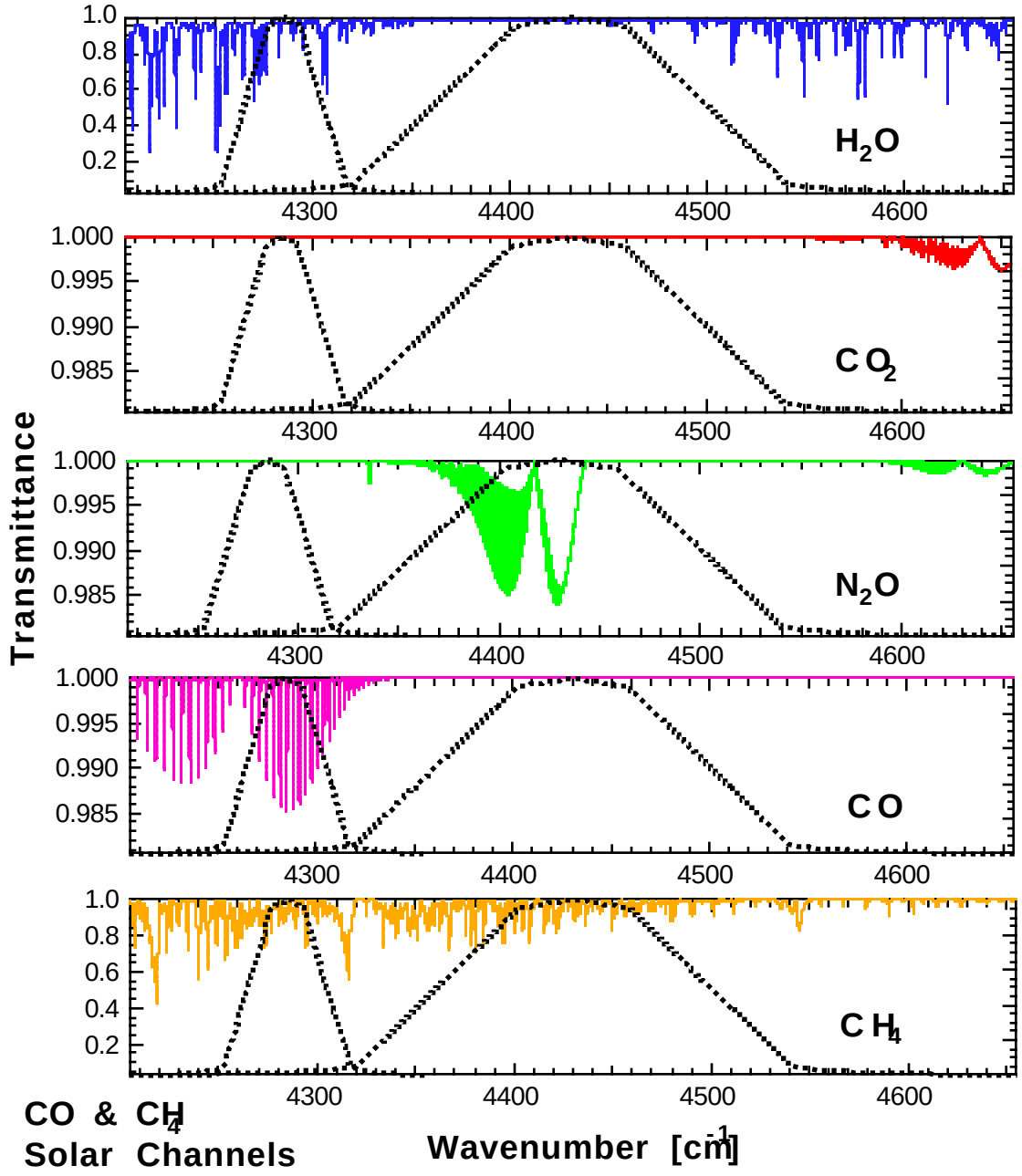

Figure 3.1.4 The atmospheric transmittance for a nadir view of the atmosphere over the 2.3 and 2.2 μm spectral interval. The transmittance of each of the important absorbing gases is shown individually. Spectra are calculated at a resolution of 0.5 cm^{-1}. Note the changes in transmittance scale. The CO and CH_4 solar channel passbands are also indicated.

where $r_S=(1-\varepsilon)$ is the surface reflectivity, I_O is the solar radiance, and $\tau(\nu,h_s)$ is the total transmittance for a slant path between the top of the atmosphere and the surface for a solar zenith angle of θ_{Sun}, and then upward to the observation point h at the satellite viewing angle with

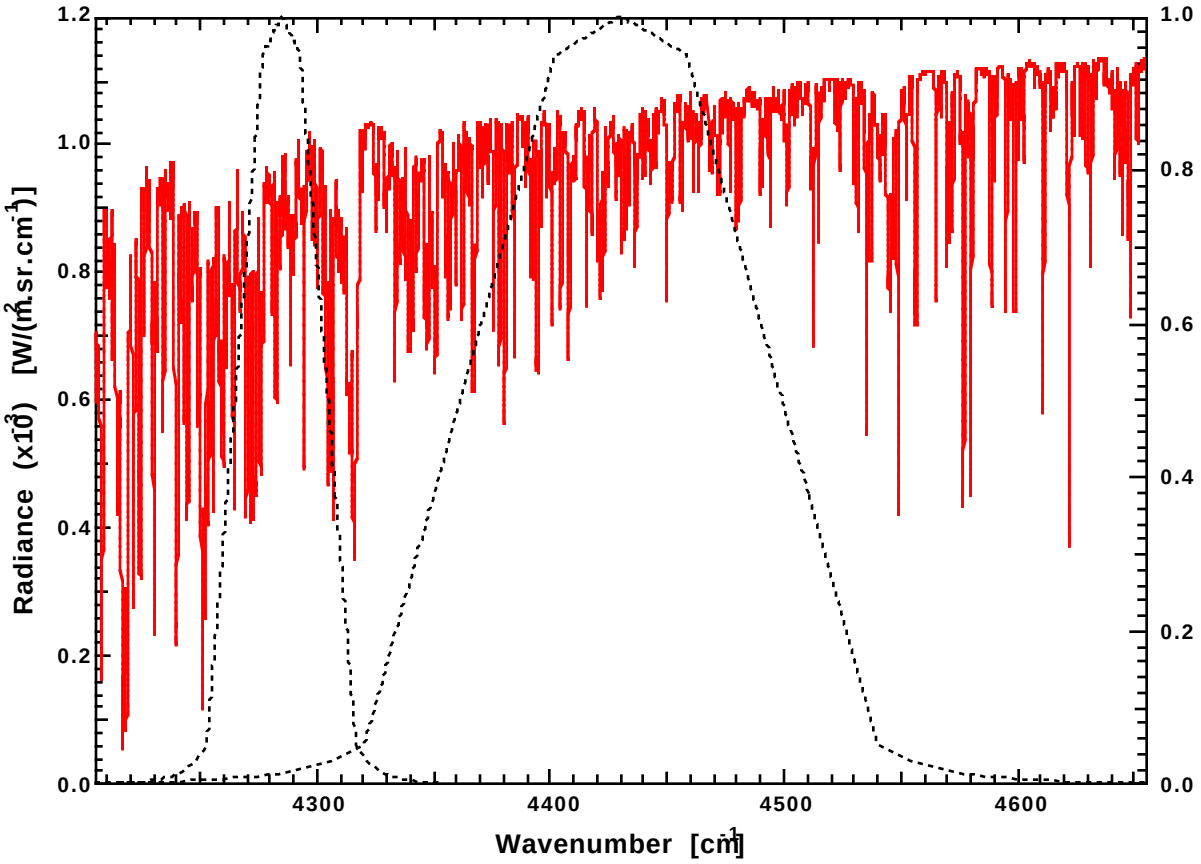

Figure 3.1.5 The total atmospheric radiance for a nadir view of the Earth surface over the 2.3 - 2.2 μm spectral region. The calculation assumes the U.S. Standard Atmosphere and a Lambertian surface with temperature and emissivity of 289 K and 0.90, respectively. The spectrum is calculated at a resolution of 0.5 cm^{-1}. The CO and CH_4 solar channel passbands are also indicated.

respect to nadir of θ_{sat}. This is a function of the total absorber density $\rho(z)$, and the mixing ratio $q(z)$, and absorption coefficient $k(\nu,z)$ of each gas, such that

$$\tau(\nu,h_s)=\exp\{-\int_{h_s}^{h} dz'(\sec\theta_{sun}+\sec\theta_{sat})\rho(z')\sum_n k_n(\nu,z')q_n(z')\}, \qquad (3.1.4)$$

where the summation is over all contributing absorbers n.

3.1.5 The Atmospheric Model

The forward model assumes the atmosphere to be plane-parallel. Atmospheric state parameters and the distributions of the gas constituents are constructed from climatological or meteorological data sources.

The model atmosphere is divided into layers for the radiative transfer calculation. Typically, 40 layers are used, of width 1 km in the first 30 km, and of a coarser structure in the upper atmosphere to 100 km. Each layer is considered as a homogeneous path for the transmittance calculation, and the temperature and pressure are represented by Curtis-Godson absorber weighted mean values. The integration over the total atmospheric absorption path then becomes a summation over the constituent layers.

In the clear sky calculations, the lower surface is treated as Lambertian (i.e., the reflected radiation is assumed to be unpolarized and isotropic, and is independent of the initial state of polarization and incident angle). This can be represented by a Planck function at temperature T_S and a constant emissivity. The effects of polarization and wavelength dependent emissivity within the MOPITT filter bandpass will be considered in future versions.

3.1.6 The Line-by-Line Radiative Transfer Model

Radiative transfer calculations are performed using the GENLN2 line-by-line transmittance and radiance model developed at Oxford University and NCAR (*Edwards, 1992*). The algorithm has been designed for speed of computation, and a modular structure serves as a basis for future modification and expansion. Calculations are performed for a multi-layered atmosphere of mixed gases, and several different viewing geometries are available. Optimal atmospheric layers are calculated and refraction and spherical geometry are considered when appropriate. Several line shapes and continuum absorption are available. A two stage spectral calculation is performed for regions close to and far from line center and there is a full treatment of line wings and of lines lying outside the spectral range of interest.

Spectral line parameters are presently taken from the 1992 edition of the HITRAN database (*Rothman et al., 1992*). The modeling of gas correlation spectroscopy requires accurate spectral line parameters. The spectral data for CO has been recalculated for the 1992 HITRAN database. The transition frequencies and line strengths do not, however, differ substantially from the 1986 HITRAN edition. The considered accuracies for the transition wavenumbers and the line strengths, are respectively, better than 10^{-4} cm^{-1} and 2-5%, for both the fundamental and first overtone bands. The other important parameters of air- and self-broadened half width and temperature dependence of the air-broadened half width are new or changed considerably for the 1992 edition. These are considered accurate within 5-10%. For CH_4, new laboratory results are included for the lines of interest in the 2.3 μm spectral region. The line positions are known to better than 10^{-3} cm^{-1}, and the strengths to within 5-10%. However, only average values are available for the line width parameters. The new 1996 version of HITRAN will be incorporated in the next version of the model.

The D-signals are in general much more sensitive to the accuracy of the line data than the A-Signals because a greater part of the signal comes from the position of the correlation line itself. Assuming the same spectral line data is used to model both the lines of the atmosphere and the lines of the correlation cell, then there is some compensation for uncertainties in line width and almost total compensation for uncertainties in line position. The latter is important only to the extent to which the overlap, with lines of the interfering species, changes. The calculation of MOPITT signals is most sensitive to the accuracy of the line strength data. This has the biggest effect on the high pressure LMR's that will be used to make total c42olumn measurements and provide profile information in the lower troposphere. As described in section 3.1.7, these radiometers have response functions that have broad peaks in the line wing and are zero close to

line center in the case of the D-response. They are non-zero, only away from the line center in the case of the A-response radiometers. If the line strength increases by the maximum uncertainty of 5%, more absorption takes place in the wing and the maximum signal change of 15.4% occurs for the 80 kPa double pass LMR D-Signal. The corresponding change in the A-Signal is 6.7%. The low pressure 2.5-5.0 kPa PMR is least affected with a 6.2% change in the D-Signal and a 0.2% change in the A-Signal. The low pressure PMR signals are most affected by uncertainties in the line width as these are sensitive to absorption in a very narrow part of the line profile at about one halfwidth from line center. For the maximum line width uncertainty of 10%, the maximum associated signal change is 6.1% and occurs for the 2.5-5.0 kPa PMR D-Signal. The corresponding A-Signal change is 0.27%. The high pressure 80 kPa LMR DP D-Signal and A-Signal are changed by 3.8% and 1.8%, respectively. A new version of HITRAN was released in 1996. In the spectral intervals of interest to MOPITT, there have been significant improvements to the CO line strength data in both bands following the work of Goorvitch (*1994*). The data for CH_4 are unchanged.

Gaseous absorption is modeled using the Voigt line shape with the exception of the H_2O absorption which is calculated using the line shape of Clough *et al.* (*1980*) to account for non-Lorentzian line wings and the water vapor continuum. H_2O line wings have cutoff at a distance of 25 cm^{-1} from the line center and at greater distances, the absorption is included using a precomputed continuum calculated using all lines and the appropriate line shape. GENLN2 uses two calculation grids. The spectral interval of interest is first divided into wide meshes, each with a typical width of 1 cm^{-1}. Each wide mesh is then sub-divided to give the high-resolution fine wavenumber grid. This grid spacing is chosen so as to adequately sample Doppler-broadened lines in the upper atmosphere. The far-line wing and continuum absorption, which change slowly with frequency, are calculated at three points within each wide mesh interval and then interpolated onto the fine grid. The calculation of spectral line absorption close to line center, which changes rapidly with frequency, takes place on the fine wavenumber grid. The high resolution spectroscopic calculation is essential for the MOPITT instrument modeling. Although the instrument measures integrated radiance over each passband, the gas correlation cells in front of the radiometers create a spectral response that filters the radiance with a very high spectral resolution.

Forward calculations needed for the retrieval process include the high resolution spectral transmittance for each layer of the model atmosphere, the spectral radiance at the top of the atmosphere, and the total signals for each radiometer. The calculation proceeds monochromatically, on a layer-by-layer basis, starting at the top of the atmosphere with a solar blackbody source function. In the downward part of the calculation, this radiation is followed to the Earth's surface through the atmospheric layers where it is absorbed by the radiatively active gases and also picks up a radiation component due to thermal emission. On reaching the surface, the radiation is reflected upwards together with the thermal radiation of the surface according to the surface emissivity. As this radiation proceeds from the surface to space, there is again absorption and emission by the atmospheric gases.

3.1.7 The Instrument Model

Both PMRs and LMRs are gas correlation radiometers in which the atmospheric radiation passes through a cell containing the same gas as the atmospheric gas which is being measured. The MOPITT radiometer has eight gas correlation channels. The six MOPITT cells contain: two pressure modulated cells and two length modulated cells for CO profile measurement and two length-modulated cells each for the CO and CH_4 total column measurements. Either the gas

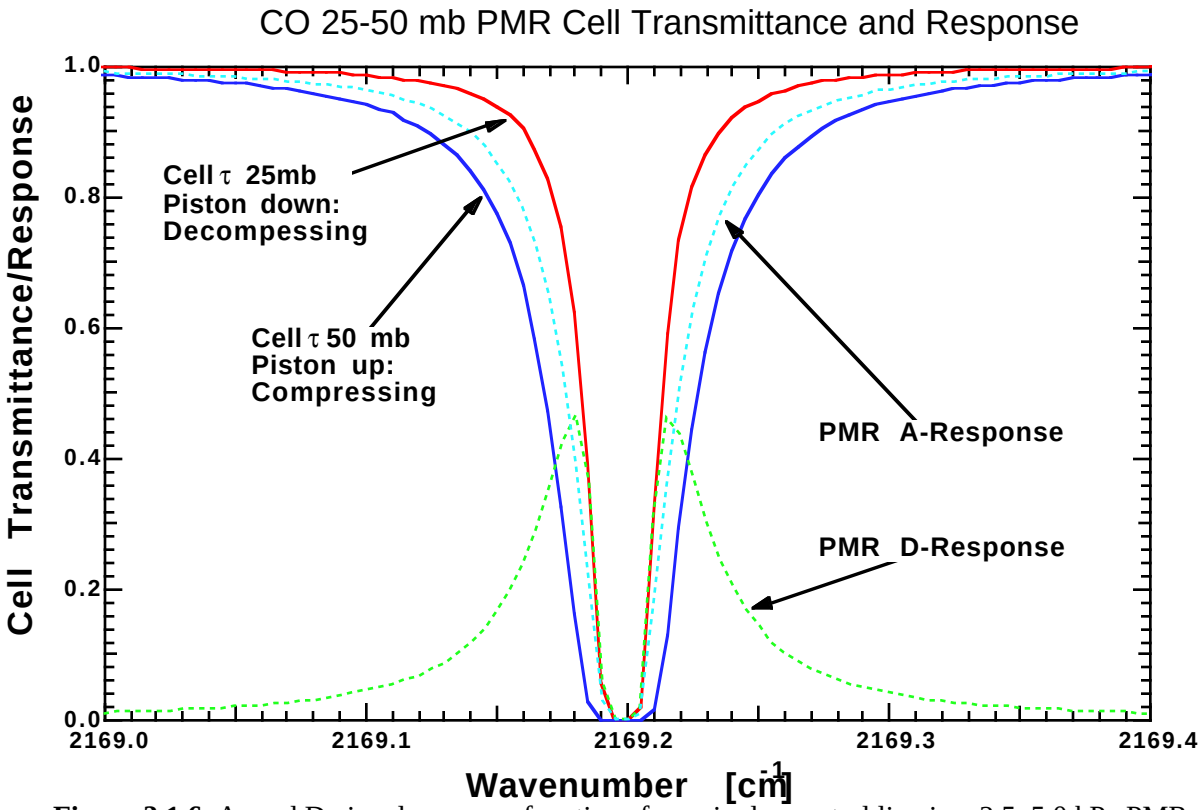

Figure 3.1.6 A- and D-signal response functions for a single spectral line in a 2.5–5.0 kPa PMR used in the CO thermal 4.7 μm measurement. The cell transmittances at 2.5 and 5.0 kPa are shown together with the difference (D) and average (A) responses of the cell. Atmospheric radiation will only reach the detector in spectral regions of non-zero response.

pressure inside the cell in the case of the PMR, or the effective gas cell length with the LMR, is modulated, resulting in a modulation in the opacity of the cell due to that component of the atmospheric radiation that was emitted by the cell gas species. As noted in Sec. 2.3.3, this produces fluctuations in the signal at the detector only inside the spectral lines of the gas species contained in the cell. Two signals are possible: the difference (D) signal and the average (A) signal. The D-signal results from differencing the signals for low and high cell opacity. The A-signal is achieved by asynchronously chopping the input signal with the modulation to measure the mean radiation transmitted by the cell. High effective resolution and signal-to-noise ratio are possible because contributions from all lines of the cell gas species are sampled. The principles and operation of the PMR are discussed in detail by Taylor (*1983*), and of the LMR by Drummond (*1989*).

The information content of the two signals, difference and average, are complementary to each other. The A-response function is low at the spectral line positions of the correlation gas and high at other positions. This provides information on the background radiance, which includes the surface emission and the absorption due to other atmospheric constituents. The D-response function is high only at the spectral line positions of the correlation gas and is nearly opaque for other spectral intervals. This signal provides the target gas information. This is illustrated for a 2.5–5.0 kPa PMR in Figure 3.1.6.

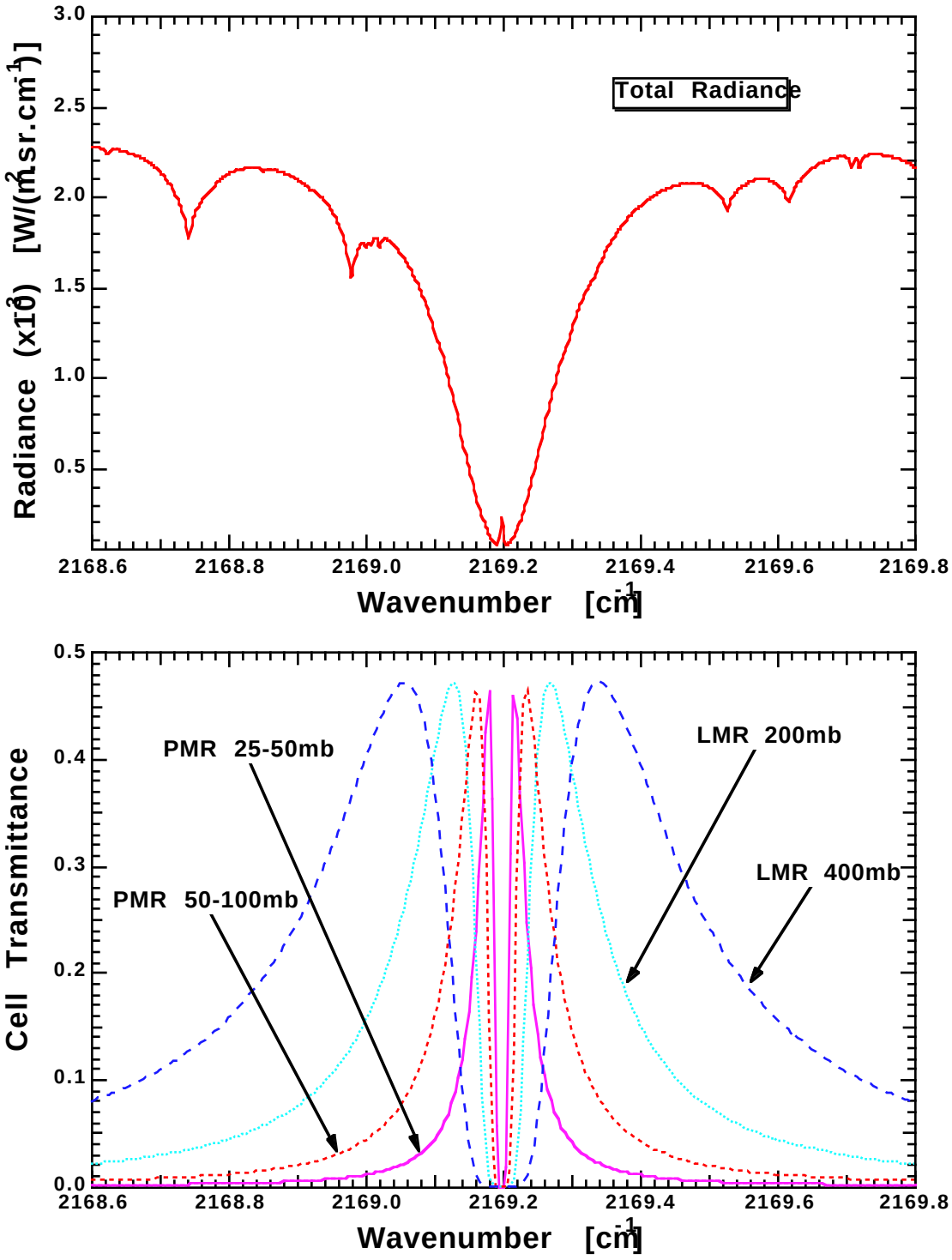

Figure 3.1.7 Total atmospheric radiance together with PMR and LMR D-response functions of a single CO line for a nadir view of the Earth surface in the 4.7 μm spectral region. The upper panel calculation assumes the U.S. Standard Atmosphere and Lambertian surface with temperature and emissivity of 289 K and 0.98, respectively. The spectrum is calculated at a resolution of 0.5 cm^{-1}. The lower panel shows the D-response of four gas correlation cells of different pressures which sample different parts of the line wing.

At the center of a purely collision broadened spectral line, the PMR cell absorption for a given cell length and temperature is independent of cell pressure, and the radiometer D-response is zero. Away from the line center, the D-response rises to a maximum and then decreases, the exact form depending on the optical thickness of the gas cell. For the optically thin case, the maximum occurs at line center $\pm\overline{\alpha_L}$, where $\overline{\alpha_L}$ is Lorentz half width evaluated at the cell mean pressure. If Doppler broadening is present, then the absorption at line center is greater during the high-pressure part of the modulator cycle and the response is greater than zero. In the case of the LMR, the D-response is a maximum at a line center in the optically thin case. However, the cell pressures needed for MOPITT are relatively large so that the cell is optically thick at the line center frequencies for most channels. This results in an LMR D-response function with a similar shape to that of the PMR.

The pressure or length modulation cycle used for the cell determines the part of the spectral line that is sampled. With increasing pressure in the correlation cell, the double peaks of the D-response function move outward from the line center. The lower pressure PMR D-response functions measure radiation from close to line center, while the higher pressure LMR D-mode has a maximum response in the line wing as shown Figure 3.1.7. Since the absorption of the upwelling surface radiation in the line wing takes place at lower altitudes, it is possible to derive information about the vertical CO profile by using a series of PMRs and LMRs at different pressures.

The goal of the forward model is to calculate the instrument signals under the conditions of the measurement. The signals measured by the MOPITT radiometers are the radiance at the top of the atmosphere, $I(\nu,h)$, convolved with the spectral response of the radiometer over the spectral passband $\Delta\nu$,

$$S_i^{A,D} = \int_{\Delta\nu} I(\nu,h) R_i^{A,D}(\nu) d\nu, \qquad i = 1,\ldots m \tag{3.1.5}$$

where $R_i^{A,D}(\nu)$ represents the average (A) or difference (D) radiometer response function for the ith radiometer.

The total radiometer response can be written as the product of the response profile of the channel blocking filter $G(\nu)$ and the gas correlation response, $H^{A,D}(\nu)$,

$$R^{A,D}(\nu) = G(\nu) H^{A,D}(\nu) \tag{3.1.6}$$

Assume now that the blocker response profile $G(\nu)$ varies very slowly over the wavenumber width of a GENLN2 wide calculation mesh interval of width $\delta\nu$ (typically 1 cm^{-1}). If there are N wide mesh intervals j, which need not have equal spacing, then Eq. (3.1.5) can be written

$$S_i^{A,D} = \sum_{j=1}^{N} \overline{G_j} \int_{\delta\nu_j} I(\nu,h) H_i^{A,D}(\nu) \mathrm{d}\nu \tag{3.1.7}$$

where

$$\overline{G_j} = \frac{1}{\delta\nu_j} \int_{\delta\nu_j} G(\nu) \mathrm{d}\nu. \tag{3.1.8}$$

The functions $G(\nu)$ and $H^D(\nu)$ for the MOPITT 4.7 μm CO thermal channel PMR are shown in Figure 3.1.9. Also shown is the resultant spectrum when the response function is convolved with the atmospheric radiance. The instrument signal is then the integral of this spectrum over the channel blocker response.

The PMR or LMR cycle can be represented as a linear combination of *K* gas cells, each containing the correlation gas. In the PMR case, each cell has the same length but the pressure and possibly the temperature differ according to the point that the cell represents on the modulation curve. With the LMR, the signal is alternated between just two gas cells of different length, with the pressure remaining constant. The gas correlation response is then approximated as a weighted linear combination of the monochromatic transmittances of each cell

$$H^{A,D}(\nu) = \sum_{k=1}^{K} a_k^{A,D} \tau_k(\nu)^{cell} \qquad (3.1.9)$$

where $\tau_k(\nu)^{cell}$ is the transmittance of cell *k* and $a_k^{A,D}$ is the weighting coefficient. In this way, the commonly used two-cell approximation is modeled by setting *K*= 2. Cell 1 is the high pressure or longer cell with $a_1 = -1$ for the PMR and LMR, respectively, and cell 2 is the low pressure or shorter cell with $a_2 = +1$. The gas correlation D-response in this case is

$$H^{D}(\nu) = \tau_2(\nu) - \tau_1(\nu). \qquad (3.1.10)$$

The two-cell A-signal calculation is modeled by setting both a_1 and a_2 to 0.5 with the same cell transmittances as in the D-signal case above. The figure 3.1.8 shows a measured pressure and temperature variation within the PMR cell. This can be modeled by defining cells with appropriate weights, at various times along the cycle with the corresponding temperature, pressure and gas amount.

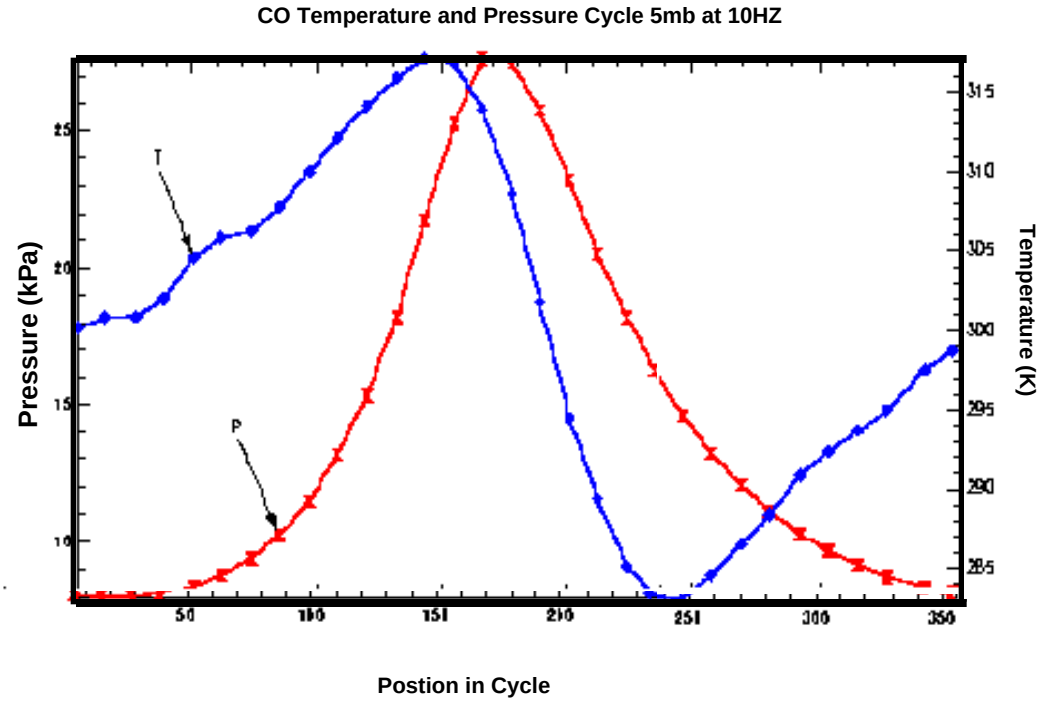

Figure 3.1.8 Measured pressure and temperature variation within the CO PMC

The gas correlation response function $H^{A,D}(\nu)$ depends on the pressure or length cycle of the PMR or LMR and the temperature cycle. Thus, the same function will be applicable to many

atmospheric radiance calculations that use the same PMR or LMR. The approach taken in GENLN2 is to pre-compute $H^{A,D}(\nu)$ for a particular PMR or LMR on the GENLN2 fine wavenumber grid and to store the result in a file for subsequent atmospheric calculations to use. This avoids duplication of cell transmittance calculations and makes possible a PMR representation with a larger number of composite cells.

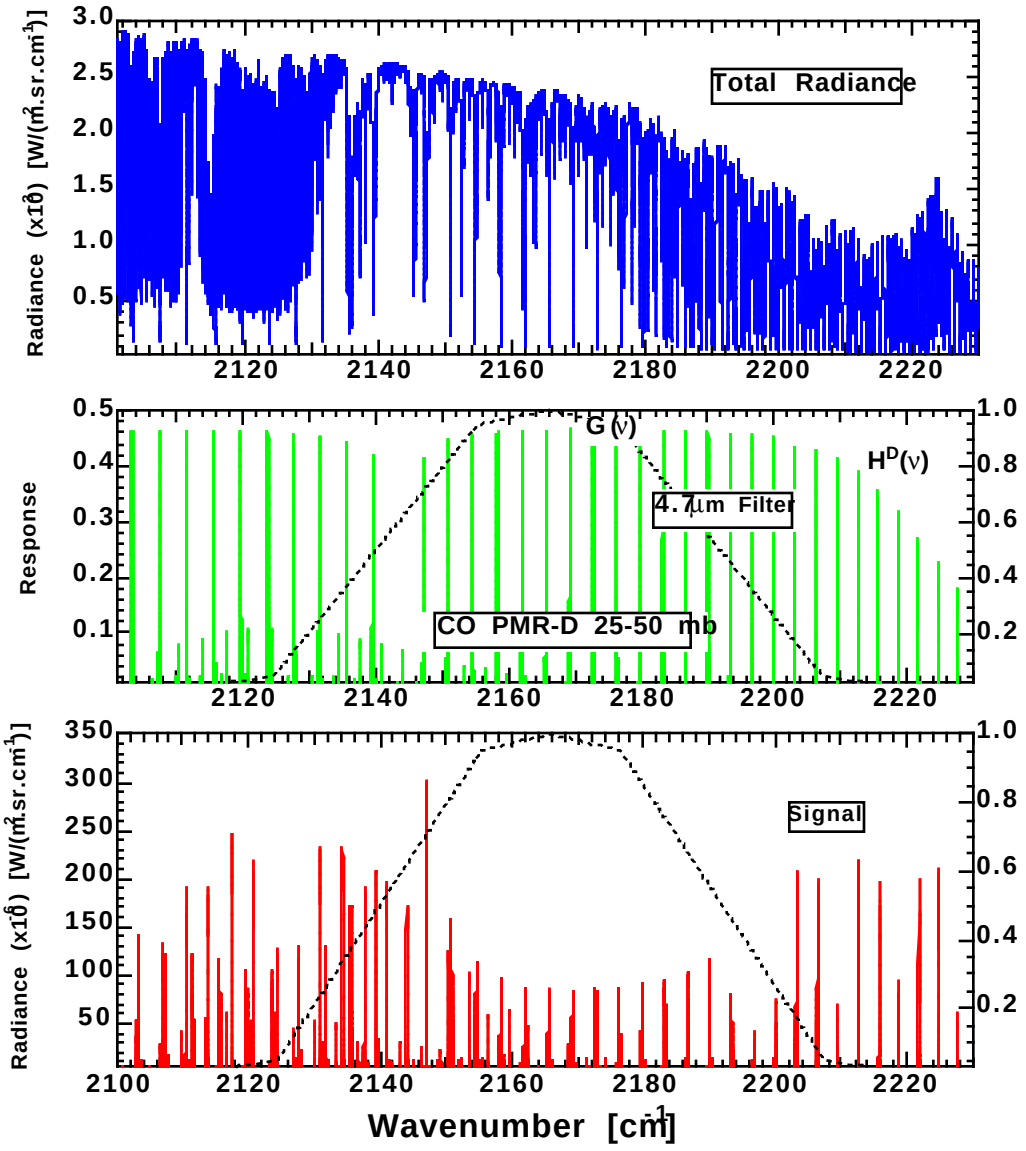

Figure 3.1.9 Three stages of the MOPITT measurements are illustrated in this figure. The top panel shows the total 4.7 μm nadir monochromatic spectral radiance for the U.S. Standard Atmosphere and a Lambertian surface with temperature and emissivity of 289 K and 0.98, respectively. The middle panel shows the CO 2.55.0 kPa PMR D-response function $H^D(\nu)$ together with the 4.7 μm filter profile $G(\nu)$. The bottom panel shows the result of the convolution of the atmospheric radiance with the D-response function.

Away from strong absorption lines of the cell gas, the response function $H^D(\nu)$ approaches zero. At such points it is unnecessary to compute the line-by-line atmospheric radiance. The GENLN2 wide mesh wavenumber boundaries are chosen such that they fall either side of regions of non-zero response. Wide meshes with zero response are then flagged. Because the response function and the wide mesh boundaries are input at the start of the GENLN2 calculation, line-by-line calculation in these meshes can be switched off to save time.

3.1.7.1. The Fast Transmittance Model (MOPFAS)

Full line-by-line calculations of atmospheric transmittance and radiance are too slow to be of practical use in forming the forward model of an operational retrieval scheme or even for developing prototype algorithms that are to be run for a large number of cases. It is, therefore, necessary to have a fast transmittance model that runs several orders of magnitude faster than the line-by-line calculation. It must be capable of reproducing channel transmittances and their dependence on the important variables of temperature, target gas amount, contaminating gas amount (particularly H_2O), and satellite and solar zenith angles. The fast model should also be able to calculate MOPITT channel radiances to within an acceptable accuracy when compared to the full GENLN2 (*Edwards, 1992*) line-by-line calculation.

The approach taken for the first version of the fast transmittance model, MOPFAS-1, was to use the method of McMillin and Fleming (*1976; Fleming and McMillin, 1977; McMillin et al., 1979; Susskind et al., 1983*). The code for MOPITT was based on a version of the model originally developed for the AIRS instrument (*Strow and Hannon, private communication, 1993*), and was the first time the method had been applied to an instrument with PMRs and LMRs.

The basic idea is that the transmittances from space, down to some atmospheric pressure level p_i can be parameterized as a function of the atmospheric state variables; temperature, mixing ratio, view angle, etc. If the transmittances are calculated accurately once using a line-by-line code for a reference atmosphere, then the transmittances for any test atmosphere may be obtained by perturbing the reference transmittances in a way that depends on the differences between the reference and test atmospheric state variable profiles. Because the integration in spectral space over the channel passband is computationally expensive, we deal here only with instrument function convolved transmittance $T(p_i)$. The following relation is used to calculate an effective layer (between consecutive pressure levels) transmittance for the test atmosphere,

$$\frac{T(p_i)}{T(p_{i-1})} = \frac{T(p_i)^{ref}}{T(p_{i-1})^{ref}} + \sum_j \alpha_{ij} \Delta X_{ji}. \qquad (3.1.11)$$

Here the j terms ΔX_{ji} for layer i, describe the differences between the reference and test atmosphere state variable profile. The corresponding fitting parameters α_{ij} must be determined. This is described in the following section.

3.1.7.2. Determination of Fitting Coefficients

Transmittances and profile differences with the reference atmosphere are first calculated for a diverse ensemble of training profiles. Using (3.1.11), the coefficients α_{ij} can then be calculated in each case. Finally, a least-squares fit is made to obtain the best values α_{ij} for the entire ensemble.

3.1.7.2.1 Training profiles

Since the fast model will be used to calculate transmittances for a wide range of atmospheric conditions, the expected variation must be represented in the diverse ensemble of training

profiles that go into the least-squares fit. The training profile set has been constructed using the NCAR 3D chemical transport model (*Muller and Brasseur,1995*) for a general global climatology together with measurements to provide profile extremes, such as very high CO amounts in a polluted boundary layer. A total of 57 profiles form the training ensemble.

3.1.7.2.2 Transmittance calculations

GENLN2 is used to calculate monochromatic transmittance spectra for each of the training profiles. Transmittances are formed from space down to each pressure level at several zenith angles θ through the atmosphere. For each MOPITT channel in turn, the resulting spectra $\tau(p,\nu)$ are convolved with the instrument channel response function *R*, to form the channel transmittances,

$$T(p_i) = \int R(\nu) \prod_i \tau(p_i,\nu) \frac{B(p_i,\nu)}{\bar{B}(p_i)} \, d\nu. \qquad (3.1.12)$$

The overbar signifies a channel quantity spectrally averaged. The Planck function term helps ensure the correct emission frequency variation in the final radiative transfer equation.

In the fast transmittance model, we wish to describe the change in channel transmittance for independent variations in the profile amounts of the target and contaminating gases. In order to do this, we need to form separate transmittance quantities for each gas that we will consider independently, and a least-squares fit can be performed to generate separate fitting coefficients.

Because there is a considerable amount of line overlap between the gases, their transmittances cannot be considered independently. Assume here that we can divide the gases of interest into three groups; fixed gases such as CO_2, whose mixing ratio profiles will be assumed the same everywhere, the target gas, which will be either CO or CH_4, and a variable gas, such as H_2O. We can form gas dependent transmittance quantities that take into consideration line overlap using the build-up method described below.

The GENLN2 line-by-line calculations and MOPITT channel response function convolutions are performed:

(i) for the fixed gases on their own, yielding T_F',

(ii) for the fixed and target gas combined monochromatically and then convolved, T_{FT}',

(iii) for the fixed, target, and variable gases combined monochromatically and then convolved, giving T_{FTV}'.

Representative channel transmittances for the three groups are then defined as,

$$T_F = T_F', \qquad T_T = \frac{T_{FT}'}{T_F'}, \quad T_V = \frac{T_{FTV}'}{T_{FT}'}. \qquad (3.1.13)$$

This formulation has the property that the product of the components reproduces the exact result,

$$T_F \times T_T \times T_V = T_{FTV}'. \qquad (3.1.14)$$

The fitting is then performed separately for each of T_F, T_T, and T_V.

3.1.7.2.3 Determination of predictors

The j predictor quantities ΔX_{ji} in (3.1.1) involve differences in layer i between the training profile quantities and the reference profile. These are determined to a certain extent by trial and error to discover quantities that determine the way in which the transmittance varies through the atmosphere. Suitable predictor elements of ΔX_{ji} include,

$$\Delta T_i = (T_i - T_i^{ref}), \quad \Delta T_i^2, \quad \Delta u_i = (u_i \sec\theta - u_i^{ref} \sec\theta^{ref}), \quad \Delta u_i^2, \tag{3.1.15}$$

where T is the temperature and u the layer absorber amount. To take account of the profile differences above the current layer in determining the layer transmittance, we include weighted terms such as

$$\Delta T_i^{*} = \frac{\int_0^{p_i} \Delta T(p)\mathrm{d}p}{\int_0^{p_i} \mathrm{d}p}, \quad \Delta T_i^{**} = \frac{\int_0^{p_i} \Delta T(p)p\mathrm{d}p}{\int_0^{p_i} p\mathrm{d}p}, \quad \Delta T_i^{***} = \frac{\int_0^{p_i} \Delta T(p)\sec\theta u\mathrm{d}p}{\int_0^{p_i} \sec\theta u\mathrm{d}p}. \tag{3.1.16}$$

At this stage the least-squares fitting can be performed to find the best values for α_{ij} for each of the three gas components.

3.1.7.2.4 Use of the fast model MOPFAS-1

Once the fitting coefficients have been determined, the model may be used to calculate the effective layer transmittances for a test profile presented by the retrieval algorithm. The values of ΔX_{ij} are first calculated between the test and reference profiles for the three gas components using (3.1.5) and (3.1.6), and then (3.1.1) is used along with the reference atmosphere transmittances to obtain the test atmosphere effective layer transmittances for each gas component.

The transmittances are then used in the MOPFAS radiative transfer calculation to obtain the MOPITT channel radiance at the top of the atmosphere according to,

$$S = \varepsilon T_N \overline{B}_s + (1-\varepsilon) T_N \left[\bar{I}_\Theta T_N + \sum_{i=1}^{N} (T_{i-1} - T_i)\overline{B}_i \right] + \sum_{i=N}^{1} (T_{i-1} - T_i)\overline{B}_i, \tag{3.1.17}$$

where ε is the surface emissivity, and $\bar{I}_\Theta$ the solar source radiance. The first term on the right of (3.1.17) represents surface emission, the second term, the reflected downwelling solar and thermal radiation, and the third term, the upwelling atmospheric emission.

The MOPFAS-1 model is currently used in the retrieval algorithm and was included as part of the MOPITT algorithm Beta delivery. MOPITT channel radiances are calculated to better than 0.5% compared to the full line-by-line calculation and are some 10^5 times faster. The full MOPFAS-1 calculation scheme is shown in Figure 3.1.10.

3.1.7.3. Development of MOPFAS-2

A completely new code, MOPFAS-2, is currently under development and will replace MOPFAS-1 in the MOPITT processing sometime in the autumn of 1996. MOPFAS-2 uses the OPTRAN regression scheme developed by McMillin *et al*. (*1995a,b*).

Transmittance through the atmosphere is essentially a function of the absorber amount. The absorber amount from space down to a given pressure level can vary dramatically with location and season. It also scales with the secant of the zenith angle for a given view geometry and atmospheric profile. This suggests the use of a column amount reference grid rather than a pressure grid on which to fit the transmittance. This is shown in Figure 3.1.11 where the CO

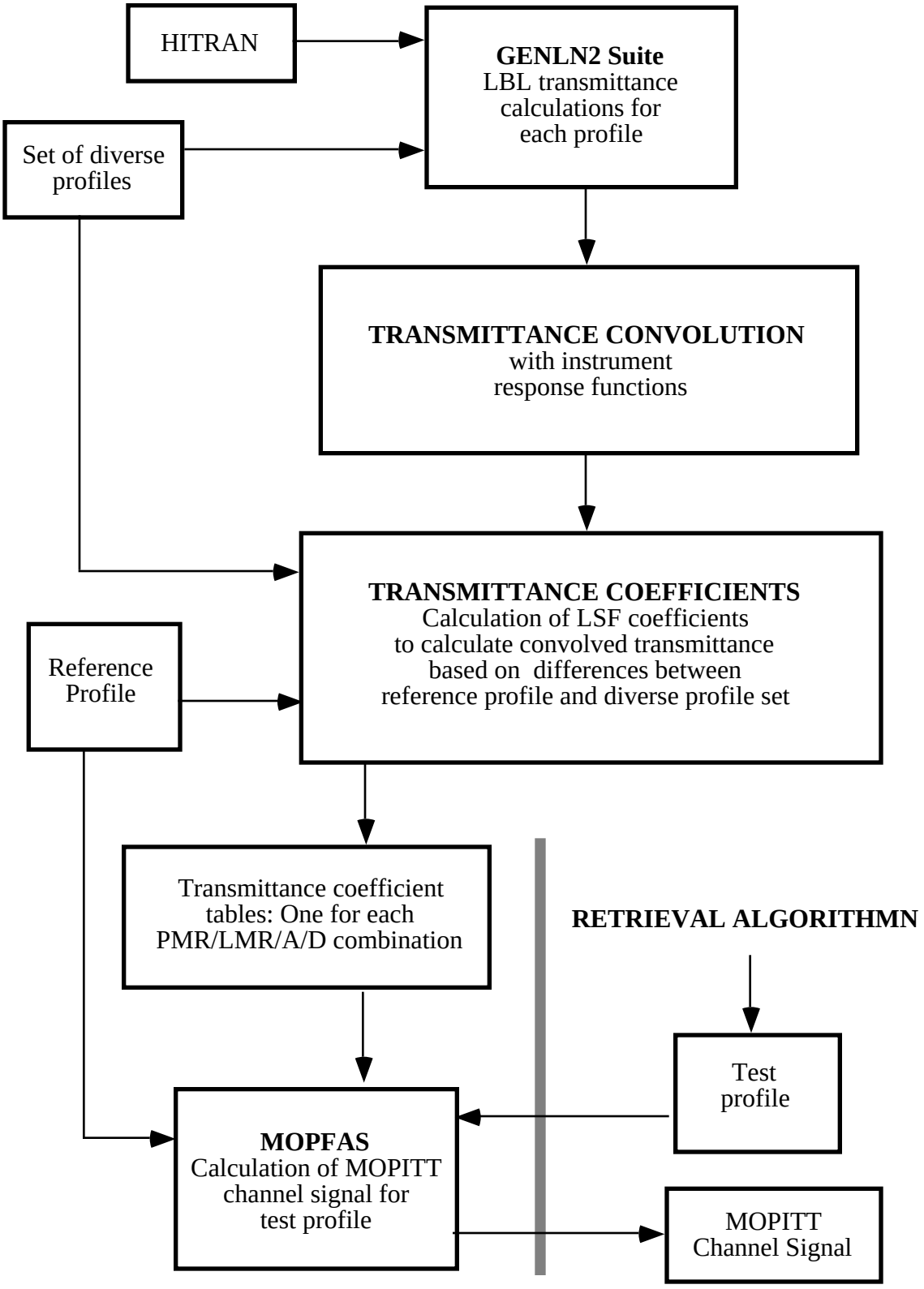

Figure 3.1.10. Flow diagram of MOPFAS fast transmittance calculation.

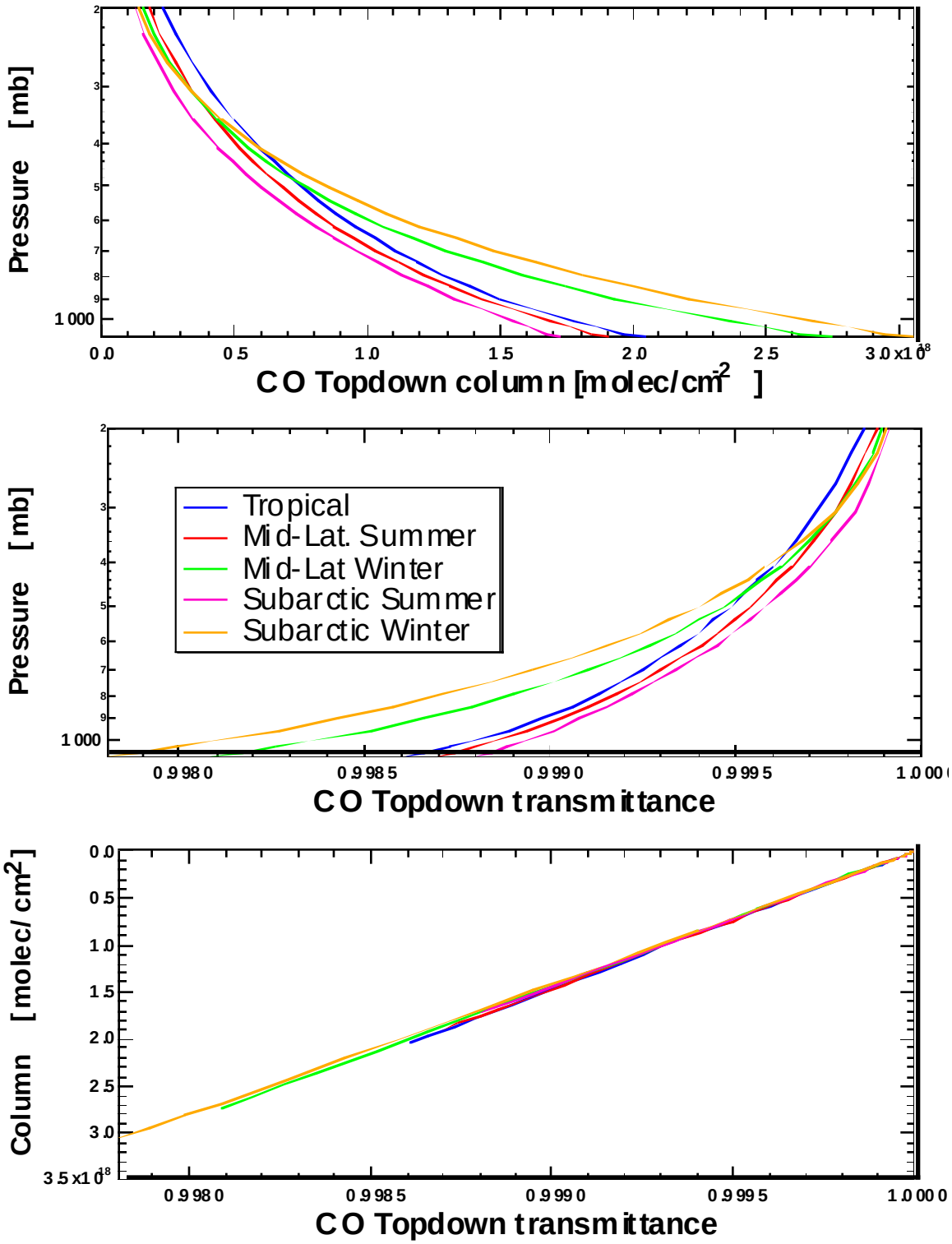

Figure 3.1.11. Dependence of transmittance on column amount for five different atmospheres and the D-signal of an 80.0 kPa double-pass CO solar channel LMR.

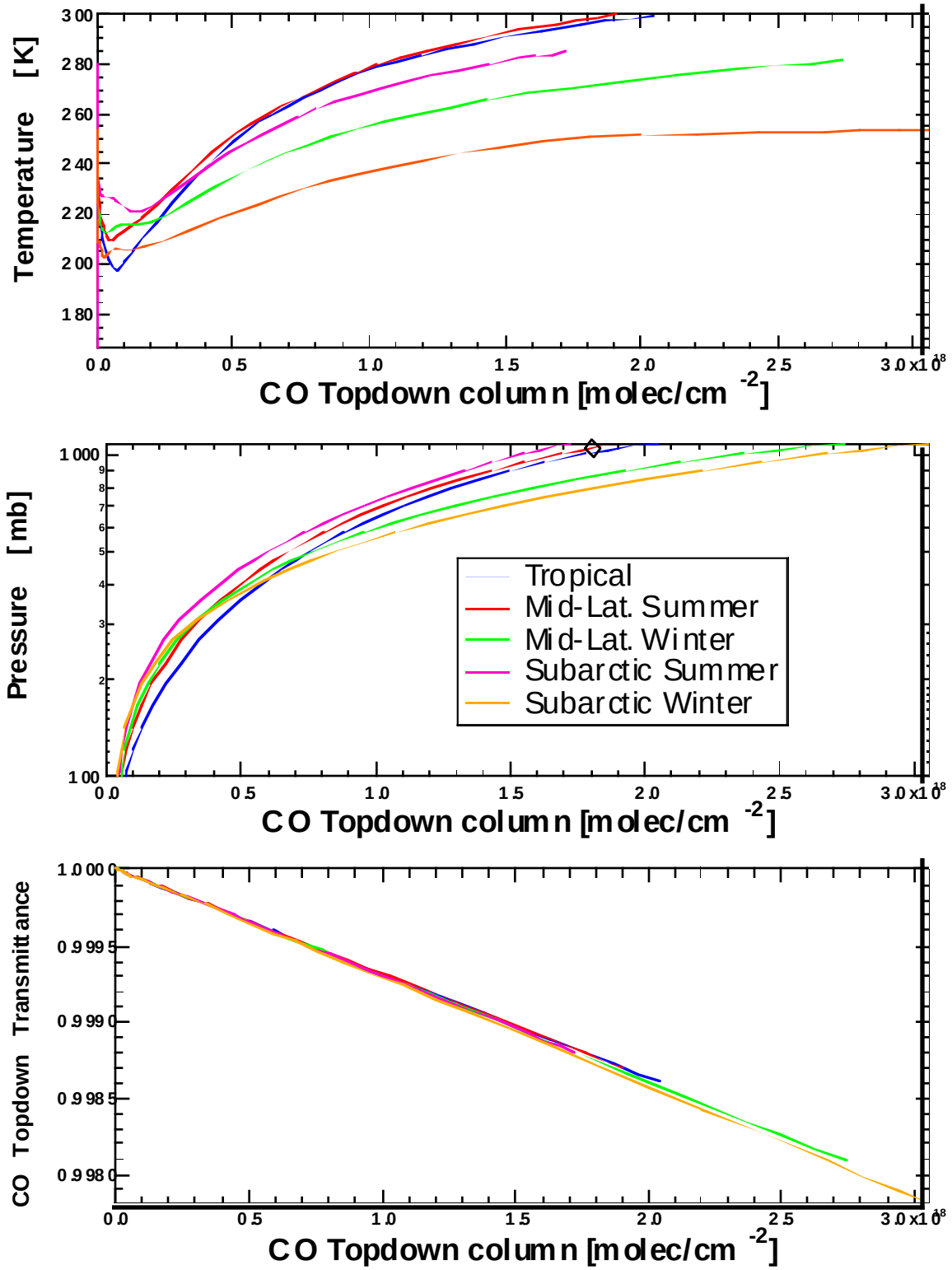

Figure 3.1.12. Interpolation of training profile quantities from the pressure to absorber amount grid for the example of Figure 3.1.11.

absorber column and transmittance for the D-signal of an 80.0 kPa double-pass CO solar channel LMR are shown as a function of pressure for five different atmospheric profiles. When transmittance is plotted as a function of column amount, an almost linear relation is obtained which does not vary greatly with atmospheric profile.

Therefore, if transmittance were to be fitted on the column amount grid, the relation between transmittance and absorber amount would become implicit, and terms containing pressure and temperature at given absorber amount would become predictors of small changes in transmittance. Also, because absorber amount depends on ray angle, view geometry is automatically accounted for.

3.1.7.3.1 Determination of MOPFAS-2 fitting coefficients

The new method uses essentially the same techniques described above for MOPFAS-1, only now the fitting of transmittance takes place on the column amount grid according to,

$$\frac{T(A_k)}{T(A_{k-1})} = \frac{T(A_k)^{ref}}{T(A_{k-1})^{ref}} + \sum_j C_{kj}\Delta Z_{jk}, \qquad (3.1.18)$$

where $T(A_k)$ is the MOPITT channel transmittance from space to absorber amount level k for one of the three gas components, fixed, target, and variable; C_{kj} are the j fitting coefficients in layer k, and ΔZ_{jk} are the corresponding predictors.

The calculation scheme is as follows. The MOPITT instrument function convolved transmittances are calculated on a pressure grid using the GENLN2 line-by-line code for an ensemble of training profiles as before. The calculations are again performed for the three gas components and different zenith angles. The atmospheric profile quantities and transmittances of each of the training atmospheres are then interpolated onto the absorber amount grid k of the particular gas component. This is illustrated in Figure 3.1.12. One of the profiles is chosen as the reference. The maximum column amount that can be fitted will be determined by the reference profile and therefore this has to be chosen with care so that the full range of expected atmospheric column amounts can be accommodated.

Absorber amount grid layer difference predictors ΔZ_{jk}, of j weighted quantities involving T, p, and θ, that affect the transmittance are taken between each training profile in the ensemble and the reference profile. A least-squares fit is then used to calculate the best fitting coefficients C_{kj} that relate the ensemble profile effective layer transmittances to those of the reference profile as a function of ΔZ_{jk}.

3.1.7.3.2 Use of the fast model MOPFAS-2

The fitting coefficients C_k, reference atmosphere column amount grid A_k and corresponding transmittances $T(A_k)^{ref}$ are stored in the program. When the retrieval algorithm presents a test profile, the temperature and pressure are interpolated onto the reference column amount grid. The predictor quantities ΔZ_{jk}, can then be formed for each layer and (3.1.18) used to determine the test profile absorber amount layer transmittances. These transmittances are then interpolated back to the original pressure grid and used in the radiative transfer equation (3.1.17) as before.

Early tests of this model show it to be considerably more accurate than the MOPFAS-1 model. Care has to be taken that the two interpolation stages involved in MOPFAS-2 are coded very

efficiently so as not to adversely impact run time. The fact that this is a completely new code has allowed us to address this effectively.

3.2 Cloud Detection and Filtering Algorithm

The attenuation of radiation by clouds in the MOPITT field of view will have a significant impact on the signals measured at 2.2μm, 2.3μm and 4.7μm. In a four-year cloud study by Wylie et al.(*1994*), using High Resolution Infrared Radiation Sounder (HIRS) data, they found only 23% of the observations were cloud free. HIRS has a field of view of 20 km which compares well to the 22x22 km field of view of MOPITT. Thus MOPITT can expect over 75% of the observations to be cloud contaminated.

Clouds can generally be classified according to the altitudes they predominately exist at in the atmosphere. Low clouds, such as stratus and cumulus, are found at altitudes below 70.0kPa. Middle clouds are found between 70.0kPa-40.0kPa, this class usually contains altostratus, nimbostratus and altocumulus clouds. High clouds are found above 40.0kPa, this class can contain cirrus, cirrostratus, cirrocumulus and the tops of cumulonimbus clouds. Wylie's study (*1994*), using a CO_2 slicing technique, found that low clouds were present in 26% of the observations, middle clouds were present in 27% of the observations and 24% of the cases contained high clouds. They also found that 42% of the observations contained evidence of cirrus clouds.

Using only cloud free sites would not allow enough coverage to give detailed information on CO/CH_4 distributions. This amount of coverage would also limit the understanding of methane and carbon monoxide distribution relationships to meteorological and cloud processes. Finally, limited coverage could also result in a statistically biased data set. The MOPITT field of view of 1.8 degrees and the temporal and spatial variability of clouds, make it necessary to develop an algorithm whereby MOPITT can identify areas that are clear, overcast or contain broken clouds.

The objective of this section is to describe a cloud detection and filtering algorithm to identify and evaluate clear and cloudy pixels based on data available to MOPITT at launch. Once a pixel has been designated as cloud contaminated, it then goes through a cloud clearing algorithm and the results are flagged. The methodology is designed so that a cloud need not cover the entire MOPITT field of view, however, the spectral cloud forcing must be greater than the instrument noise and background profile noise to be detected. Post-processing implementation of a cloud mask from the MODIS EOS-AM instrument is also described

3.2.1 Physics of the Problem: Cloudy Sky Radiance

The interaction of solar radiation and thermal emission with clouds is a function of the cloud particle characteristics. Optical thickness and effective radius are often used to describe how incident radiation reacts with a cloud and used to evaluate empirical measurements with theoretical models. Optical thickness is determined by the wavelength of incident radiation, physical nature of the particles (ice crystals, drops, droplets), their concentration and vertical extent of the cloud. The effective radius is defined as (*Hanson and Travis, 1974*)

$$re = \int r^3 n(r) dr / \int r^2 n(r) dr , \qquad (3.1.1)$$

where r is particle radius, and n(r) is particle size distribution.

In the solar channels, at 2.3 -2.4μm, Nakajima and King (*1990*), Nakajima *et al.* (*1991*) and King *et al.* (*1990*), have evaluated the reflectance of water clouds as a function of optical thickness and effective radius at 2.14μm. Their results show that at 2.14μm, cloud reflectance

increases asymptotically with increasing optical thickness, leveling off as the solar absorption of droplets increases. Warren (*1984*) determined that at 2.2-2.3μm, ice particles have a negligible absorption coefficient and reflectance is dependent on particle size, increasing as the particle size decreases.

In the thermal channel, at 4.7μm, the distinction between a cloud and its underlying surface is due not only to the reflectance properties of the cloud but also the clouds thermal emission. Hanson and Pollack (*1970)* show that in the near infrared, liquid water clouds are distinguished by a dominate thermal emission factor, while ice clouds can have equal contributions of thermal emission and solar reflectance. The 4.7μm channel is also sensitive to thermal emission through semi-transparent clouds, resulting in a reduction of surface contrast and increased difficulty in determining the presence of optically thin clouds.

The radiative transfer equation for a clear air radiance was given in Eq. 3.1.1. The radiative transfer equation for a cloud covered field of view is given by,

$$I_{i,k}^{CLOUD} = \varepsilon_{ic_k} B_i\left(T_{c_k}\right)\tau_i\left(h_{c_k}\right) + \int_{h_{c_k}}^{h} B_i\left[T(z)\right]\left(\frac{d\tau_i}{dz}\right)dz$$
$$+\rho_{ic_k}^{'} H_i \tau_i^{'}\left(h_{c_k}\right)\cos\theta_0 + I_i^{\downarrow} + I_{i,k}^{SCAT} + \tau_{ic_k} I_i\left(h_{c_k}\right)\tau\left(h_{c_k}\right) \qquad (3.2.2)$$

where $I_{i,k}^{CLOUD}$ is the channel *i*, radiance containing cloud type *k*, at the top of the atmosphere. The radiative transfer equation, due to varying cloud properties c_k, has additional terms not included in the clear air radiance. The first term on the right is the radiation reaching the instrument from the cloud. The second term gives the contribution to the total radiance from atmospheric self emission between the surface and the instrument. The third term is the radiation that is reflected off the cloud top in the direction of the satellite. The fourth term is the downwelling thermal emission from the atmosphere. The fifth term is the effect of scattering on the channel and the last term is the radiation from the ground that is transmitted through the cloud. The pixel number is represented by *j*. There are four 22x22 km pixels in each MOPITT stare.

3.1.1 Mathematical Description of the Cloud Algorithm

The cloud cleared radiance is the radiance that would have been measured by the instrument if no clouds were present in the field of view. The majority of cloud clearing techniques are based on the *n** approach (*Smith,1968*) which utilizes information from adjacent pixels. The algorithm assumes that radiance from two spatially independent but geographically close locations differ only in the amount of fractional cloud cover in the scene. If clouds are present at a uniform altitude, over similar terrain, then the clear air radiance is the same for both fields of view.

If α represents the fraction of the pixel scene containing a single cloud, then the observed radiance is given by,

$$I_i^{obs} = \left(1 - \alpha I_i^{CLEAR}\right) + \alpha I_i^{CLOUD} \qquad (3.2.3)$$

Following the approach developed by Joiner et al. (*1995*) for the AIRS instrument, their cloud clearing methodology can be applied to the MOPITT radiometer channels, *i*. For multiple cloud types *k*, Eq. 3.2.3 becomes,

$$I_i^{obs} = \left(1 - \sum_k \alpha_k\right) I_i^{CLEAR} + \sum_k \alpha_k I_{i,k}^{CLOUD} \qquad (3.2.4)$$

For each channel, the reconstructed clear column radiance, $\tilde{I}_i$ is calculated as,

$$\tilde{I}_i = I_{i,1}^{OBS} + \eta_1\left[I_{i,1}^{OBS} - I_{i,J+1}^{OBS}\right] + ... + \eta_j\left[I_{i,1}^{OBS} - I_{i,(J+2)-j}^{OBS}\right] + ... + \eta_J\left[I_{i,1}^{OBS} - I_{i,2}^{OBS}\right] \quad (3.2.5)$$

Using the adjacent four pixels in one MOPITT stare ($J+1 = 4$), up to three cloud types ($K=3$), can be determined from the sixteen radiometer channels (I=16), by solving the following set of linear equations:

$$\begin{pmatrix} I'_{1,CLEAR} - I_{1,1} \\ I'_{2,CLEAR} - I_{2,1} \\ I'_{I,CLEAR} - I_{I,1} \end{pmatrix} = \begin{pmatrix} I_{1,1} - I_{1,J+1} & I_{1,1} - I_{1,J} & I_{1,1} - I_{1,2} \\ I_{2,1} - I_{2,J+1} & I_{2,1} - I_{2,J} & I_{2,1} - I_{2,2} \\ I_{I,1} - I_{I,J+1} & I_{I,1} - I_{I,J} & I_{I,1} - I_{I,2} \end{pmatrix} \begin{pmatrix} \eta_1 \\ \eta_2 \\ \eta_J \end{pmatrix} \quad (3.2.6)$$

In matrix form Eq. 3.2.6 becomes

$$\boldsymbol{A} = \boldsymbol{B}\eta \quad (3.2.7)$$

A least squares solution can be used to determine η.

3.2.3 Uncertainty Estimates for the Cloud Algorithm

In this approach, cloud identification is based on contrast between scenes and the ability to detect a cloud signal which is larger than the instrument and background noise. Thus a noise covariance matrix is introduced into equation 3.2.7. The uncorrelated elements are found on the diagonal values of the channel noise covariance matrix *N*, and contain:

(i) Instrumental channel noise
(ii) Uncertainty in estimates of (I'_{CLEAR}–I_1)
(iii)Computational Error

$$N_{ii} = NE\Delta N_i^2 + \left(\Delta I_{i,surface}\right)^2 + \left(\Delta I_{i,Tsurface}\right)^2 + \left(\Delta I_{CO(p)}\right) + \left(\Delta I_{CH_4(p)}\right) + \left(\Delta I_{H_2O(p)}\right) + \left(\Delta I_{T(p)}\right) + C \quad (3.2.8)$$

Instrumental channel noise, is from the MDD *document (Drummond et al., 1993*) and will be adjusted for measured noise levels after launch. Uncertainty estimates will be determined from experimental data and simulation studies. Computational errors will be held as a constant and determined empirically.

The solution to A = Bη becomes:

$$\eta = \left(B'W^{-1}B\right)^{-1} B'W^{-1}A \quad (3.2.9)$$

where *W*, is the inverse of the channel noise covariance matrix *N*.

A solution for η, cannot be determine if the term $(B'W^{-1} B)$ is effectively singular. In these cases, the radiance will be rejected and flag accordingly. Once η is determined the cloud cleared radiance $\tilde{I}_i$ can be calculated using Eq. 3.2.5.

Sensitivity studies using the NCAR GCM (*Hack et al., 1993*) and the *CTM (Muller and Brasseur, 1995*) show that high clouds have a significant impact on all the MOPITT radiances. MOPITT is insensitive to clouds below 95.0kPa.

Future studies will determine if the correlated, off-diagonal, elements will need to be evaluated in the cloud retrieval algorithm. In addition to the noise covariance matrix, studies will also be developed to address the characteristics of cirrus clouds, semi-transparent clouds, cloud shadow and sun glint.

3.2.4 Practical Considerations for the Cloud Algorithm

The MOPITT cloud algorithm will evaluate the four pixels found in each MOPITT stare. First, radiances from the initial guess I'_{CLEAR}, will be generated. Second, to determine channel sensitivity to clouds, the radiances from a simulated overcast initial guess I'_{CLOUD}, will been generated. If $| I'_{CLEAR} - I'_{CLOUD} | <$ Limit, then the channel is insensitive to clouds. Only the channels that show a sensitivity to clouds will be used to determine η. The third step, after η has been determine, is to derive a set of cloud cleared radiances. Only the channels that are sensitive to clouds will have a η correction applied to them. Also, if the cloud cleared radiance minus the observed radiance is within limits, the radiances are declared clear.

The last step is to perform an internal validation. During the daytime the RMS for the CH_4 channel radiances, both clear and cloud cleared, will be evaluated. During the nighttime, the RMS of the CO channel will be evaluated. The nighttime radiance validation limits will have to be larger, due to the larger temporal and spatial variance of CO in the atmosphere. If the RMS of the radiances for one stare are within acceptable limits, they will be passed on to the retrieval algorithm.

3.2.5 Cloud Masking

After launch, cloud information may be available from other EOS_AM instruments. MODIS (*King et al., 1992)* is a high resolution radiometer with channels in the visible and infrared regions of the spectrum. MODIS will be generating a cloud mask at 250 and 1,000 meter resolution. The MODIS cloud mask would be interpreting the signal from the same atmospheric and surface signatures as the MOPITT instrument but on a much finer scale. Methods by which it would be appropriate to aggregate the 1 km MODIS cloud mask data up to a MOPITT, 22 km field of view will be investigated. Areas found to be completely clear by MOPITT, will be cross checked with the MODIS cloud mask. Flagging of MOPITT pixels, from cloud mask data, will occur at the same time the cross-track scans are analyzed.

The MODIS cloud mask algorithm starts with a single pixel (1000 m) and applies a series of infrared window brightness threshold and difference (BTD) tests to determine cloud conditions. The tests are separated into land/ ocean categories and are based on AVHRR cloud processing techniques. (*Ackerman et al., 1994*). The MODIS cloud mask (EOSDIS param 3660) is output as a 32-bit word for each MODIS field of view (see Fig. 3.2.1).

Decision	1	1=mask determined, 0=no decision
Summary of all algorithms 11> 99% prob of clear 10> 95% prob of clear 01> 66% prob of clear 00= cloud	2	unobstructed FOV (quality flag)
Ancillary information 1 snow/ice (1=no, 0=yes) 2 land/water (11=land, 10=wetland, 01=coastal, 00=water)	1	visible data (1=usable, 0=not usable)
Results from cloud algorithms 1 IR diff. - did not find clouds 1 CO2 high cloud test - no high clouds 1 Near IR test - no thin cirrus 1 SWIR threshold did not find cloud 1 visible ratio did not find cloud 1 cloud shadow not found	1	IR threshold did not find cloud
Additional tests	1 1	passed temporal consistency test passed spatial consistency test
250 m mask from vis tests	16	1=clear, 0=cloud for 16 FOV in 1 km FOV

Figure 3.2.1 MODIS cloud mask

3.3. CO Profile and Column Amount Retrieval for the Clear Sky and Cloud Cleared Radiances

3.3.1. Mathematical Description of the Algorithm

The MOPITT CO retrieval algorithm uses a maximum likelihood method that has been described by Rodgers (*1976*). The forward signal calculations uses the fast radiative transfer model, MOPFAS, as described in section 3.1**.** First, the retrieval program retrieves the CO profiles using all available measurement information. The CO column amount is then derived from an integration of the profile.

The forward equation for the CO profile retrieval problem can be written as:

$$\vec{y} = F(\vec{x}, \vec{b}) + \vec{N}_{\varepsilon}, \qquad (3.3.1)$$

where $\vec{y}$ is the measurement vector, $\vec{x}$ is the state vector, $\vec{b}$ represents all forward model parameters, $F(\vec{x},\vec{b})$ is the forward model function, $\vec{N}_\varepsilon$ is the instrument noise.

In our algorithm, the measurement vector, $\vec{y}$, is formed by measured radiances of all CO channels, as defined in Eq. (3.1.5). For the thermal band, A_i and D_i are used to represent the A and D signals for the *i*th radiometer. For the solar band, as indicated by Eqs. (3.1.3) and (3.1.5), the ratio S^D/S^A is independent of the surface parameters, as long as the spectral variation of ε over the bandpass is negligible. Our forward model study has also shown that the effect of interfering species is largely canceled when the ratio is taken. For these reasons, we define a R signal as the ratio of A and D signal, $R_i = D_i/A_i$. and use the R signals in the retrieval.

As indicated by Eqs.(3.1.1, 3.1.2) and discussed in section (3.1), thermal band signals depend on not only the atmospheric CO distribution but also several other atmospheric parameters and surface parameters. In our algorithm, the atmospheric temperature profiles and the distributions of interfering constituents such as water vapor, N_2O etc., are treated as known parameters. Their values will be provided by the EOS/AM platform as ancillary data. The effective lower surface temperature, T_s and thermal emissivity, ε, however, are treated as unknown parameters, along with the CO mixing ratios for a set of layers.

Using these notations, the measurement vector and the state vector can be written as:

$$\vec{y} = (S_i) = \begin{pmatrix} A_1 \\ \vdots \\ A_4 \\ D_1 \\ \vdots \\ D_4 \\ R_5 \\ R_6 \end{pmatrix}, \quad \vec{x} = (x_j) = \begin{pmatrix} \varepsilon \\ T_s \\ q_1 \\ q_2 \\ \vdots \\ q_m \end{pmatrix}, \tag{3.3.2}$$

where q_i represent a layer-average CO mixing ratio. The forward function is then linearized around an initial guess state vector $\vec{x}_0$:

$$F(\vec{x},\vec{b}) \cong F(\vec{x}_0,\vec{b}) + K\Delta\vec{x}, \tag{3.3.3}$$

and the matrix K is the weighting function:

$$K = \left(k_{ij}\right) = \left(\frac{\partial S_i}{\partial x_j}\right). \tag{3.3.4}$$

The maximum likelihood solution to Eq.(3.31) using a Newtonian iteration is:

$$\vec{x}_{n+1} = \vec{x}_0 + C_a K_n{}^T (K_n C_a K_n{}^T + C_\varepsilon)^{-1}\left[\vec{y} - \vec{y}_n - K_n(\vec{x}_0 - \vec{x}_n)\right], \tag{3.3.5}$$

where $\vec{x}_0$ is the *a priori* state vector and the initial guess for the retrieval, *n* is the order of iteration, C_a is the *a priori* covariance matrix for CO and the surface parameters,

$$C_a = E\left\{(\vec{x} - \vec{x}_0)(\vec{x} - \vec{x}_0)^T\right\} \tag{3.3.6}$$

and C_ε is the measurement error covariance matrix,

$$C_\varepsilon = E\left\{\vec{N}_\varepsilon \vec{N}_\varepsilon{}^T\right\}. \tag{3.3.7}$$

We have assumed that the instrument noise levels are uncorrelated between channels and used zeros for the off-diagonal components of C_ε. The covariance for the retrieved state vector is:

$$\hat{C} = C_a - C_a K^T (K C_a K^T + C_\varepsilon)^{-1} K C_a \ . \tag{3.3.8}$$

The *a priori* information, represented by the covariance matrix C_a and the initial guess state $\vec{x}_0$, is an important component of the retrieval algorithm. We have explored two groups of CO profiles as the retrieval *a priori* information. One is compiled from aircraft *in situ* measurements. The other is compiled from the output of a chemical transport model developed. at NCAR. *(Muller and Brasseur, 1995*) For testing purposes, an ensemble of 152 *in situ* measured profiles were used both as the true atmosphere, for retrieval simulations, and to compute the *a priori* statistics for the retrieval. These profiles are compiled from the work of Seiler and Fishman (*1981*), STRATOZ III and TROPOZ II experiments by Marenco *et al.* (*1989, 1994*), and the GTE/TRACE-A experiment by Sachse *et al*. (*private communication*).

Figure 3.3.1 shows a comparison of the mean profiles between the *in situ* measurement ensemble and the model output CO profiles. Also shown in Figure 3.3.1 is a U.S. standard CO profile from the AFGL atmospheric model (*Anderson et al., 1986*). The large tail, near the surface, in the *in situ* measured mean profile reflects the fact that the aircraft measurements are over sampled in heavily polluted coastal cities and airports. In our algorithm testing, we have modified the boundary layer CO values to avoid the large variance produced by this over sampling.

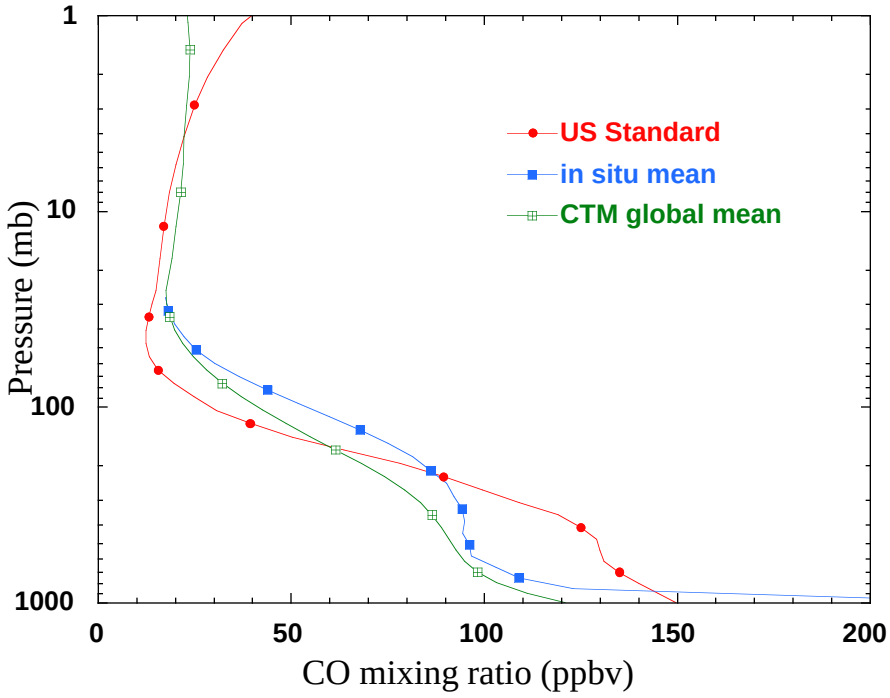

Figure 3.3.1. CO profiles from a U. S. Standard atmosphere model, the in situ measurements, and a 3D model.

It is well known that the distribution of CO varies with latitude and season. (*Novelli et al., 1994; Reichle et al., 1986; Reichle et al., 1989; Reichle et al., 1990*). The typical southern hemisphere mixing ratio is on average around 70 ppbv, while the northern hemisphere values are typically between 100-200 ppbv. The seasonal cycle has its peak value in late winter and early spring and lower values in the summer. Therefore a suitable climatology for an operational retrieval should reflect these variations. We are in the process of enlarging the measurement database as well as combining the measured and model output, to build a CO climatology and to make *a priori* ensembles for several latitude bands.

3.3.2. Analysis and Characterization of the Algorithm

3.3.2.1. Forward Model Sensitivity

The weighting functions represent the sensitivities of the forward signals to the retrieval parameters and are essential to the analysis and characterization of the retrieval. We present the weighting functions in three groups. The first group, plotted in figure 3.3.2, is the sensitivity to surface parameters. The second group, plotted in Figure 3.3.3, is the CO sensitivity of the A signals. The third group, plotted in Figure 3.3.4, is the CO sensitivity of the D and R signals.

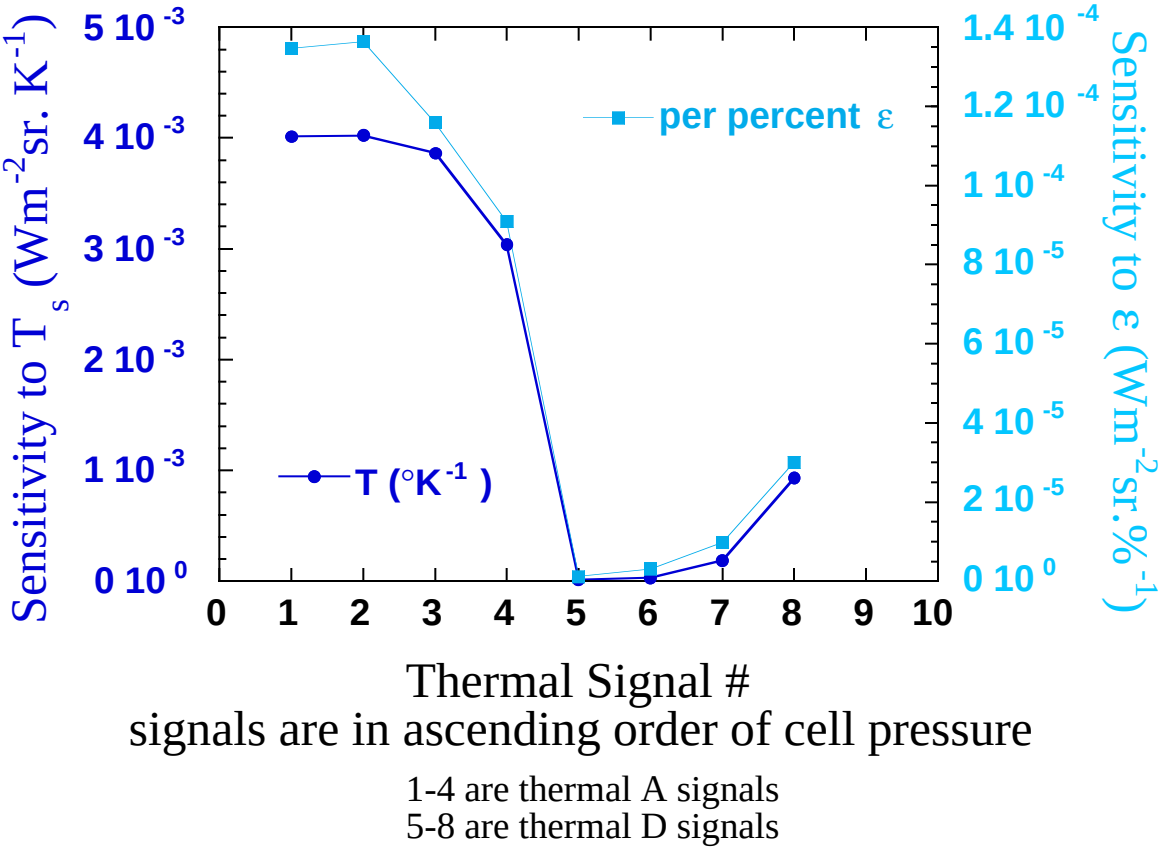

Figure 3.3.2. Sensitivities of MOPITT thermal band signals to the surface temperature and emissivity

As indicated by Figure 3.3.2, the A signals have a larger sensitivity to surface parameters and their sensitivities decrease as the modulation cell pressure increases. The D signals are less sensitive to surface parameters and their sensitivities increase as the modulation cell pressure increases.

Figures 3.3.3 shows that the A signals are also very sensitive to the atmospheric CO, however, the sensitivities all peak in the mid-troposphere (~ 50.0 kPa). The D and R signals have a range of sensitivities which provide the vertical resolutions that the profile retrieval requires.

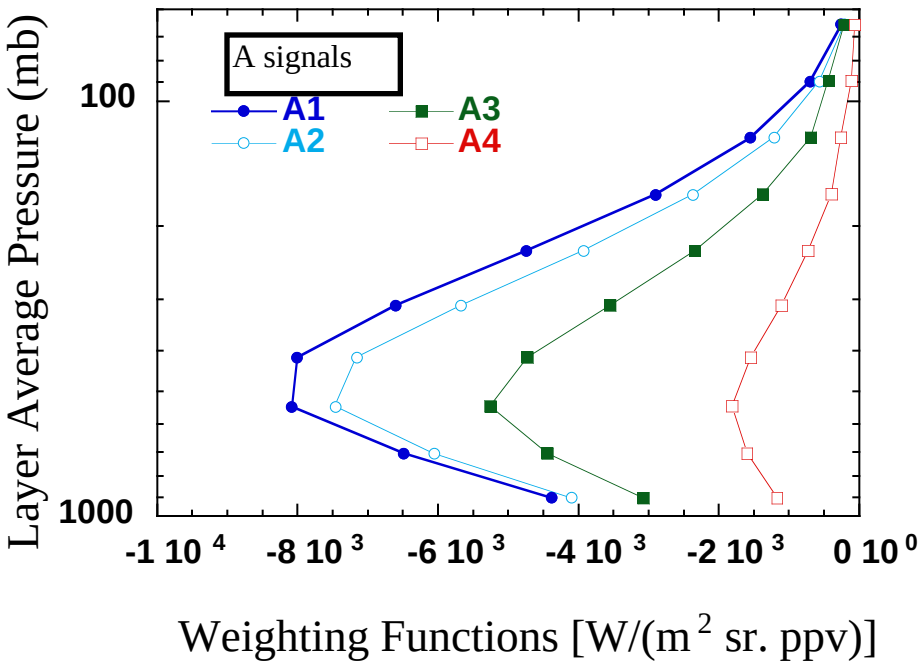

Figure 3.3.3 CO weighting functions for the thermal band A signals

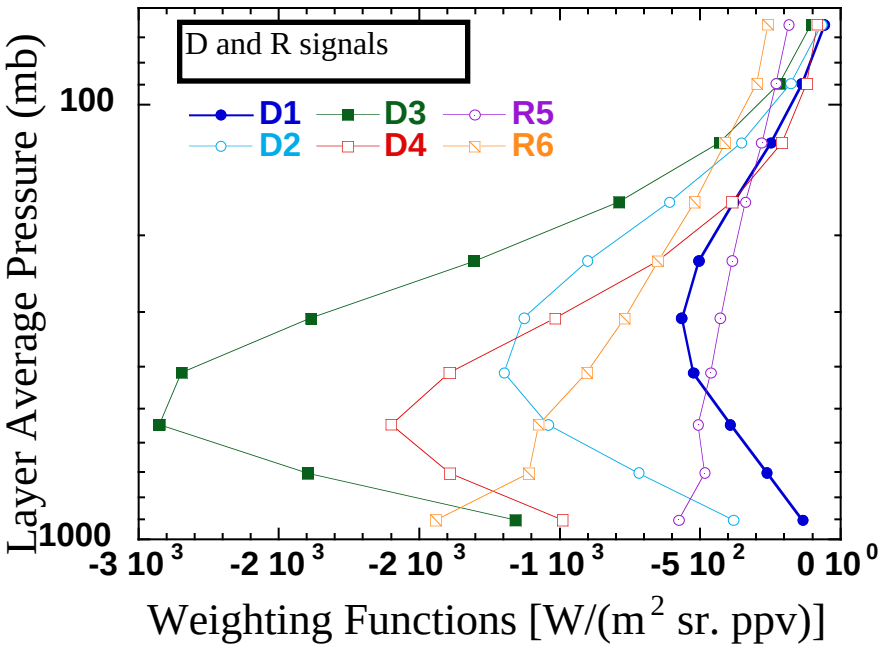

Figure 3.3.4. CO weighting functions for the thermal band D and R signals.

The CO weighting functions as displayed in figures 3.3.3 and 3.3.4, show that the sensitivity of the signals have large overlaps in the vertical range. The orthogonal components of the weighting functions and their corresponding signal-to-noise ratios, for a unit change of CO, are given by the eigenvectors and eigenvalues of an information matrix:

$$H = K^T C_\varepsilon^{-1} K, \tag{3.3.9}$$

where K is the weighting function matrix and C_ε represents the instrument noise as defined in Eq.(3.3.7). We have performed this analysis using the predicted instrument noise from the MOPITT Mission Description Document (MDD) (*Drummond et al., 1993*). The results of this analysis are plotted in Figure 3.3.4.

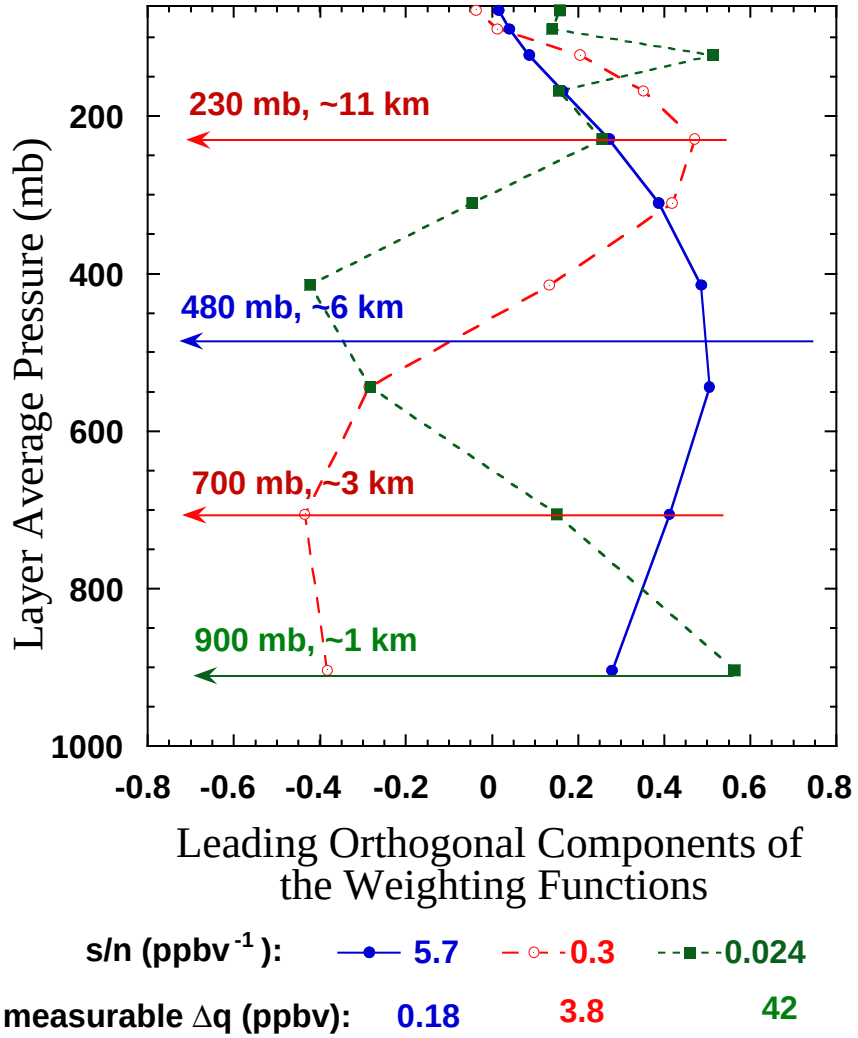

Figure 3.3.5. Three leading components of the weighting functions, their peak positions, their corresponding signal-to-noise ratios, and their corresponding minimum measurable CO changes.

As listed in the legend, the three leading components have the signal-to-noise ratio 5.7, 0.3, and 0.024 per ppbv CO change. The inverse of these numbers, give the smallest measurable change of CO in the direction defined by each corresponding component. The peak positions of the three components are as indicated in Figure 3.3.4. Note that these results strongly depend on the values used for C_ε, *i.e*. the assumed instrument noise, which is subject to change for the actual radiometers.

3.3.2.2. Characterization of the *A Priori* Covariance

A priori information on the atmospheric CO is an important component of the retrieval algorithm. Its representation in the algorithm includes a covariance matrix, which acts as a constraint, and a mean profile, which is used as the initial guess profile. To see the characteristics of the *a priori* constraint, we can decompose the *a priori* covariance into statistically uncorrelated modes using an eigen analysis. This analysis is often referred to as the empirical orthogonal function (EOF) analysis. As an example, Figure 3.3.6 displays the five leading eigenvectors of the covariance matrix, computed from the *in situ* measurement ensemble and scaled by the square root of their corresponding eigenvalues. These eigenvectors are conventionally referred to as the EOFs. Figure 3.3.7 displays the first five EOFs for the

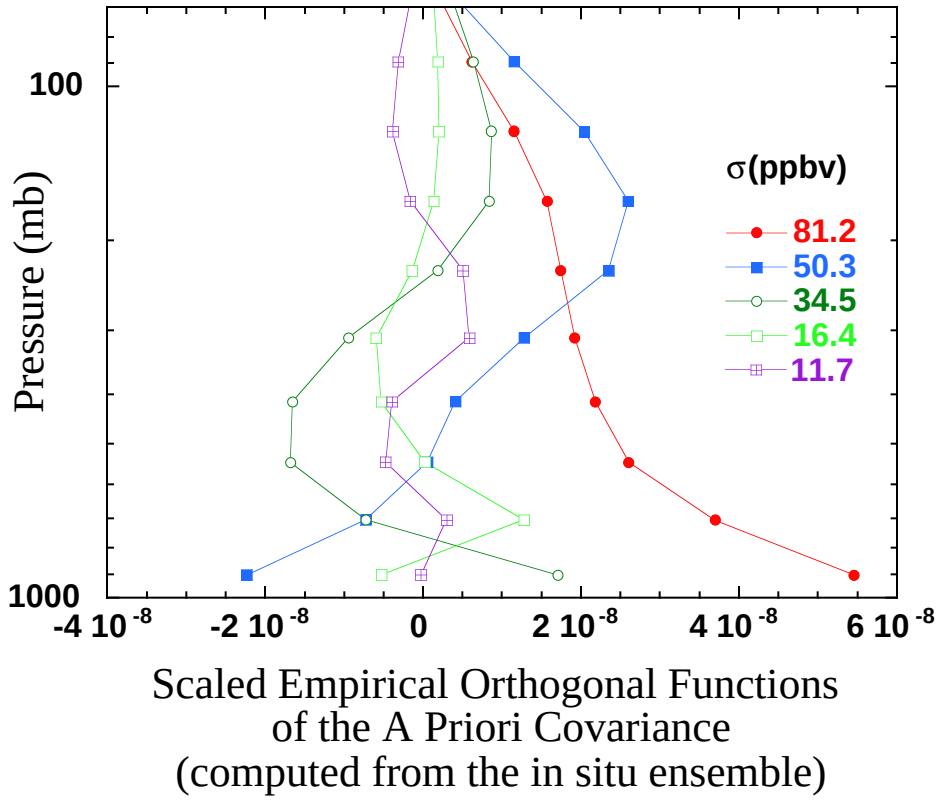

Figure 3.3.6. Five leading eigenvectors for the covariance matrix computed from the *in situ* measurement ensemble, scaled by the square roots of their corresponding eigenvalues as displayed in the legend.

covariance computed from a mixture of measured and model output, with the model profiles being predominate. These vectors give the independent variance patterns. Their corresponding eigenvalues give the uncorrelated variance for each pattern. The effectiveness of the measurement can be evaluated in comparison with the values of the *a priori* variance.

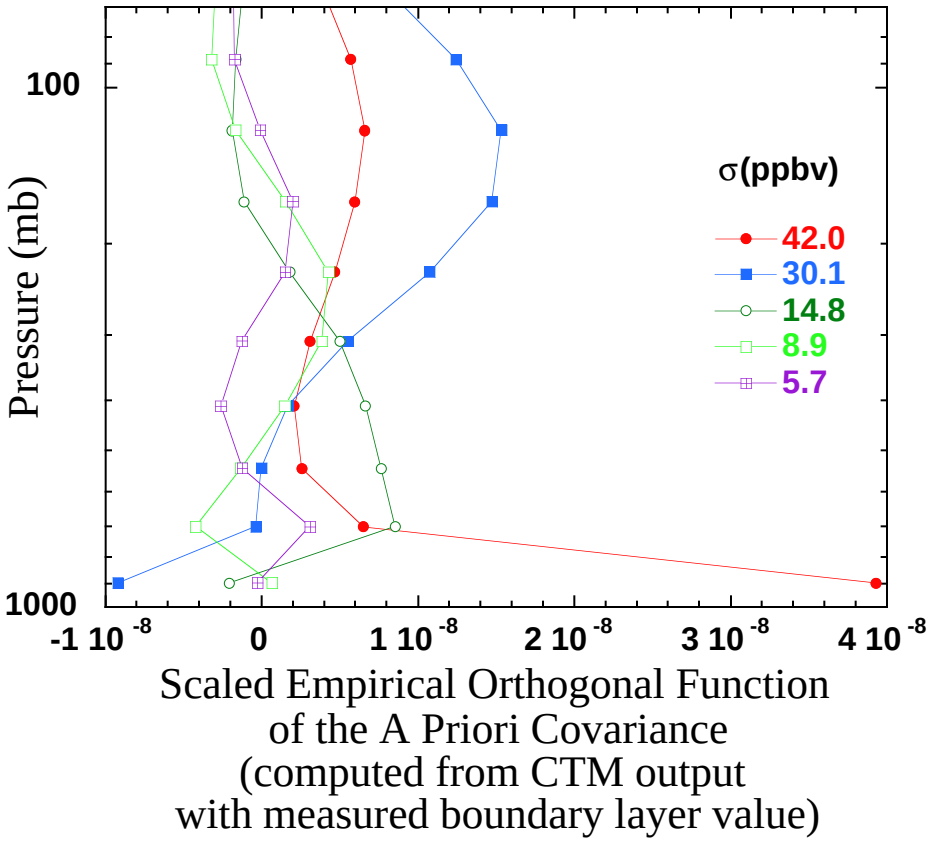

Figure 3.3.7. Five leading eigenvectors for the covariance matrix computed from a predominantly model output ensemble, scaled by the square roots of their corresponding eigenvalues as displayed in the legend.

3.3.2.3. Characterization of the Retrieval

For the purpose of analyzing retrieval characteristics, the retrieved state can be expressed as a transformation of the true state (*Rodgers, 1990*). If we denote the true state as $\bar{x}$, the *a priori* state as $\bar{x}_0$, and neglect the uncertainties of all model parameters, the forward model equation can be written as:

$$\begin{aligned}\bar{y} &= F(\bar{x}) + \bar{N}_\varepsilon \\ &= F(\bar{x}_0) + \frac{\partial F}{\partial x}(\bar{x} - \bar{x}_0) + \bar{N}_\varepsilon \\ &= \bar{y}_0 + K(\bar{x} - \bar{x}_0) + \bar{N}_\varepsilon\end{aligned} \qquad (3.3.10)$$

Similarly, denoting the retrieved state as $\hat{\bar{x}}$, the inverse function as $I(\bar{y})$, we can write the inverse model equation as:

$$\begin{aligned}\hat{\bar{x}} &= I(\bar{y}) \\ &= I(\bar{y}_0) + \frac{\partial I}{\partial y}(\bar{y} - \bar{y}_0) \\ &= I_0 + D(\bar{y} - \bar{y}_0) \quad ,\end{aligned} \tag{3.3.11}$$

where D=∂I/∂y is named the contribution function matrix and represents the sensitivity of the inverse model function to the measurement vector.

Eqs. (3.3.10) and (3.3.11) can be combined to express the retrieved state as a weighted mean of the true state and the *a priori* state, plus the contribution of the noise:

$$\begin{aligned}\hat{\bar{x}} &= T(F(\bar{x}), \bar{\bar{N}}_\varepsilon) \\ &= T(\bar{x}_0) + DK(\bar{x} - \bar{x}_0) + D\bar{\bar{N}}_\varepsilon \\ &\cong \bar{x}_0 + A(\bar{x} - \bar{x}_0) + D\bar{\bar{N}}_\varepsilon \\ &= A\bar{x} + (I - A)\bar{x}_0 + D\bar{\bar{N}}_\varepsilon\end{aligned} \tag{3.3.12}$$

where the rows of the matrix *A=DK* are named the averaging kernels. In Eq.(3.3.12), the step from line 2 to line 3 has assumed that the retrieval model is unbiased. In our case, the explicit form of the averaging kernel matrix can be shown as:

$$A = C_a K^T (K^T C_a K + C_\varepsilon)^{-1} K \tag{3.3.13}$$

Eq.(3.3.12) shows the importance of averaging kernels as characteristic functions of the retrieval. The closer the matrix A is to the unit matrix, the better the retrieved state resembles the true state. The difference *I-A* represents the "smoothing error" which in turn reflects the limits of the resolving power of the measurement.

Figure 3.3.8 shows an example set of averaging kernels for the MOPITT CO profile retrieval, calculated using the weighting functions in Figure 3.3.3, the *a priori* covariance described in Figure 3.3.5 and the noise values estimated in the MOPITT MDD (*Drummond et al., 1993*). The apparent groupings of the averaging kernel peaks around 20.0 kPa and 50.0 kPa reflects the highest sensitivities of the forward model, as shown in Figure 3.3.5.

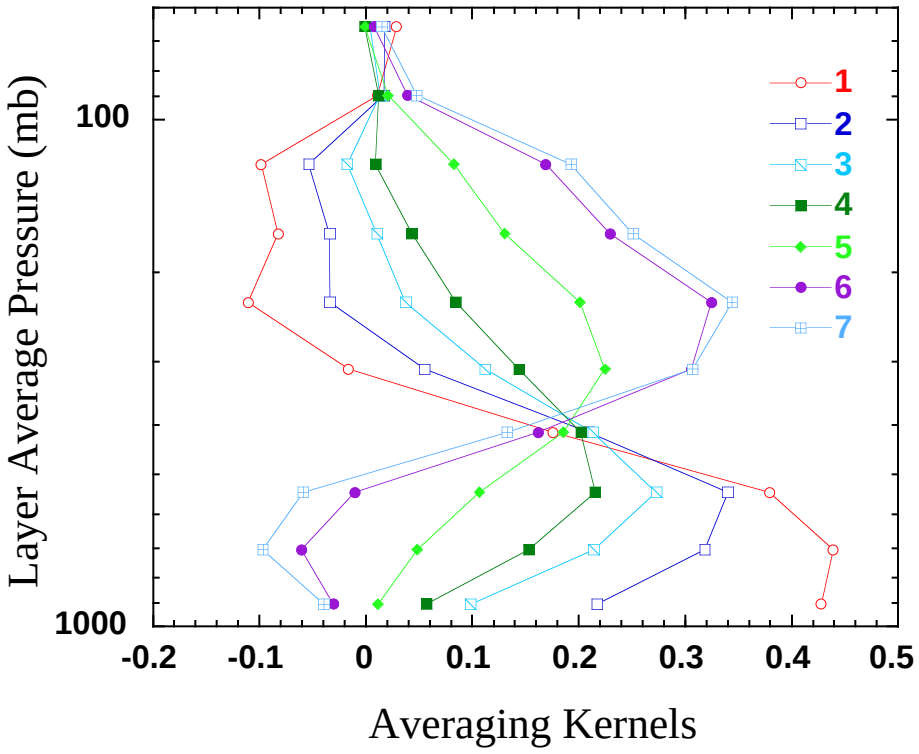

Figure 3.3.8. The first seven averaging kernels for the CO profile retrieval using a two-kilometer atmospheric layering

In order to quantify the smoothing error given by the matrix difference I-A, We have performed an eigenvalue analysis of the A matrix. Since the A matrix is asymmetric, it has a set of left and right eigenvectors. If we use L and R to represent the matrix of left and right eigenvectors, A can be written as:

$$A = L\Lambda R^T, \tag{3.3.14}$$

where Λ is a diagonal matrix with the eigenvalues of A on the diagonal. Using the eigenvectors as a set of basis functions, the last line of Eq.(3.3.12), neglecting the noise, can be transformed into:

$$\hat{\bar{x}}' \cong \Lambda \bar{x}' + (I - \Lambda)\bar{x}_0' \tag{3.3.15}$$

where I is the identity matrix and

$$\hat{\bar{x}}' = R^T \hat{\bar{x}}, \quad \bar{x}' = R^T \bar{x}, \quad and \quad \bar{x}_0' = R^T \bar{x}_0 . \tag{3.3.16}$$

It becomes very clear in Eq.(3.3.15) that the weight of the true profile in the retrieved state depends on the size of the eigenvalues of A. For those components whose corresponding eigenvalues are close to unity, the retrieved profiles show a good resemblance to the true profile.

Figure 3.3.9 shows the three leading right eigenvectors of the *A* matrix, for the CO part of the state vector. Their corresponding eigenvalues are 1.0, 0.98 and 0.21. According to (3.3.15), in the directions defined by the first and second eigenvectors, which correspond to eigenvalues equal to or near unity, the retrieved CO profile values well resemble the true CO profile. In the

direction defined by the third eigenvector, the retrieval gives a large weight to the initial guess profile due to the large departure of the corresponding eigenvalue from unity.

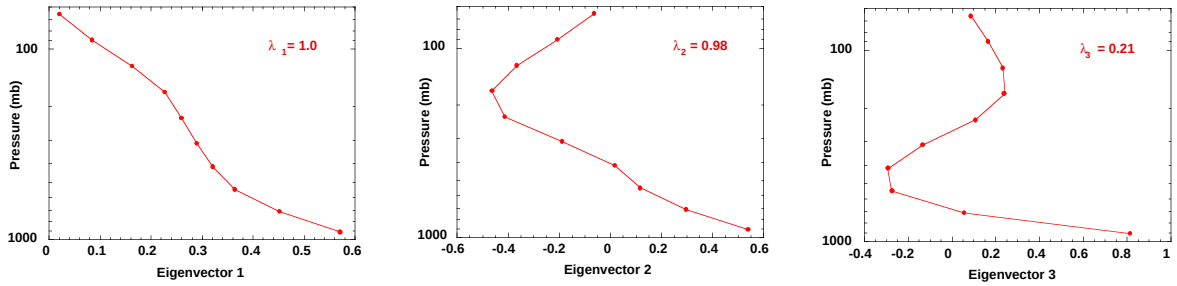

Figure 3.3.9. The three leading eigenvectors of the averaging kernel as plotted in Figure 3.3.8.

3.3.2.4. Effects of the Signal-to-Noise Ratio to the Retrieval Sensitivity and Vertical Resolution

The forward sensitivities and retrieval resolutions characterized by Figures 3.3.5, 3.3.8 and 3.3.9 are result of a given set of signal-to-noise ratios (SNR). An improved SNR will result in an improved sensitivity and resolution, and vice versa.

Two important factors that control the SNR for clear sky conditions are the noise-equivalent-radiance (NER) and the solar band surface reflectivity. For the analysis described in the previous sections, we have used the noise levels as estimated in the MOPITT MDD, which is a conservative estimate, and a value of 10%, for solar channel surface reflectivity, in our analysis and retrieval simulations. To illustrate the effect of SNR on the retrieval, we have performed an analysis of the characteristic functions using a reduced thermal D signal NER (by approximately a factor of 3 from that listed in the MDD) and a solar reflectance term of 30%. The results for the orthogonal components of the weighting function space and the averaging kernels are given in Figures 3.3.10 and 3.3.11, respectively.

Comparing Figure 3.3.10 with Figure 3.3.5, we note that the sensitivities of the first two components are comparable. The third and the fourth components are significantly improved. The smallest measurable CO change for the third component decreased from ~40 ppbv to ~20 ppbv. Additional contributions to the vertical resolution from the fourth component are as marked in Figure 3.3.10.

Comparing Figure 3.3.11 with Figure 3.3.8, it is apparent that with an improved SNR the averaging kernel peaks are more evenly spaced and better correspond to the layer positions of retrieval. This is consistent with the results in Figure 3.3.10 which indicates that with an increased SNR, the instrument sensitivity spans a larger range in the profile space and results in a smaller smoothing error.

Eigen analysis of this averaging kernel matrix yields a new set of eigenvalues. There are now four significant eigenvalues, as opposed to three, in the case represented by Figures 3.3.8 and 3.3.9. Their values are 1.0, 0.99, 0.58 and 0.16. This shows the increase of measurement information content on account of the improved SNR.

Results in this sub-section clearly point out the importance of a good SNR to retrieval sensitivity. Currently, the MOPITT instrument is in the fabrication stage. The noise levels for the actual radiometers will not be available until prelaunch calibration activities are completed.

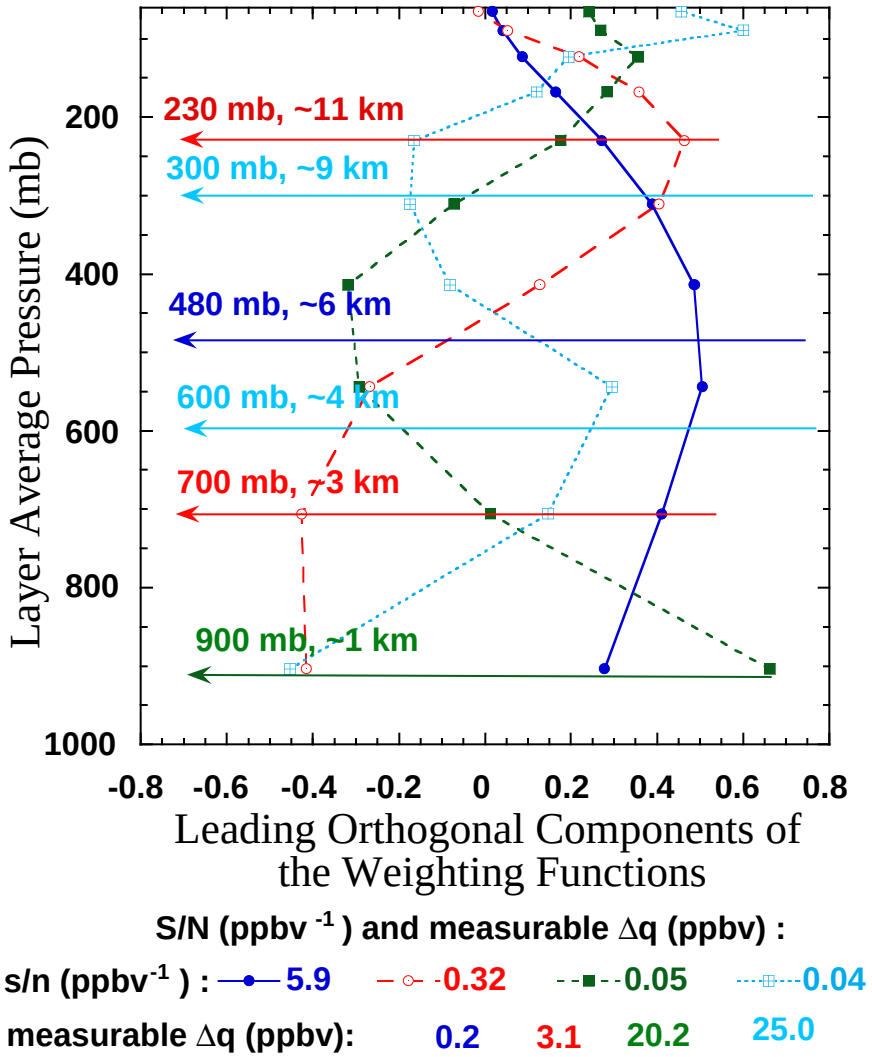

Figure 3.3.10. The four leading components of the weighting functions, their peak positions, corresponding signal-to-noise ratios, and corresponding minimum measurable CO changes, using an improved SNR as specified in the text.

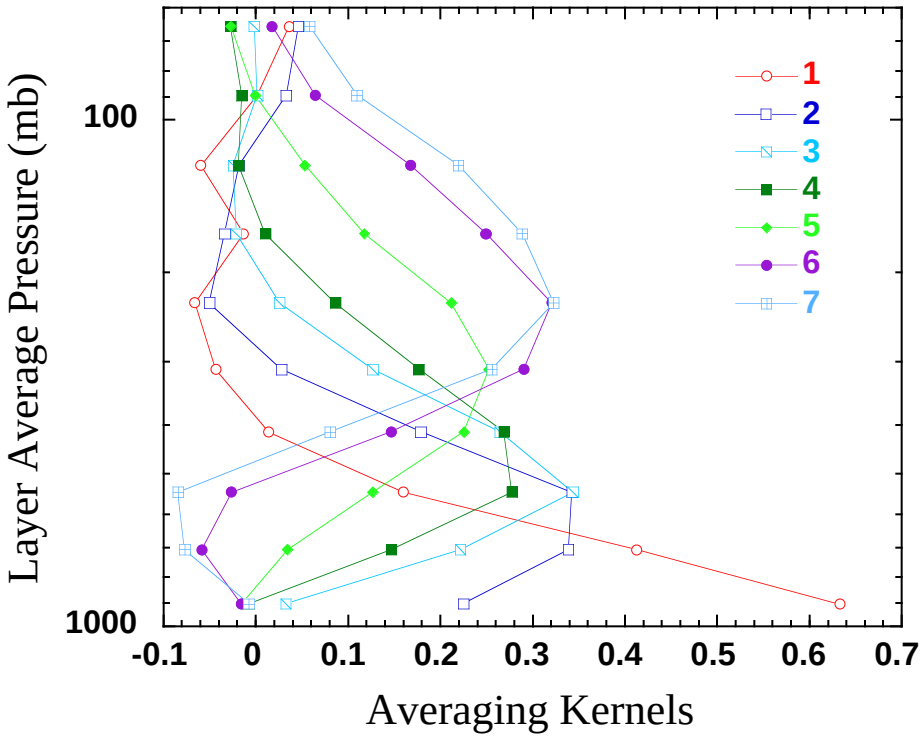

Figure 3.3.11. The CO retrieval averaging kernels computed using the improved SNR as specified in the text.

3.3.2.5. Effect of Varying Lower Surface Height to SNR

The lower surface pressure for each measurement pixel can vary with the change of terrain height or the cloud top height. With this change of surface pressure, the surface temperature will also change. The impact of this change of lower surface pressure and temperature to the MOPITT SNR is simulated using a fixed solar reflectivity (10%). Plotted in Figure 3.3.12 is the sensitivity of the leading component as a function of lower surface pressure.

Figure 3.3.12 shows that the smallest measurable CO change increases rapidly as the lower boundary rises above 40.0 kPa. This is consistent with the information given in Figures 3.3.5 and 3.3.10. The peak position of the leading component is around 5.0 kPa. As the lower surface rises above that range, the technique begins to rapidly loose its sensitivity.

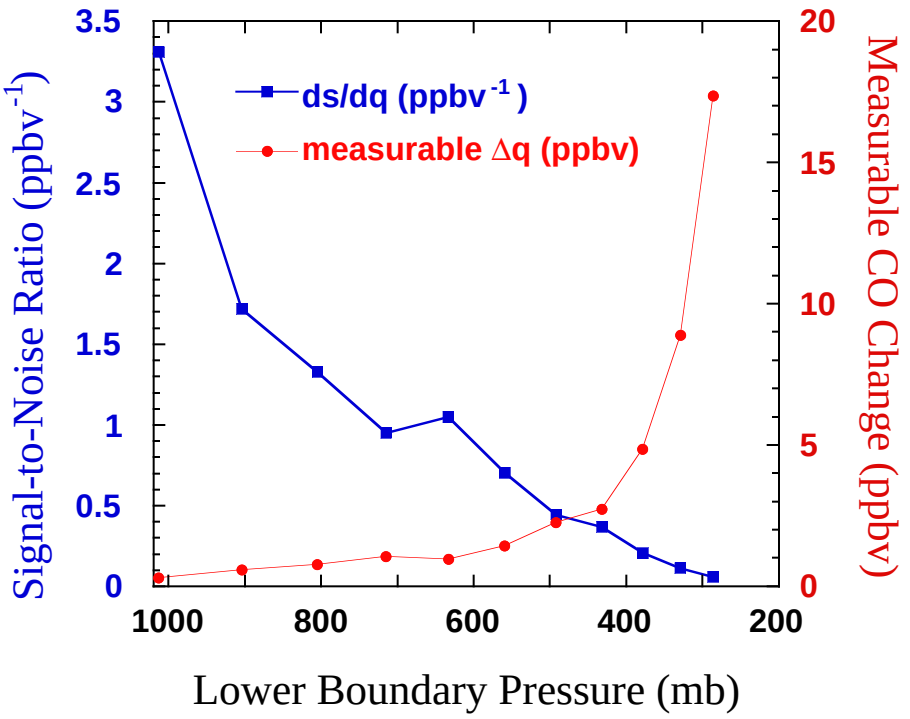

Figure 3.3.12. Sensitivity of the leading component as a function of lower boundary pressure.

3.3.3. Retrieval Variances and Uncertainties

Many factors contribute to the retrieval error. Using the methodology described in Rodgers (*1990*), we can divide the error into four groups according to their sources. Including all model parameters explicitly, we rewrite Eq.(3.3.12) as

$$\begin{aligned}\hat{\bar{x}} &= T(\bar{x}_0, b_0) + DK(\bar{x} - \bar{x}_0) + DK_b(b - b_0) + D\Delta f(\bar{x}, b, b') + D\bar{N}_\varepsilon \\ &\cong \bar{x}_0 + A(\bar{x} - \bar{x}_0) + A_b(b - b_0) + D\Delta f(\bar{x}, b, b') + D\bar{N}_\varepsilon\end{aligned} \tag{3.3.17}$$

where b represents all forward model parameters, $K_b = \partial F/\partial b$ represents the forward model sensitivity to model parameters, Δf is the forward model error which represents the difference between the true forward function and the forward model, and b' represents the missing model parameters that are responsible for the forward model error. Again, we have assumed that the retrieval algorithm is unbiased, since the bias should be identified and removed. Subtract the true state from both side of equation and rearranging terms, we have

$$\begin{aligned}\hat{\bar{x}} - \bar{x} &= (A - I)(\bar{x} - \bar{x}_0) && \leftarrow \text{smoothing error} \\ &+ A_b(b - b_0) && \leftarrow \text{model parameter error} \\ &+ D\Delta f && \leftarrow \text{forward model error} \\ &+ D\bar{N}_\varepsilon && \leftarrow \text{measurement error due to instrument noise}\end{aligned} \tag{3.3.18}$$

The smoothing error and measurement error are intrinsic to the finite instrument sensitivity and resolution. The forward parameter error includes both instrument model error and ancillary data

error. Instrument error includes: the calibration error, the modulation cell pressure and temperature error, and the spectroscopic data error. The ancillary data error includes: the uncertainty in the temperature profile and interfering species profiles, uncertainty in the lower boundary pressure, etc. We have estimated these error using both linear algebraic analysis and ensemble retrieval experiments.

The objective of the error analysis is to determine the expected errors in the retrieved CO profiles and column amounts of CO and CH_4 from MOPITT data. These errors can be both systematic and random. Systematic errors are, at least to first order, independent of time; they usually represent constant bias in the zero or scaling of the results. Random errors are time-varying; they must be described by some statistical parameter such as the expected standard deviation in the error. An ubiquitous source of random error is instrument noise. Rodgers (*1990*) has developed general techniques to characterize errors in atmospheric profiles retrieved from remote sounding measurements. We intend to apply Rodgers' techniques to the MOPITT error analysis. The pre-launch error analysis is based on the estimate of instrument noise. After launch, the error analysis will be updated to include the in-orbit instrument performance data.

3.3.3.1 Systematic Errors

Primary sources of systematic errors include:

(1). *Forward model errors.* Errors due to the forward model include spectral line parameters, line shape, line mixing, continuum, and forward model approximations. The CO error covariance matrix, due to forward model is given by,

$$S_b = D C_b D^T \tag{3.3.19}$$

where D is the instrument contribution function matrix, and C_b is the forward model error sensitivity matrix.

(2). *Errors due to calibration uncertainties.* Calibration errors (gain and offset errors) will also contribute to the systematic error. During pre-flight instrument calibration, uncertainties in calibration can be estimated by looking at stable blackbody sources. During flight, calibration uncertainties can be estimated, to a certain degree, by examining the time series of the calibrated space view radiances which are expected to be randomly distributed with a mean value of zero.

From the MOPITT calibration peer review document (*Calibration Peer Review, March 2, 1994*) the total calibration uncertainty for the longwave channels is +/- 0.2 K, and the total calibration uncertainty for shortwave channels is +/- 0.5 K. The calibration error covariance matrix is generated by setting the diagonal elements to, the square of the channel radiance error due to calibration. The off-diagonal elements are set to zero. The CO error covariance matrix due to instrument calibration uncertainties can be calculated as,

$$S_{M,cal} = D C_{\varepsilon,cal} D^T \tag{3.3.20}$$

where $C_{\varepsilon, cal}$ is the calibration error covariance matrix, and D is the instrument contribution function matrix.

(3). *Errors due to instrument model.* Instrument model errors include spatial response error (FOV), detector misalignment, spectral response error caused by cell pressure and temperature error, spectral response error caused by band-blocking filter error (center wavelength uncertainties, filter spectral response error, filter degradation and shift...). These errors could

become a major part of the overall systematic error. For example, in the case of ISAMS, temperature retrieval systematic errors are dominated by the uncertainties in the spectral positions of ISAMS filters (*Dudhia and Livesey, 1995*). Similarly, the instrument model error covariance matrix can be formed by setting the diagonal elements to the square of the channel radiance error due to the instrument model, and the off-diagonal elements to zero. The CO error covariance matrix due to the instrument model errors can be calculated as,

$$S_{M,inst} = D C_{\varepsilon,inst} D^T \tag{3.3.21}$$

where $C_{\varepsilon, inst}$ is the instrument model error covariance matrix, and D is the instrument contribution function matrix.

(4). *Errors due to atmospheric temperature profile errors.* This error source could considered part of the forward model error, but in order to examine the impact of atmospheric temperature error on the accuracy of CO and CH_4 retrieval, we will consider this error source separately. Define a temperature retrieval sensitivity matrix D_T as,

$$D_T = \frac{\partial \hat{x}}{\partial T} \tag{3.3.22}$$

where $\hat{X}$ is the retrieved CO profile. Therefore the error covariance matrix due to atmospheric temperature error is given by,

$$S_T = D_T \, C_T \, D_T{}^T \tag{3.3.23}$$

where C_T is the temperature error covariance matrix. It is important to include off-diagonal elements because temperature errors at different levels are correlated. Fortunately, atmospheric temperature measurements are widely available from radiosonde reports and satellite retrievals. Thus a realistic temperature error covariance matrix can be generated for the MOPITT retrieval error analysis.

(5). *Errors due to atmospheric water vapor profile errors.* Similarly, this error source can be considered as part of the forward model error, but in order to examine the impact of atmospheric water vapor profile error on the accuracy of CO retrieval, we will consider this error source separately. Define a water vapor retrieval sensitivity matrix D_{H_2O} as,

$$D_{H_2O} = \frac{\partial \hat{x}}{\partial x_{H_2O}} \tag{3.3.24}$$

where $\hat{X}$ is the retrieved CO profile, and X_{H_2O} is the water vapor mixing ratio profile. Therefore the error covariance matrix due to atmospheric water vapor profile error is given by,

$$S_{H_2O} = D_{H_2O} \, C_{H_2O} \, D_{H_2O}{}^T \tag{3.3.25}$$

where C_{H_2O} is the water vapor profile error covariance matrix. It is important to include off-diagonal elements because water vapor profile errors at different levels are correlated. A realistic water vapor covariance matrix can be developed from data available from NMC or ECMWF.

Errors in other atmospheric species, such as N_2O, O_3, CO_2, and surface parameters (emissivity and reflectivity) will also lead to errors in retrieved CO and CH_4. However, their variability are smaller compared with that of H_2O, and climatology values will be used in the forward model calculations.

(6). *Smoothing error or a priori error.* The smoothing error or *a priori* error represents the difference between the retrieved smoothed atmospheric CO profile and the high vertical resolution *a priori* CO profile. Smoothing errors are mainly caused by the finite vertical resolution of the MOPITT measurement. In reality, it is relatively difficult to estimate the smoothing error because it is difficult to get an *a priori* data set that contains all the realistic small scale features of atmospheric CO. If a representative *a priori* covariance matrix can be constructed, the smoothing error can be calculated as,

$$S_{sm} = (A - I)C_a(A - I)^T \tag{3.3.26}$$

where A is the averaging kernel, I is the identity matrix, and C_a is the *a priori* covariance matrix.

3.3.3.2. Random Error

The main source of random error is the instrument noise. Potential random error sources include:

(1). *Errors due to instrument, detector, and electronic noise.* The noise-equivalent-radiance (NER) predicted by the MOPITT radiometric model is used to form the instrument noise covariance matrix $C_{\varepsilon,noise}$. Since the instrument noise, of the different channels, is not correlated, the off-diagonal elements can be set to zero.

$$S_{M,noise} = D C_{\varepsilon,noise} D^T \tag{3.3.27}$$

where D is the contribution function matrix.

(2). *FOV smearing due to pointing jitter.* For a nadir sounder such as MOPITT, with a nadir FOV of 22 km x 22 km, errors due to pointing jitter may be negligible. However, errors due to FOV smearing during instrument stare (~ 400 ms) may be significant and both will be evaluated.

3.3.3.3. Total Error

The total error covariance is given by

$$S = S_b + S_{M,cal} + S_{M,inst} + S_T + S_{H_2O} + S_{sm} + S_{M,noise} \tag{3.3.28}$$

As a preliminary estimate, the square root of the diagonal elements can be considered as the CO and CH_4 retrieval error.

For example, the retrieval errors due to instrument noise and smoothing are calculated using the approaches described above. The CO covariance matrix was generated using 152 aircraft *in*

Layer (km)	Error due to noise (%)	Smoothing error (%)	Total error (%)	RMS retrieval error (%)	Background profile error (%)
0 - 2	10.48	12.45	**16.28**	**16.80**	49.91
2 - 4	1.91	11.03	**11.19**	**10.60**	38.07
4 - 6	5.70	7.87	**9.72**	**10.00**	32.78
6 - 8	6.26	8.54	**10.59**	**11.40**	30.39
8 - 10	2.74	8.75	**9.17**	**10.00**	28.67
10 - 12	4.47	7.49	**8.72**	**8.50**	34.18
12 - 14	8.72	9.93	**13.22**	**16.90**	40.29

Table 3.3.1 Comparison of linear error analysis and retrieval simulation results

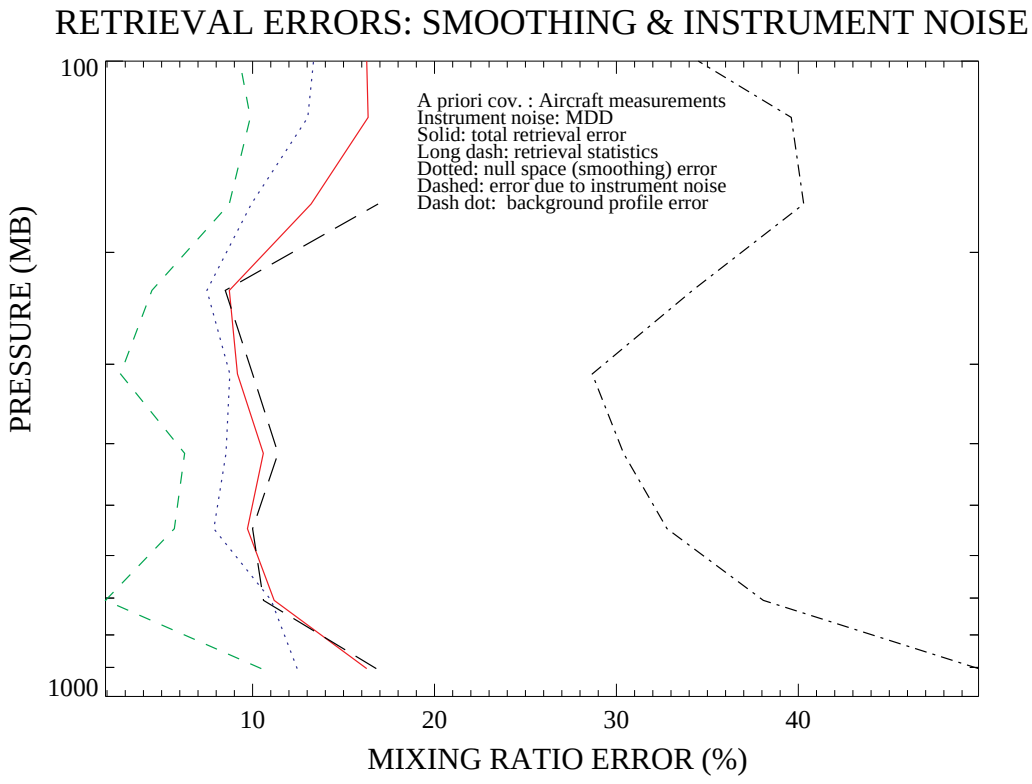

Figure 3.3.13 Retrieval errors due to instrument noise and smoothing. Short dash line (green) is the error due to instrument noise, dot line (purple) is the smoothing error, solid line is the total error due to smoothing and instrument noise, and the long dash line is the RMS error of retrieval simulations using the prototype retrieval algorithm. The dash-dot line on the far right is the mean *a priori* profile error.

situ measurement profiles compiled from Seiler and Fishman (*W. Seiler and J. Fishman, 1981*), STRATOZ III experiment (*Marenco and Prieur, 1989*), TROPOZ II *experiment (Marenco, 1994*), and the GTE/TRACE-A experiment *(Sachse and Logan, private communication, 1994*). Because most of those measurements were conducted in polluted coastal area with high CO concentration in the lower troposphere, the covariance generated is more representative of polluted region rather than the global CO distribution. The instrument noise covariance is generated using the NER of each channel described in the MOPITT Mission Description Document, the diagonal elements are the squares of the channel NER, and off-diagonal elements are set to zero because the noise of each channel are not correlated. The smoothing error, error due to instrument noise, and the RMS of the two are plotted in Figure 3.3.13. The linear error analysis result is also compared with retrieval simulation statistics using the prototype retrieval algorithm. The retrieval simulation used 152 CO profiles. The RMS error is also plotted in Figure 3.3.13. It can be seen that there is excellent agreement between the total error from linear error analysis and retrieval simulation statistics. The smoothing error dominates the total error, which is mainly due to the relatively low vertical resolution associated with nadir sounding technique used in MOPITT. The relatively large errors in the lower troposphere below about 80.0 kPa and in the upper troposphere above 20.0 kPa are mainly due to the bias in the covariance matrix as discussed before, which is also evident from the background profile error plot in Figure 3.3.13. It is expected that a better CO covariance matrix will be generated when additional CO profiles are obtained over more diverse geographical regions. Analysis of errors due to other sources including forward model error, calibration, instrument model, temperature profile error, and H_2O profile error are in progress.

3.3.4. Evaluation and Testing

Numerous ensemble retrieval experiments have been conducted, both to evaluate and test the algorithm and to study the sensitivity of the retrieval to various parameters. Some sample results are given below. These experiments were conducted using the *in situ* measurement ensemble as the true atmosphere. The ensemble mean and variance were used as the retrieval *a priori* constraints. The noise levels were taken from the MOPITT MDD (*Drummond et al., 1993*) and the retrieval used a two-kilometer layering. The retrieved profiles are reported as layer average mixing ratios.

The first four sets of retrieval experiments were designed to isolate and estimate the effect of instrument smoothing, instrument noise and the uncertainties in the ancillary data (*i.e.,* the water vapor profile and the temperature profile information). The results of CO column retrieval are given in Figure 3.3.14. The profile retrieval results are shown in Figure 3.3.15.

In Figure 3.3.14, the length of each horizontal bar indicates the ensemble RMS of the CO column amount retrieval error. The experimental results show an approximately 1% increase of error due to the instrument noise, an approximately $1\frac{1}{2}$% increase of error due to a 10% water vapor profile random error, and an approximately $2\frac{1}{2}$% increase of error for a 2 K temperature random error.

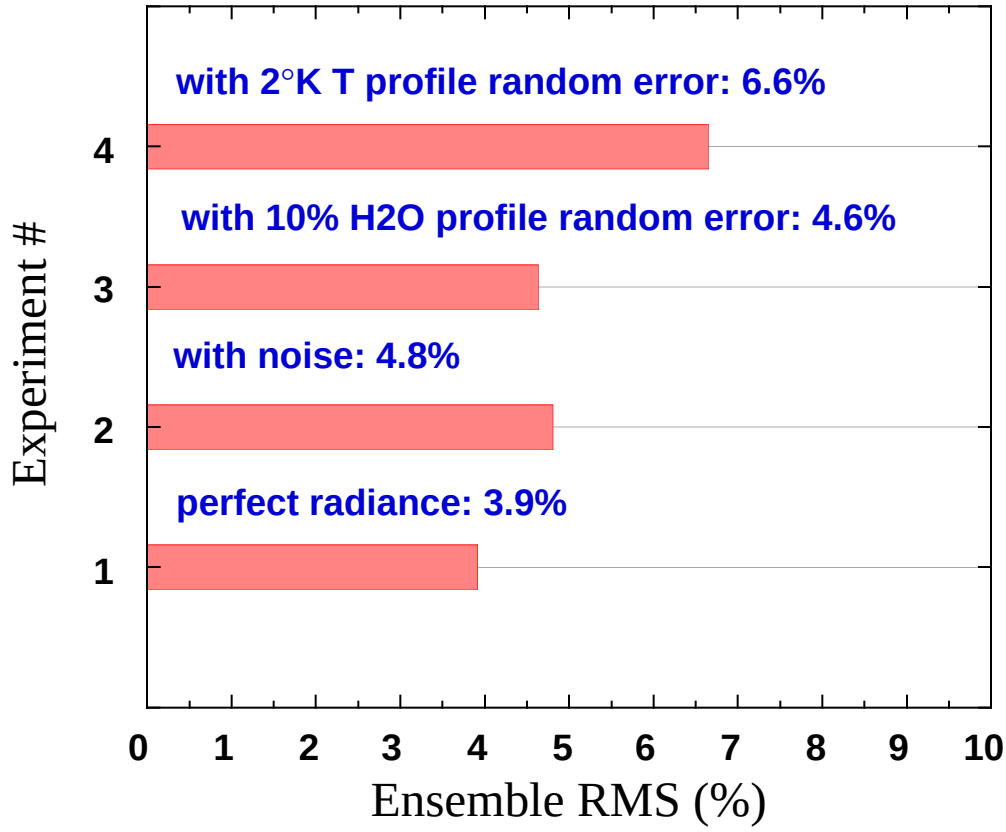

Figure 3.3.14. The ensemble RMS error for the four CO column amount retrieval experiments.

Figure 3.3.15 shows the ensemble RMS error for first seven layers in the CO profile retrieval. The average of the seven layers is given in the legend. Experiment #1 is retrieved from simulated "perfect radiance". In this case, the error is entirely due to the instrument smoothing. Experiment #2 is retrieved from simulated noisy radiance. Comparison of the two experiments shows that retrieval error, for the case of 2-km layering, increased 2% for the given noise level. Experiments #3 and #4 show the retrieval error due to a 10% water vapor profile uncertainty and a 2 K temperature profile uncertainty.

Again, the retrieval error is smaller for the ranges where MOPITT has higher measurement sensitivities, as shown in Figure 3.3.5. Note that these results depend not only on the noise level used in the measurement covariance but also on the layering used for comparison of the retrieved with the true profile.

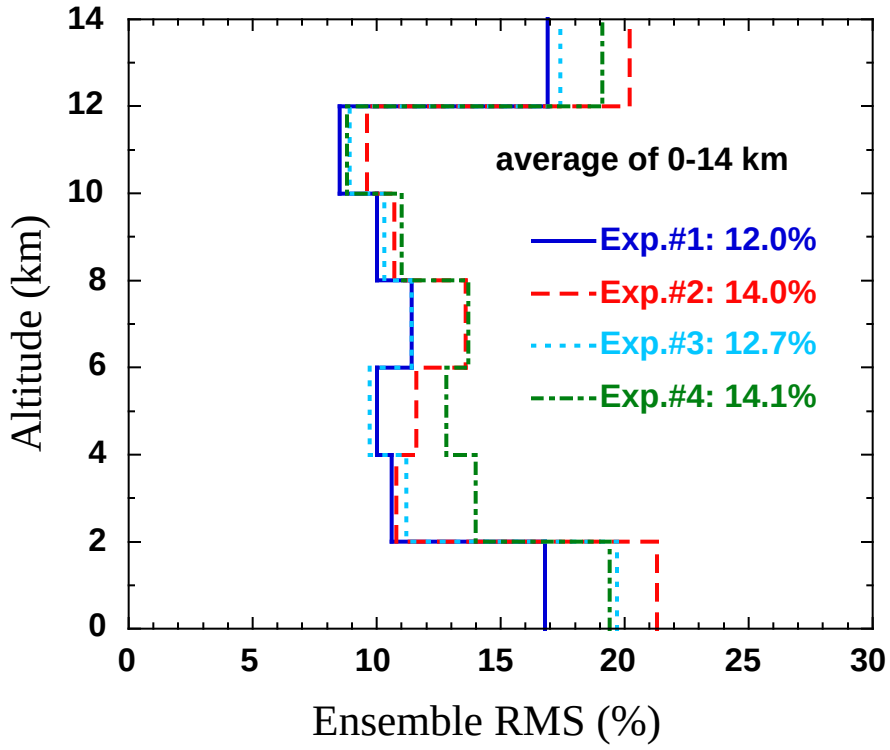

Figure 3.3.15. Ensemble RMS for four CO profile retrieval experiments. In experiment #1, a simulated perfect radiance was used as a measurement signals, *i.e*., there were no errors in the ancillary data. In experiment #2, instrument noise is included in the simulated radiance. In experiment #3, there were 10% random error in the water vapor profiles. In experiment # 4, there were 2 K random error in the temperature profiles.

Besides these four experiments, retrieval experiments have also been conducted to evaluate the retrieval sensitivities to modulation cell pressure and temperature error, to compare the daytime and the nighttime measurements, to estimate the retrieval error due to temperature profile inversions and the impact of errors in estimating the lower boundary pressure, etc.

3.4 CH_4 Column Amount Retrieval Algorithm for the Clear Sky and Cloud Cleared Radiances

3.4.1. Description of the Algorithm

The methane retrieval algorithm follows exactly the CO column amount retrieval described in the section 3.3.1. As specified in section 3.1.4, MOPITT has two identical CH_4 channels in the 2.2 μm solar band. The present version of the prototype retrieval algorithm uses one R signal, as defined in section 3.3.1, for tropospheric CH_4 column amount retrievals.

Although there is only on piece of information from the measurement, it can be shown that it is advantageous to perform a profile retrieval as described in Eqs.(3.3.1)-(3.3.5). The retrieved column amount is obtained from an integration of the profile. In this case, the measurement vector has only one element and there is no need to have surface parameters in the state vector. Hence we have:

$$\vec{y} = (S_1) = \left(R_{7,8}\right), \quad \vec{x} = (x_j) = \begin{pmatrix} q_1 \\ q_2 \\ \vdots \\ q_m \end{pmatrix}. \tag{3.4.1}$$

The dimension of the weighting function matrix in this case is *1×m*,

$$K = \left(k_{1j}\right) = \left(\frac{\partial S_1}{\partial x_j}\right). \tag{3.4.2}$$

A priori statistics for CH_4 have been compiled using both the *in situ* measurement ensemble and the model profile ensemble as described in the section 3.3. The mean profile for the two ensembles and the CH_4 profile from the AFGL U.S. Standard atmospheric model (*Anderson et al., 1986*) are displayed in Figure. 3.4.1. An example of weighting function computed from the *in situ* measurement mean profile is plotted in Figure 3.4.2. Weighted by the corresponding noise, the SNR per ppbv change in the CH_4 mixing ratio is 0.03 which corresponds to a measurable change of 31 ppbv in CH_4 profile.

The five leading EOFs for the *in situ* measurement CH_4 ensemble are given in Figure 3.4.3. As shown in the legend, the leading variance for this ensemble is ~126 ppbv. This fairly large variance is due to the fact that this ensemble collected measurements on a global scale and throughout several seasons. Similar to the CO distribution, the tropospheric CH_4 distribution has a latitudinal and seasonal variation (*Steele et al., 1992*) An enlarged CH_4 database is under development which will allow the compilation of zonal and seasonal *a priori* statistics for retrieval.

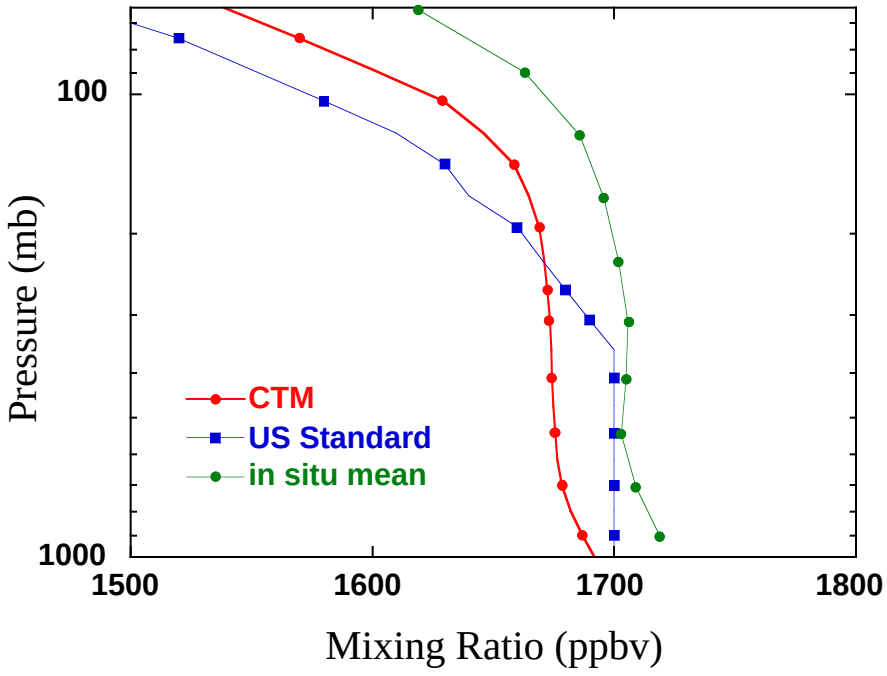

Figure 3.4.1. CH_4 profiles from a U. S. Standard atmosphere model, the in situ measurements, and a 3D chemical transport model.

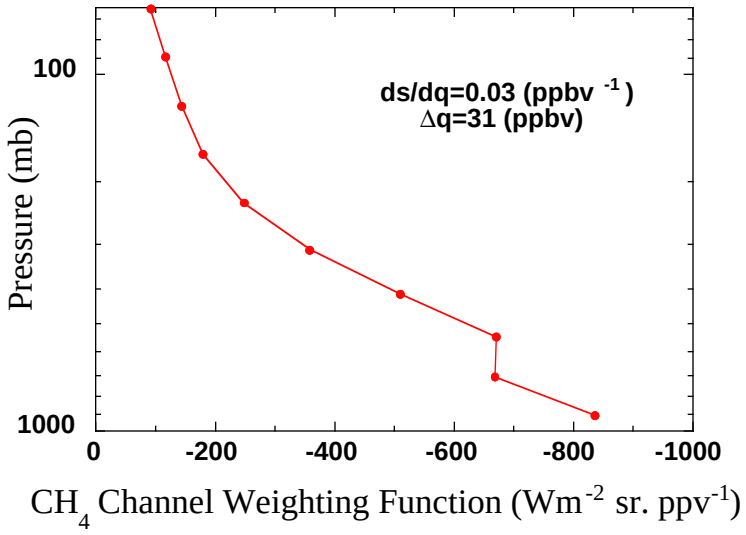

Figure 3.4.2. Weighting function for the R signal of CH_4 channel. The corresponding SNR and measurable CH_4 change are shown in the figure.

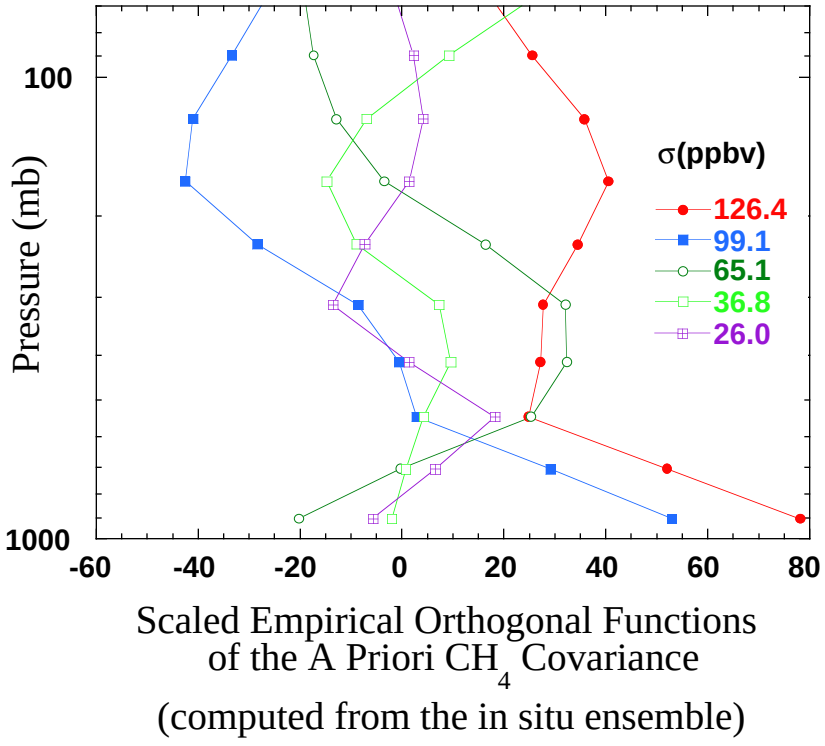

Figure 3.4.3. Five leading eigenvectors for the covariance matrix computed from the CH_4 *in situ* measurement ensemble, scaled by the square roots of their corresponding eigenvalues as displayed in the legend.

3.4.2. Algorithm Evaluation and Testing

The retrieval algorithm has been tested using simulated radiances from the *in situ* measurement ensemble as described in the CO retrieval algorithm section. The NER estimated in the MDD was used as the instrument noise level. The surface reflectivity was assumed to be 10%. The four retrieval experiments were designed to isolate and estimate the retrieval error due to: instrument noise, atmospheric temperature profile and water vapor profile, the results are given in Figure 3.4.4.

As shown in Figure 3.4.4, among all the factors considered, the instrument noise is the leading contributor to the retrieval error. The effect of the temperature profile uncertainty is negligible, as expected from a solar band measurement. The water vapor profile error is reduced by using the R signal.

Another important source for CH_4 retrieval error is the uncertainty in the absorption line parameters. Assessment of retrieval error, due to the uncertainty of this spectroscopic information is in progress.

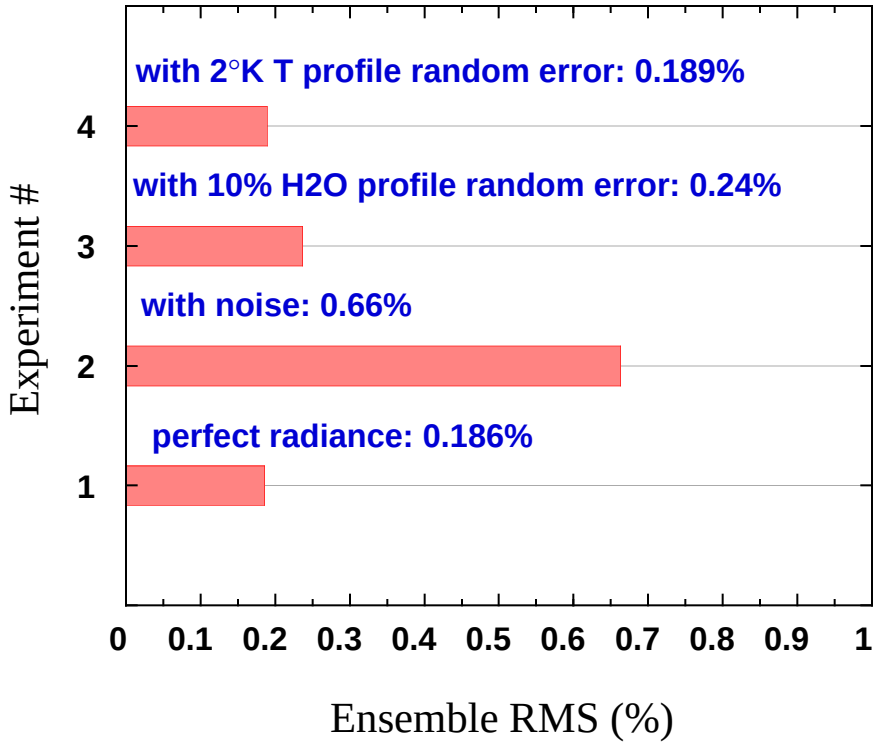

Figure 3.4.4. CH_4 column amount retrieval errors from four retrieval experiments. The length of each horizontal bar indicates the percent RMS error for the 152 profile ensemble experiment.

4.0 Practical Considerations for MOPITT Level 1 to Level 2 Data Reduction

The MOPITT Level 1-2 operational software will generate a retrieved CO profile and CO and CH_4 column amounts from the calibrated radiances for each pixel. The software will conform to the EOSDIS standards (*SDP Toolkit, 1996*). It will invoke the SDP toolkit calls for pixel location and TAI93 time format, it will also use the mathematical libraries (IMSL) that are supported by EOSDIS. The entire production software will be implemented and run at the Langley Research Center DAAC. A description of the MOP01 and MOP02 data products is given in Appendix A.

4.1 Required Input Data

The Level 1 ingested, calibrated and geolocated radiances (*MOPITT ATBD: Level 0-1, 1996*), will be combined with several auxiliary data sets to generate an initial guess for the cloud and retrieval algorithms. The auxiliary data sets will include surface properties: surface type and elevation from the SDP Digital Elevation Model (DEM); surface reflectivities from the MOPITT surface reflectivity data set (*Zhen and Drummond, 1996*); surface pressure and temperature will come from the NASA Data Assimilation Office (DAO) at Goddard Space Flight Center. The auxiliary data set of atmospheric profiles will include: climatological profiles of CO and CH_4; all other profiles (temperature, water vapor etc.) will be supplied from DAO assimilated data sets. Interpolation, in time and space, of the auxiliary data sets will be required to generate the initial conditions for the MOPITT pixel.

4.2 Data Processing Requirements

A M2_config file will be used to store the values of all limits and convergence criteria used in the Level 2 processing. Values contained in the M2_config file may be updated after launch and validation activities are initiated. Information regarding the version of the M2_config file used to process the data, will be recorded in the Level 2 product.

As described in section 3.2, the Level 1 radiances along with the auxiliary data will be used to identify clouds in the MOPITT field of view. Only clear and cloud cleared radiances will be passed on to the retrieval algorithm. Radiances that are rejected by the cloud algorithm will be recorded in a separate file and will be examined off line.

4.3 Quality Control and Exception Handling

Level 1 ingested files are assumed to be calibrated and geolocated and have passed all the quality checks in the Level 0-1 processing (*MOPITT ATBD, Level 0-1, 1996*). Ancillary data will be interpolated in time and space with error estimates assigned to its individual values. These error estimates will be accounted for by both the cloud and retrieval algorithms in their processing.

The cloud algorithm will assign flags to all radiances, indicating if they are clear or the value of the cloud correction applied to them. If an area fails any of the cloud identification criteria, the radiance is rejected and recorded in a separate file. A check on the RMS of the clear and cloud cleared radiances is used to validate the cloud correction technique (Section 3.2).

The retrieval algorithm will only process the radiances and use the auxiliary data that have passed all prior quality control checks. A convergence criteria will be placed on the retrieval algorithm. Any profiles failing to converge within a set number of iterations will be flagged and removed from the Level 2 product. All discarded radiances and retrievals will be analyzed off line by the MOPITT algorithm development team.

4.4 Validation

Validation of the MOPITT Level 1 to Level 2 algorithms and data products is currently being accomplished using both simulated and experimental data. The MOPITT simulator (MOPSIM) is currently being used to assimilate various atmospheric data sets from UARS(*Kumer et al., 1993*), NCAR-CCM2 (*Hack et al.,* 1993), NCAR-CTM (*Muller, J.-F. and G. P. Brasseur, 1995*) and to generate radiances along the expected MOPITT orbital track. The MOPITT simulator, together with the forward model is being used to understand channel sensitivities, generate cloud contaminated radiances, and validate the level 1-2 algorithms. The simulator will also be used to address any postlaunch validation concerns. An incremental examination of auxiliary data inputs, forward model radiances, cloud clearing and retrieval techniques, will be in place to address validation issues and help to identify systematic errors in the retrieved data set.

Experimental data is also being investigated for use in the validation of the Level 1-2 algorithms. The MOPITT Algorithm Test Radiometer (MATR) was flown on the NASA Wallops T-39 aircraft in June of 1996. MATR has the same design principle as the MOPITT instrument, however, it has fewer channels. Initial data processing is underway and data from the aircraft flights will be used to validate the MOPITT algorithms. Further MATR flights are planned for September and October of 1996.

As described in section 3.3 experimental data from Seller and Fishman (*W. Seiler and J. Fishman, 1981*), STRATOZ III experiment (*Marenco and Prieur, 1989*), TROPOZ II experiment *(Marenco, 1994*), and the GTE/TRACE-A experiment *(Sachse and Logan, private communication, 1994*) are being used to develop *a priori* data sets and validate retrieval algorithms

MAPS data (*Reichle et al.,1990*) and potentially Micro MAPS data, will also be an important source of information in development of the Level 1-2 retrieval algorithms and validation of the MOPITT data products. Postlaunch validation of the MOPITT products is detailed in the MOPITT Validation Report (*Wang et al., 1996*).

5.0 References

Ackerman, S., C. Moeller, K. Strabala, R. Frey, B. Baum, R. Welch, P.Menzel, Discriminating Clear Sky from Cloud with MODIS, ATBD-MOD-06, 1994.

Anderson, G. P., S.A. Clough, F. X. Kneizys, J. H. Chetwynd, and E. P. Shettle, *AFGL Atmospheric Constituent Profiles (0-120km)*, AFGL-TR-86-0110, AFGL (OPI), Hanscom AFB, MA 01736, 1986.

Berman, R., P. Duggan, M. P. Le Flohic, A. D. May, and J. R. Drummond, Spectroscopic technique for measuring the temperature and pressure cycle of a pressure modulator radiometer, *Appl. Opt.*, **32**, 6280-6283, 1993.

Connor, B. J., A. Parrish, J. J. Tsou, and M. P. McCormick, Error analysis for the Ground-Based Microwave Ozone Measurements During STOIC, *J. Geophys. Res*., **100**, 9283-9291, 1995.

Drummond, J. R., Measurements of Pollution in the Troposphere (MOPITT), in *The use of EOS for Studies of Atmospheric Physics*, edited by J. C. Gille and G. Visconti, 77-101, North Holland, Amsterdam, 1992.

Drummond, J. R., G.P. Brasseur, G. R. Davis, J.C. Gille, J.C. McConnell, G.D. Pesket, H.G. Reichle, and N. Roulet, MOPITT Mission Description Document, Department of Physics, University of Toronto, Toronto, Ontario, CANADA, M5S 1A7, 1993.

Dudhia, A., and N. J. Livesey, Validation of Temperature Measurements from the Improved Stratospheric and Mesospheric Sounder, Accepted for publication in *J. Geophys. Res*., **101**, 9795-9809, 1996.

Edwards, D. P., GENLN2: A General Line-By-Line Atmospheric Transmittance and Radiance Model, Version 3.0 Description and Users Guide, *NCAR/TN-367-STR*, National Center for Atmospheric Research, Boulder, CO, 1992.

EOS Data Products Reference Guide Volume-1: TRMM & AM-1, S.W. Wharton and M.F. Myers, Editors. NASA Goddard Space Flight Center, In Preparation.

Fleming, H. E., and L. M. McMillin, Atmospheric Transmittance of an Absorbing Gas 2: A Computationally Fast and Accurate Transmittance Model for Slant Paths at Different Zenith Angles, *Appl. Opt.,* **16,** 1366-1370, 1977.

Hack, J.J., B.A. Boville, B. P. Brieglev, J. T. Kiehl, P. J. Rasch, D.L., Williamson, Description of the NCAR Community Climate Model (CCM2), NCAR/TN-382+STR, NCAR, 1993.

Hansen, J. E., L. D. Travis, Light scattering in planetary atmospheres, *Space Sci. Rev*., **16**, 527-610, 1974.

Hansen, J.E., J.B. Pollack, Near-infrared scattering by terrestrial clouds. *J. Atmos. Sci*. **47**,27, 265-281, 1970.

Joiner, J., J. Susskind, C.D. Barnet, Determination of Atmospheric and Surface Parameters from Simulated AIRS/AMSU Sounding Data Part II: Cloud Clearing Methodology, Submitted for publication, 1995.

Khalil, M. A. K., R. A. Rasmussen, Carbon Monoxide in the Earth's Atmosphere: Increasing Trend, *Science*, **224**, 54-56, 1984.

King, M.D., L.F. Radke and P.V. Hobbs, Determination of the spectral absorption of solar radiation by marine stratocumulus clouds from airborne measurements within clouds, *J. Atmos. Sci.* **47**, 894-907, 1990.

King, M.D., Y. J. Kaufman, W. P. Menzel, D. Tanre, Remote sensing of cloud, aerosol, and water vapor properties from the moderate resolution imaging spectrometer (MODIS), *IEEE Trans. Geosci. Rem. Sens*., **30**, 2-27, 1992.

Kumer J.B., Mergenthaler J.L., Roche A.E, CLAES CH_4, N_2O, CCL2F2 (F12) Global Data. *Geophys. Res. Lett.* 20, 1239-1242, 1993.

Ludwig, C. B., M. Griggs, W. Malkmus, and E. R. Bartle, Measurement of Air Pollutants from Satellites, 1, Feasibility Considerations, *Appl. Opt*., **13**, 1494, 1974.

Marenco, A. M., The Airborne Programs STRATOZ and TROPOZ: A Study of Atmospheric Chemistry on Regional and Global Scale, *International Symposium: Space, Aeronautics and Atmospheric Environment* (1994), CIC Meteo-France, March 15-17, 1994.

Marenco, A. M. and S. Prieur, Meridional and Vertical CO and CH_4 Distributions in the Background Troposphere (70°N-60°S; 0-12 Km Altitude) from Scientific Aircraft Measurements During the STRATOZ III Experiment (June 1984); *Atmospheric Environment*, **23,** 185-200, 1989.

May, R. D., D. J. McCleese, D. M. Rider, J. T. Schofield, and C. R. Webster, Tunable Diode Laser Spectral Diagnostic Studies of a Pressure Modulator Radiometer, *Appl. Opt.*, **27**, 3591-3593, 1988.

McMillin, L. M., and H. E. Fleming, Atmospheric Transmittance of an Absorbing Gas: A computationally Fast and Accurate Transmittance Model for Absorbing Gases with Constant Mixing Ratios in Inhomogeneous Atmospheres, *Appl. Opt.*, **15**, 358-363, 1976.

McMillin, L. M., H. E. Fleming, and M. L. Hill, Atmospheric Transmittance of an Absorbing Gas 3: A Computationallyfast and Accurate Transmittance Model for Absorbing Gases with Variable Mixing Ratios, *Appl.Opt.*, **18**, 1600-1606, 1979.

McMillin, L. M., L. J. Crone, M. D. Goldberg, and T. J. Kleespies, Atmospheric Transmittance of an Absorbing Gas. 4. OPTRAN: A Computationally Fast and Accurate Transmittance Model for Absorbing Gases with Fixed and Variable Mixing Ratios at Variable Viewing Angles. *Appl.Opt.*, **34**, 6269-6274, 1995a.

McMillin, L. M., L. J. Crone, and T. J. Kleespies, Atmospheric Transmittance of an Absorbing Gas. 5. Improvements to the OPTRAN Approach, *Appl.Opt., **34***, 8396-8399, 1995b.

Muller, J.-F. and G. P. Brasseur, IMAGES: A Three-Dimensional Chemical Transport Model of the Global Troposphere, *J. Geophys. Res*., **100**,16445-16490, 1995.

MOPITT Algorithm Theoretical Basis Document: Conversion of MOPITT Digital Counts into Calibrated Radiances in Carbon Monoxide and Methane Absorption Bands (Level 0 to Level 1), University of Toronto and NCAR MOPITT Team, August, 1996.

MOPITT Science Data Products Catalog- Beta Delivery. NCAR April,1996.

Nakajima, T. Y., M. D. King, Determination of the optical thickness and effective particle radius of clouds from reflected solar radiation measurements. Part 1: Theory, *J. Atmos. Sci*., **47**, 1878-1893, 1990.

Nakajima, T. Y., M. D. King, J. D. Spinhirne, L.F. Radke, Determination of the optical thickness and effective particle radius of clouds from reflected solar radiation measurements. Part 2: Marine Stratocumulus Observations, *J. Atmos. Sci*., **48**, 728-750, 1991.

Novelli, P. C., L. P. Steele and P. Tans, Mixing Ratios of Carbon Monoxide in the Troposphere, *J. Geophys. Res.,* **97**, 20731-20750, 1992.

Novelli, P.C., K. A. Masarie, P. Tans, and P. M. Lang, Recent Changes in Atmospheric Carbon Monoxide, *Science***, 263,** 1587-1589, 1994.

Pan, L., D. P. Edwards, J. Gille, M. Smith and J. Drummond, Satellite Remote Sensing of Tropospheric CO and CH_4: Forward Model Studies of the MOPITT Instrument; *Appl. Opt.*, **34**, 6976-6988, 1995.

Reichle Jr., H. G., V. S. Connors, J. A. Holland, W. D. Hypes, H. A. Wallio, J. C. Casas, B. B. Gormsen, M. S. Saylor, and W. D. Hesketh, Middle and Upper Tropospheric Carbon Monoxide Mixing Ratios as Measured by a Satellite-Borne Remote Sensor During November 1981, *J. Geophys. Res.,* **91**, 10865-10887, 1986.

Reichle Jr., H. G., H. A. Wallio, and B. B. Gormsen, Feasibility of Determining the Vertical Profile of Carbon Monoxide from a Space Platform, *Appl. Opt.,* **28**, 2104-2110, 1989.

Reichle, Jr., H. G., V. S. Connors, J. A. Holland, R. T. Sherrill, H. A. Wallio, J. C. Casas, E. P. Condon, B B.Gormsen, and W. Seiler, The Distribution of Middle Tropospheric Carbon Monoxide During Early October 1984, *J. Geophys,. Res.*, **95**, 9845-9856, 1990.

Rodgers, C. D., Retrieval of Atmospheric Temperature and Composition from Remote Measurements of Thermal Radiation, *Rev. Geophys. and Space Phys.*, **14**, 609-624, 1976.

Rodgers, C. D., Characterization and Error analysis of Profiles Retrieved from Remote Sounding Measurements, *J. Geophys. Res.,* **95**, 5587-5595, 1990.

Rodgers, C. D., *Inverse Methods for Atmospheric Sounding: Theory and Practice,* July 27, 1995. To be published.TRACE-A data is archived on NASA Langley DAAC. Data used in this work is from a private communication with G. Sachse and J. Logan.

Roscoe, H. K., and R. J. Wells, The variation of pressure, Temperature and transmission within a pressure modulator: measurements with a high-compression modulator, *J. Quant. Spectrosc. Radiat. Transfer*, **41**, 259-285, 1989.

SDP Toolkit Users Guide for the ECS Project, EOSDIS Core System Project Document 333-CD-003-002, Hughes Information Technology Corporation, Landover, Maryland. 1996.

Seiler, W. and J. Fishman, The Distribution of Carbon Monoxide and Ozone in the Free Troposphere, *J. Geophys. Res*., **86**, 7225-7265, 1981.

Steele, L. P., E. J. Dlugokencky, P. M. Lang, P. P. Tans, R.C. Martin and K. A. Masarie, Slowing Down of the Global Accumulation of Atmospheric Methane During the 1980s, *Nature*, **358**, 313-316, 1992.

Susskind, J., J. Rosenfield, and D. Reuter, An Accurate Radiative Transfer Model for Use in the Direct Physical Inversion of HIRS2 and MSU Temperature Sounding Data, *J. Geophys. Res*., **88**, 8550-8568, 1983.

Smith, W.L. Improved Method for Calculating Tropospheric Temperature and Moisture from Satellite Radiometer Measurements, *Mon. Wea. Rev.,* **96** 387-396, 1968.

Taylor, F. W., Pressure Modulator Radiometry, in *Spectroscopic Techniques. Vol.III*, 137-197, Academic Press Inc., 1983.

Wang, J., J. Gille, P. Bailey, L. Pan, L. Rokke, M. Smith, D. Edwards, J. Drummond, G. Davis, H., Reichle, MOPITT Data Validation Plan, NCAR, 1996.

Wylie, D. P., W. P. Menzel, H. M. Woolf, K. I. Strabala, Four Years of Global Cirrus Cloud Statistics Using HIRS, *J. Climate*, **7**, 4-18, 1994.

Zhen, Z.Y, and J.R. Drummond, A Global Surface Reflectivity Data Set for the 2.2-2.35mm Region, *To be submitted for publication*, Department of Physics, University of Toronto, 1996

APPENDIX A

MOP01 & MOP02 Product Description

The following product code descriptions are from the MOPITT Science Data Products Catalog, (*1996*).

EOSDIS Product Code: MOP01

Data Product Overview

The MOPITT Level-1 data product consists of the geolocated, calibrated earth scene radiances, associated instrument engineering data summaries and inflight calibration information. Data granules are one day in duration and limited to the earth scenes observed within the midnight to midnight period. Data from special calibration sequences and instrument diagnostic modes have been excluded.

Data Format

The MOPITT Level-1B product is archived using the HDF-EOS Swath structure which is described along with Application Program Interfaces (APIs) in references listed in Section 2.0. This structure has been defined to represent time ordered, multi-channel instrument data such as MOPITT. HDF-EOS is an extension to the Hierarchical Data Format (HDF) standard developed at the University of Illinois National Center for Supercomputer Applications. Readers should familarize themselves with HDF and HDF-EOS in advance of using the data.

Data Content

```
* NOTE -- DIMENSIONALITIES OF ARRAYS ARE DEFINED IN FORTRAN
ORDER, C ORDER IS REVERSED *

DIMENSIONS
ntrack = unlimited   (number of cross-tracks = Number of swaths)
nstare = 29          (29 stares per cross track swath =  Number
                     in Crosstrack)
npixels = 4     (4 pixels per stare)
nchan = 8       (8 channels of radiance measurement)
nstate = 2           (Average and difference state of correlation
                     cell)
nengpoints = 102     (102 engineering data elements per swath)
neng = 2             (Engineering data elements are represented
                     as an average value over a swath and a
                     standard deviation)
```

ncalib = 8 (Calibration parameters for each radiance element: swath average gain, offset, noise and internal Blackbody radiance and associated standard deviations)

nsunparms = 2 (Number of solar location elements: zenith and azimuth angles)

GEOLOCATION FIELDS

The following are HDF VDATA variable names:

Track Count float: Number of tracks in this data set

Time : double (ntrack) (Holds time of day and date in Tai93 format for first stare in swath. Subsequent stares occur 450 milliseconds apart.See Appendix A for description of Tai93 time format)

Swath Quality : int32 (ntrack) (TBD values to flag if entire swath has valid values)

The following are HDF Scientific Data Set (SDS) variable names

Latitude : float (npixels,nstare,ntrack) (Latitude in degrees -90 to 90)

Longitude : float (npixels,nstare,ntrack) (Longitude in degrees -180 to 180)

Solar Parms : float (nsunparms,npixels,nstare,ntrack) (Solar direction angles at pixel locations in degrees)

(in nsunparms dimension)

1=solar zenith angle

2=solar azimuth

Satellite Parms: float (nsunparms,npixels,nstare,ntrack) (Satellite direction angles at pixel locations in degrees)

(in nsunparms dimension)

1=satellite zenith angle

2=satellite azimuth

DATA FIELDS

The following are HDF Scientific Data Set (SDS) variable names

MOPITT Radiances: float (nstate,nchan,npixels,nstare,ntrack) (MOPITT radiances in *watts meter^{-2} sr^{-1}* - swath format)

(in nstate dimension)

1=average state radiance

2=difference state radiance

Engineering Data: float (neng,nengpoints,ntrack) (Engineering data, one set per swath)

(in neng dimension)

1=Average over time of swath of engineering element

2=Standard deviation of engineering element

(in nengpoints dimension)

1 = cell pressure channel 1 CO LMC 4.7mic in mb (20 mb nominal)

2 = cell pressure channel 2 CO LMC 2.3mic in mb (20 mb nominal)

3 = cell pressure channel 3 CO PMC(Low state 50mb) 4.7mic

4 = cell pressure channel 3 CO PMC(High state 100mb) 4.7mic

5 = cell pressure channel 4 CH4 LMC 2.4mic in mb (80 mb nominal)

6 = cell pressure channel 5 CO LMC 4.7mic in mb (80 mb nominal)

7 = cell pressure channel 6 CO LMC 2.3mic in mb (80 mb nominal)

8 = cell pressure channel 7 CO PMC(Low state 25mb) 4.7mic

9 = cell pressure channel 7 CO PMC(High State 50mb) 4.7mic

10 =cell pressure channel 8 CH4 LMC 2.4mic in mb (80 mb nominal)

11 - 18 = Cell temperature for channels 1 to 8 (1&2 and 5&6 are the same) in K

19 - 22 = Blackbody temperature for 4 optical benches in K

23 - 26 = Chopper temperature for 4 optical benches in K

27 - 30 = Optics temperature for 4 optical benches in K

31 - 102 (Unassigned Engineering data elements in Beta Delivery)

Calibration Data : float (ncalib,nstate,nchan,npixels,ntrack)
(Calibration data for each state, channel and pixel) (AVERAGED OVER SWATH)

(in ncalib dimension)

1=gain

2=offset

3=noise equivalent radiance in *watts meter^{-2} sr^{-1}*

4=Internal Blackbody Radiance in *watts meter^{-2} sr^{-1}*

5=standard deviation of gain

6=standard deviation of offset

7=standard deviation of noise in *watts meter^{-2} sr^{-1}*

8=standard deviation of Internal Blackbody Radiance in *watts meter^{-2} sr^{-1}*

EOSDIS Product Code: MOP02

Data Product Overview

The MOPITT Level-2 data product consists of the geolocated, retrieved carbon monoxide profiles and total column amounts for carbon monoxide and methane. Ancillary data concerning surface properties and cloud conditions at the locations of the retrieved parameters are also included.

MOPITT geophysical parameters are derived from the Level-1B radiances in combination with ancillary data describing the global distribution of surface and atmospheric temperature and humidity. Radiance measurements in the 4.7μm CO band provide the primary information on the vertical carbon monoxide mixing ratio profile in the troposphere. Total column abundances of carbon monoxide and methane are derived primarily using measurements of reflected solar radiation in 2 bands near 2.3 μm and best retrievals thus occur in sunlit portions of the orbits. Clouds have a large influence on the observed radiances and their effects must be modeled appropriately in the retrieval algorithms

Data Format

The MOPITT Level-2 product is archived using the HDF-EOS Swath structure for the Beta Delivery implementation. For subsequent deliveries, the HDF-EOS "Point" structure will be evaluated for use. These structures are described along with Application Program Interfaces (APIs) in references listed in Section 2.0. The Swath structure has been defined to represent time ordered, multi-channel instrument data. Where the MOPITT scenes are interrupted randomly by clouds, much of the regularity of the original cross-track is disturbed resulting in a distribution of data retrieval locations that are more "Point-like" than "Swath-like".

HDF-EOS is an extension to the Hierarchical Data Format (HDF) standard developed at the University of Illinois National Center for Supercomputer Applications. Readers should familarize themselves with HDF and HDF-EOS in advance of using the data.

Data Content

```
* NOTE -- DIMENSIONALITIES OF ARRAYS ARE DEFINED IN FORTRAN
ORDER, C ORDER IS REVERSED *
```

DIMENSIONS

ntime =	unlimited (number of retrieval time/location points)
nprs = 5	(number of pressure levels in retrieved CO vertical profile)
nwavlen = 3	(number of wavelengths for retrieved surface emissivity)

nbound = 4 (number of boundary points to describe pixel area aggregate)

ncoord = 2 (number of coordinates for each point in pixel area aggregate)

ntwo = 2 (Number of reported elements for each retrieved parameter - i.e. for retrieved value and its error estimate)

Data Fields

The following are HDF VDATA variable names:

Time Count : float (number of time/location in the data set)

Time : double (ntime) (time of retrieved profile/column amount observations in Tai93 format. See Appendix A for description of TAI93 time format)

Latitude : float (ntime) (Latitude of retrieved profile/column amount observations in degrees -90 to 90)

Longitude : float (ntime) (Longitude of retrieved profile/column amount observations in degrees -180 to 180)

Solar Zenith Angle : float (ntime) (Solar zenith angle at location of retrieved data point in degrees)

Satellite Zenith Angle : float (ntime) (Satellite zenith angle at location of retrieved data point in degrees)

Surface Indicator : float (ntime) (Land,sea,ice,cloud indicator. TBD values)

DEM Altitude : float (ntime) (Digital elevation model altitude in Km) (not implmented in Beta delivery)

Num Pixels Aggregate : int (ntime) (Number of original 22X22 km pixels in aggregate area for cloud cleared retrieval)

Cloud Description : float (ntime) (Derived cloud fraction)

The following are HDF Scientific Data Set (SDS) variable names

CH4 Total Column : float (ntwo,ntime) (Retrieved CH4 total column in *Molecules/cm*^{2} at retrieval time/location. Column is measured from base pressure to top of atmosphere)

(in ntwo dimension)

1 = Total column value

2 = estimated error bar

CO Total Column : float (ntwo,ntime) (Retrieved CO total column in *Molecules/cm*^{2} at retrieval time/location. Column is measured from base pressure to top of atmosphere)

(in ntwo dimension)

1 = Total column value

2 = estimated error bar

CO Mixing Ratio : (ntwo,nprs,ntime) (Retrieved CO mixing ratio profile at retrieval time/location.)

(in ntwo dimension)

1 = Mixing Ratio value

2 = estimated error bar

(in nprs dimension)

1 = Mixing Ratios at Pressure Level 1 ??

2 = Mixing Ratios at Pressure Level 2 ??

3 = Mixing Ratios at Pressure Level 3 ??

4 = Mixing Ratios at Pressure Level 4 ??

5 = Mixing Ratios at Pressure Level 5 ??

Surface Emissivity : float (ntwo,nwavlen,ntime) (Earth surface Emissivitiy at three MOPITT observation wavelengths from climatology)

(in ntwo dimension)

1 = Emissivity value

2 = Estimated error

(in nwavlen dimension)

1 = 2.2 mic

2 = 2.3 mic

3 = 4.7 mic

Base Pressure : float(ntwo,ntime) (Estimated base pressure of retrieval. Earth surface for clear area retrievals, Cloud top for total overcast area retrievals--in units of mb)

(in ntwo dimension)

1 = pressure value

2 = estimated error bar

Derived Base Temperature : float (ntwo,ntime) (Derived effective base temperature in deg K)

(in ntwo dimension)

1 = Temperature value

2 = estimated error bar

Derived Base Emissivity : float (ntwo,nwavlen,ntime) (Derived effective base surface emissivity)

(in ntwo dimension)

1 = Emissivity value

2 = estimated error bar

(in nwavlen dimension)

1 = 2.2 mic

2 = 2.3 mic

3 = 4.7 mic

Aggregate Bounds : float (nbound,ncoord,ntime) (Bounds of pixel aggregate (TBD) Not implemented in Beta)